University of California
Santa Barbara

Ambient Intelligence Using Wireless Signals

A dissertation submitted in partial satisfaction
of the requirements for the degree

Doctor of Philosophy
in
Electrical and Computer Engineering

by

Saandeep Depatla

Committee in charge:

Professor Yasamin Mostofi, Chair
Professor Upamanyu Madhow
Professor João Hespanha
Professor Heather Zheng

March 2019

The Dissertation of Saandeep Depatla is approved.

Professor Upamanyu Madhow

Professor João Hespanha

Professor Heather Zheng

Professor Yasamin Mostofi, Committee Chair

November 2018

Ambient Intelligence Using Wireless Signals

by

Saandeep Depatla

To My Parents

Curriculum Vitæ
Saandeep Depatla

Education

2018	Ph.D. in Electrical and Computer Engineering (Expected), University of California, Santa Barbara.
2014	M.S. in Electrical and Computer Engineering, University of California, Santa Barbara.
2010	B.Tech in Electronics and Communication Engineering, National Institute of Technology Warangal.

Publications

Journal/Magazine:

- S. Depatla and Y. Mostofi, "Passive Crowd Speed Estimation in Adjacent Regions With Minimal WiFi Sensing," *IEEE Transactions on Mobile Computing* (under review).
- S. Depatla, C. Karanam, and Y. Mostofi, "Robotic Through-Wall Imaging," *IEEE Antenna and Propagation Magazine, Special issue on Electromagnetic Inverse Problems for Sensing and Imaging*,2017.
- S. Depatla, A. Muralidharan and Y. Mostofi, "Occupancy Estimation using only WiFi Power Measurements," *IEEE Journal on Selected Areas in Communications, special issue on Location-Awareness for Radios and Networks*, volume 33, issue 7, 2015.
- S. Depatla, L. Buckland, and Y. Mostofi, "'X-Ray Vision with Only WiFi Power Measurements Using Rytov Wave Models," *IEEE Transactions on Vehicular Technology, , special issue on Indoor Localization, Tracking, and Mapping*, volume 64, issue 4, pp. 1376-1387, April 2015.

Conference:

- S. Depatla and Y. Mostofi, "Passive Crowd Speed Estimation and Head Counting Using WiFi," *IEEE International Conference on Sensing, Communication, and Networking*, (SECON) 2018.
- S. Depatla and Y. Mostofi, "Crowd Counting Through Walls Using WiFi," *IEEE International Conference on Pervasive Computing and Communications*, (PerCom) 2018.
- B. Korany, S. Depatla, and Y. Mostofi, "Subspace-Based Imaging Using Only Power Measurements," *IEEE Sensor Array and Multichannel Signal Processing Workshop*, July 2018.

Abstract

Ambient Intelligence Using Wireless Signals

by

Saandeep Depatla

With a recent increase in the number of wireless devices around us, there is a great interest in using wireless signals to sense and understand our surroundings. Wireless sensing enables several applications and presents us with unique opportunities such as sensing behind walls and preserving the privacy of humans involved. Therefore, there has been a steady growth in the research interests in this area in the recent past. In this dissertation, we focus on utilizing off-the-shelf wireless devices and fundamentally understand the information carried by the wireless signals about the surroundings.

This dissertation is focused on passive wireless sensing using off-the-shelf wireless devices. Since most off-the-shelf wireless device can only make basic measurements such as the power of the signal, the focus of this dissertation is to enable wireless sensing using minimal power measurements from the devices. Furthermore, to preserve the privacy of human subjects in the area, we focus on passive wireless sensing, i.e., without depending on people to carry any device. Moreover, as we may not have a priori access to the area of interest, we develop frameworks for sensing that minimize the requirement of prior calibrations.

This thesis then contributes to the area of wireless sensing through three main topics 1) *Robotic through-wall imaging*, 2) *Occupancy estimation*, and 3) *Joint crowd counting and crowd speed estimation*. First, in *Robotic through-wall imaging*, we utilize unmanned ground robots with standard WiFi connectivity to enable a high-resolution imaging of an area behind walls. We use theories from electromagnetic literature to mathematically

characterize the signal propagation, sparse signal processing for efficient processing, and proper path planning of robots to enable high-resolution imaging of the area. We image several structures using our framework and present the experimental results. Next, in *occupancy estimation*, we first show how to count the number of people walking in an area using only a single standard WiFi link and without relying on people to carry a device. Through a new statistical modeling of received signals, we show that the information on the number of people is captured in the probability density function (PDF) of the received power measurements, which is then used to estimate the total number of people. We then extend our framework to through-wall scenarios where WiFi transceivers are located outside a building and people are walking inside. We show that the received signal can be modeled as a renewal-type process and show that inter-event times capture the information about the total number of people. We then show several experimental results, using our framework, and show that we can estimate up to 20 people with a very good accuracy.

Finally, in *joint crowd counting and crowd speed estimation*, we estimate several occupancy attributes such as the total number of people, their walking speed, and the rate of arrival of people into the area using a pair of standard WiFi links. We further extend our approach to estimate these attributes in the adjacent regions where there may not be any WiFi coverage. We then show several experimental results with various speeds and up to 20 people and estimate the occupancy attributes. We also show experimental results of our framework in Costco, a retail store.

Contents

List of Figures

List of Tables

Chapter 1

Introduction

The number of devices with wireless capability has been increasing at an exponential rate in recent years. This growth is fueled by the advancement of Internet-of-things (IoT) which includes devices ranging from personal devices such as smart watches to smart televisions. It is expected that there will be about 50 billion IoT devices by 2020 [1]. The majority of these devices have wireless capability for the purpose of communication. As we are surrounded by several wireless devices, can we use them to understand the surrounding environment? More specifically, can we use wireless signals to sense the surrounding environment? For instance, can we use them to image an area or count the number of entities? This thesis looks at the fundamental aspects of wireless sensing to understand how much we can infer about the surrounding environment using wireless signals.

Wireless signals capture crucial information about the surrounding area. As the wireless signals propagate, they interact with the objects in the area. For instance, the signals get absorbed or scattered by the objects and in that process leave their signature on the signals. This thesis looks at understanding what information is present in the signals by mathematically characterizing the signal interactions and estimating the parameters of interest by processing the received signal.

Wireless sensing presents us with several unique capabilities. Since wireless signals

can pass through objects, they can be used to sense in areas that are occluded. For instance, they create the possibility to image or count the number of entities in an area that is occluded by walls, which is not possible by other sensing modalities such as vision-based techniques. Moreover, when sensing anything related to human subjects, such as counting the number of people, wireless signals present us with a unique opportunity to sense without invading the privacy of the people. Furthermore, since wireless signals do not require any ambient lighting conditions, sensing can be done in dark. Finally, there are several applications that can be enabled by wireless signals, such as imaging an area, counting the entities, estimating the speed of a crowd, gesture recognition, tracking, and localizing people among several others.

In this thesis, we investigate wireless sensing by utilizing only the minimal possible measurements that can be obtained from off-the-shelf wireless devices and without relying on people to carry any device. More specifically, we utilize only the signal power measurements (e.g. Received Signal Strength Indicator (RSSI)) and minimize the prior calibration in the area of interest.[1] Although we can extract more information and perform more robust sensing by utilizing the signal phase measurements, most off-the-shelf wireless devices cannot measure the phase in a stable manner. For instance, Bluetooth Low Energy (BLE), utilized in many IoT devices, can only measure the RSSI. Furthermore, when sensing involves human subjects, we are interested only in passive sensing, i.e., without requiring people to carry any device. It has been recently shown by several surveys that requiring people to carry a device is not feasible. For instance, a recent survey on active WiFi tracking technology [2] revealed that 80% of the shoppers do not like to be tracked based on their smartphones, while 43% do not want to shop at a store that employs active WiFi tracking technology. Therefore, in this thesis, we focus on

[1] In all our experiments, we utilize only RSSI measurements, which can be easily measured in any device. However, all the proposed approaches can be easily implemented with CSI power measurements.

wireless sensing using off-the-shelf wireless devices, with minimal prior calibration in the area of interest, and without requiring human subjects to carry any devices.

In this thesis, we focus on three different areas of wireless sensing as described below.

- **Robotic through-wall imaging:** Consider the scenario shown in Fig. 1.1. A couple of robots equipped with WiFi transceivers move around an area that is completely unknown to them and collect WiFi RSSI measurements. The objective then is to obtain a high-resolution image of the area including any occluded objects by utilizing the WiFi RSSI measurements.

  The ability to see through occluded objects can be beneficial to many applications, such as search and rescue, surveillance and security, archaeological discovery, detection/classification of occluded objects, and medical applications.

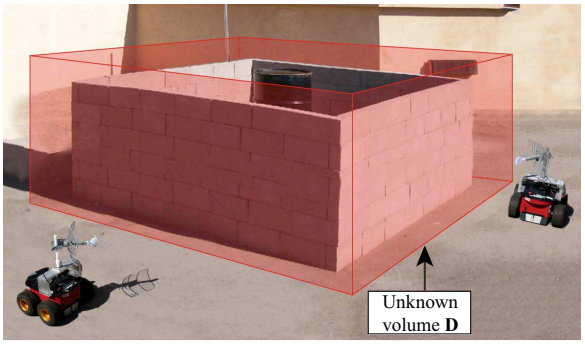

Figure 1.1: Two robots are tasked with imaging the unknown area **D** that is marked with the red superimposed volume, which involves seeing through walls, based on only a small number of WiFi measurements.

- **Occupancy estimation:** Consider the scenario shown in Fig. 1.2 where a number of people are walking in an area. A WiFi link in the area collects the RSSI measurements. The objective then is to estimate the total number of people walking in the area without relying on people to carry any device. Fig. 1.2 (left) considers a scenario where the WiFi Transmitter (Tx) and Receiver (Rx) are located in the same area. Fig. 1.2

Figure 1.2: A stationary WiFi transmitter and receiver are tasked with determining the number of people in the area based on only the received power measurements over a short period of time. (left) Considers a scenario where the Tx and Rx are located in the same area where people are walking, while (right) considers a scenario where the Tx and Rx are located outside a building while people are walking inside.

(right) considers a scenario where the WiFi Tx and Rx are located outside a building while people are walking inside.

The ability to estimate the total number of people in an area can be useful for several applications. For instance, smart buildings can optimize the energy consumption based on the number of people in the building [3, 4]. Retails can better plan their business by assessing which parts of the store get more visitors [5]. Smart cities can better plan the resources by estimating which areas of the city are more crowded [6].

- **Joint crowd counting and crowd speed estimation:** In this part, our objective is to infer various occupancy attributes of an area, such as the total number of people in the area, their walking speeds, and the rate of arrival of people into the area by utilizing a pair of WiFi links. Consider a scenario shown in Fig. 1.3 (left) where people are walking in an area and a pair of WiFi links collect WiFi RSSI measurements. This is a typical museum room scenario where people can traverse the area several times back and forth. The objective, in this case, is to estimate the total number of people along with the average walking speed of the crowd. Fig. 1.3 (right) considers a retail store type scenario where people enter an aisle, spend some amount of time, and exit the

Figure 1.3: A pair of WiFi links are tasked with determining the occupancy attributes in the area based on the received power measurements over a short period of time. (left) Considers a museum room type scenario where the number of people is changing slowly with time and the objective is to estimate the total number of people in the area as well as the average walking speed of the crowd. (right) Considers a retail store type scenario where the objective is to estimate the rate of arrival of people into the area along with the average speed of the crowd.

aisle. Our objective here is to estimate the rate of arrival/departure of people into/out of the area along with the average speed of the people. We are further interested in estimating these occupancy attributes in the surrounding WiFi free regions, i.e., where there is no WiFi coverage.

Sensing the occupancy attributes of an area, such as the corresponding speed of people when traversing the area, their arrival/departure rate into/out of the area, as well as the total number of people in the area can be useful in many applications. For instance, retail stores can learn about the popularity of the products in different aisles, if they know buyers' speed/density in different parts of the store. Consider an aisle in a retail store containing a specific type of product, for instance. Shoppers that are entering this aisle will walk at a normal pace if the products in the aisle do not attract their attention. On the other hand, they may slow down, or stop to look at the items if they find them of interest. Therefore, by estimating the average speed of the shoppers in an aisle, the popularity of the products in that aisle can be inferred. This information, in turn, can significantly help with business planning. Similarly, museums can estimate

which of their exhibits are more popular, based on the speed of the visitors, as well as their arrival rate into different areas.

We next review the literature and summarize our contributions in each of the above-mentioned areas.

1.1 Robotic Through-Wall Imaging

A survey of the related literature indicates that localization and mapping has been investigated by three different communities. More specifically, in the networking community, both device-based and device-free localization based on RF signals have been explored, typically in the context of tracking human motion [7–13]. However, in most of these setups, either the object of interest is not occluded or the information of the first layer of occluder is assumed known. Furthermore, most focus has been on motion tracking and not on high-resolution imaging. Finally, most work on RF sensing in the networking literature do not use off-the-shelf devices or readily available signal measurements, such as received signal power.

In robotics, localization and mapping of objects is crucial to proper navigation. As such, several work, such as Simultaneous Localization and Mapping (SLAM), has been developed for mapping based on laser scanner measurements [14–17]. However, in these approaches, mapping of occluded objects is not possible. For instance, in [18], some information of the occluded objects is first obtained with radar and then utilized as part of robotic SLAM.

In the electromagnetic community, there has been interest in solving an inverse scattering problem [19], i.e., deducing information about objects in an environment based on their impact on a transmitted electromagnetic wave [20–22]. For instance, remote sensing to detect oil reserves beneath the surface of the earth is one example [23]. Traditional

medical imaging based on X-ray also falls into this category [19]. There has also been a number of work on using a very general wave propagation model for inverse scattering, such as Distorted Born Iterative method [20], contrast source inversion method [24], and stochastic methods [25]. However, the computational complexity of these approaches makes it prohibitive for high-resolution imaging of an area of a reasonable size. Furthermore, most such approaches utilize bulky equipments, which makes their applicability limited.

In this thesis, we are interested in high-resolution see-through imaging of a completely unknown area, based on only WiFi RSSI measurements, and its automation with unmanned vehicles. We next describe our contributions in this area

Contributions:

- **Modeling:** We mathematically characterize the interaction of transmitted wireless signals with the objects in the area by tapping into the electromagnetics literature and show that information about the objects is captured in the received power of the wireless signals. More specifically, we utilize WKB and Rytov approximations for this purpose. We further utilize compressive sensing theories to take advantage of image compressibility.

- **Robotic path planning:** We utilize unmanned vehicles and focus on their path planning to optimize imaging through walls.

- **Experimental imaging of several areas:** We experimentally demonstrate imaging of several areas through walls. As compared to [26], this work uses a more extensive wave modeling that results in a better imaging.

1.2 Occupancy Estimation

In the second part of the thesis, we focus on occupancy estimation, i.e., estimating the total number of people walking in a given area, based on only WiFi power measurements between a transmitter and a receiver. Fig. 1.2 shows an example of our considered scenario, where a fixed Tx/Rx pair are tasked with estimating the total number of people that are casually walking in an area.

A survey of the literature indicates that the problem of crowd counting has been investigated by researchers from computer-vision, wireless networking, and environmental science communities. In computer-vision, for instance, photographic images of an area are used to identify the number of people present in the area [27–29]. However, these methods 1) require a network of cameras to be installed in the area of interest and as such have a high deployment cost, 2) cannot work in the dark, 3) cannot work behind walls, and 4) pose privacy issues. Researchers in the environmental science community utilize the characteristics of the area of interest such as temperature, concentration of carbon dioxide, and dew point to identify the number of people in the area [30–33]. However, sensing the environment in this manner requires a direct access to the area of interest and cannot be used in areas occluded by walls or in areas where access is restricted. Furthermore, they require installing specialized sensors.

The ability of radio frequency (RF) signals to penetrate through objects, such as walls, combined with the ubiquity of wireless devices, such as WiFi routers, provide a great potential for imaging [34–36], tracking [37], and occupancy estimation using RF signals. Crowd counting based on wireless devices can be mainly classified into (i) device-based active and (ii) device-free passive methods. The device-based active methods rely on people to carry a communication device [38, 39], which can limit their applicability. For this reason, there has recently been a considerable interest in device-free methods,

which do not require people to carry any device. Instead, device-free methods rely on the interaction of the wireless signals with the people in the area of interest.

In this context of device-free counting, [40] classifies the crowd density in an area into low, medium, and high using a network of wireless nodes. [41] uses the variance of the WiFi received signal strength indicator (RSSI) to estimate up to 7 people. However, this approach uses an extensive prior learning phase with different number of people. Furthermore, the approach requires a large number of wireless nodes (10 Rx and 1 Tx). [42] simultaneously estimates the number and the locations of up to 4 people with 22 wireless nodes. [43] uses differential channel state information (CSI) to classify the number of people. The method has an extensive calibration phase and is only tested with up to 7 people. [44] counts up to 30 people, using CSI measurements at 30 subcarriers and with 4 WiFi links located in the area. The method requires an extensive training phase with 7 experiments and up to 7 people walking in the same area a priori.

In this thesis, through a proper mathematical characterization of the blocking and multipath fading effects, we show how we can count up to and including 20 people in both indoor and outdoor environments with a good accuracy. To the best of our knowledge, a similar characterization and performance have not been reported before with only RSSI measurements. We then extend our approach to count the number of people in a behind-wall scenario i.e., estimating the number of people walking inside a building using a pair of WiFi transceivers located outside the building. We mathematically characterize the statistics of the inter-event times which are less prone to wall attenuation and show that they carry information about the number of people which we then use to infer the occupancy.

Contributions: We separate the impact of a walking person on the transmitted WiFi signal into two key components: 1) blocking of the LOS and 2) multipath effect. This separation is important as each component carries information on the total number

of people in a different way. We then mathematically characterize the first component probabilistically. Our results indicate that this component carries vital information on the total number of people. We further characterize the scattering impact of people through probabilistically analyzing the resulting multipath fading as a function of the number of occupants. By putting the two components together, we finally develop a mathematical expression for the probability distribution function of the received signal amplitude as a function of the total number of occupants, the first such expression to the best of our knowledge. This derived PDF is then compared to the experimental one via using Kullback-Leibler divergence as a metric, and the argument that minimizes it is taken as the estimate of the number of occupants. We then run extensive indoor and outdoor experiments with up to and including 9 people and both omni and directional antennas. Our results confirm that the proposed framework can estimate the total number of walking people with a good accuracy. For instance, an error of 2 or less is achieved 96% and 63% of the time for the outdoor and indoor cases respectively, when using the typical omni-directional antennas that come as part of the standard WiFi cards. When using directional antennas, we further observe an error of 2 or less 100% of the time for both the outdoor and indoor cases.

In the scenario of through-wall crowd counting, we rely only on the LOS blockage event and characterize the inter-event times where an event corresponds to the LOS blockage event. We show that the effect of a single person on the WiFi link can be modeled using a process that we refer to as a "Renewal-type" random process. We then show that the inter-event times carry vital information on the total number of people, and are more robust to the attenuation caused by the walls (as compared to the dip values), enabling a high-accuracy estimation through walls. More specifically, we use theories from Renewal process literature to model the effect of N people as a superposition of "Renewal-type" processes. We then derive the Probability Mass Function (PMF) of

the inter-event times based on this model and use it to estimate the number of people using a maximum likelihood (ML) estimator. It is noteworthy that no existing work has shown the relationship between inter-event times and the total number of people. We extensively validate our framework using 44 real experiments in five different areas on our campus, three classrooms, a conference room, and a hallway. More specifically, we show that we can estimate up to and including 20 people with an error of 2 people or less 100% of the time and with an error of 1 person or less 75% of the time. Our experiments further include areas with different wall materials, such as concrete, plaster, and wood, to validate the robustness of our approach. To the best of our knowledge, this is the first demonstration of crowd counting through walls.

1.3 Joint Crowd Counting and Crowd Speed Estimation

In the last part of this thesis, we propose a framework that can estimate the occupancy attributes of an area, including the speed of a crowd when traversing the area, the arrival/departure rate into/out of the area, or the total number of people in the area, using only the received signal strength (RSSI) of two WiFi links in the area of interest, and without relying on people to carry any device (i.e., passively). Since a person may not have a constant speed in an area, in this thesis "speed estimation" refers to estimating the *average speed* of the people, where the average is the spatial average of the speed of a person in that particular area. In other words, people can stop several times in an area, or change their instantaneous speed. We are then interested in estimating their average speed, which is area-dependent and can thus reveal valuable information about an area. We next summarize the related work and our contributions.

Infrared-based approaches: Infrared (IR) sensors are mainly used for occupancy detection by sensing the motion of the occupants [3, 45, 46]. IR sensors located at the entrances/exits can also count the number of people entering and exiting the area [47]. Recently, IR sensors are also used to estimate the number of people in an area, without relying on door counters [48]. However, they are limited to counting up to 8 people in the area. More recent work also classifies the walking speed of a single person in an area based on IR sensors [47, 49]. However, there is no work based on IR sensors that can estimate the speed of a crowd (i.e., estimate the speed beyond one person), or count the number of people beyond 8.

Vision-based approaches: Vision-based methods can be potentially used to estimate the occupancy attributes of an area [28, 29, 50]. This involves continuous recording of an area, using cameras, followed by computer-vision algorithms for processing the videos. However, while consumers are fine with security cameras being probed in an on-demand manner for security purposes, serious privacy concerns arise when cameras are utilized in public places to analyze customer behaviors. For instance, a recent survey on retail shoppers [51] revealed that 75% of the people who understood the capabilities of vision-based tracking technologies found it intrusive for retails to track their behavior using such a technology. Furthermore, employing such tracking techniques could lead to shoppers choosing not to visit the corresponding stores [2]. In summary, vision-based occupancy estimation methods have the major drawback of privacy violation. Furthermore, they can only estimate the occupancy attributes in the areas that are in the direct line-of-sight of the cameras, while Radio Frequency (RF) based approaches have a through-wall sensing capability.

Device-based active RF approaches: The device-based active methods depend on the RF signals transmitted from a device carried by people in the area to assess the occupancy attributes [38, 52, 53]. However, these methods require the shoppers to carry a

wireless device, or an on-body sensor, which limits their applicability. More importantly, if a store is to use shoppers' devices to gather store analytics, it can only gather crude, low resolution tracking data, based on monitoring which router the device is connected to in the store (e.g., this data may not directly translate to speed estimation in different aisles). Even then, serious privacy concerns limit the applicability of such an approach in public places. For instance, Nordstrom, a clothing company which implemented an active WiFi-based in-store tracking technology to analyze the behavior of their customers, withdrew it due to privacy concerns of the shoppers [54]. Furthermore, a recent survey on active WiFi tracking technology [2] revealed that 80% of the shoppers do not like to be tracked based on their smartphones, while 43% do not want to shop at a store that employs active WiFi tracking technology.

Device-free passive RF approaches: The device-free passive methods, on the other hand, leverage the interaction of RF signals with the pedestrians and hence do not require the pedestrians to carry any device. In this manner, they can preserve the privacy. For instance, [40, 42, 43] use the variations in the WiFi RSSI signals, caused by people, to estimate the number of people. [44] uses channel state information (CSI) measurements and its corresponding variations for counting. However, these methods rely on extensive prior calibrations to the extent of running an actual experiment with several people walking in the area. They further require several wireless links, and cannot handle time-varying number of people in the area. [55] estimates the number of people in an area by minimizing the required prior calibration. However, they have to assume the speed of the people. In terms of speed estimation, some recent work started to estimate the speed of people in a device-free manner. For instance, [56] estimates the speed of a single person walking in a circle of radius 2 m, based on the RSSI measurements of a mobile phone located at the center of the circle. [57] classifies the speed of a single person based on the FM radio receivers. However, all these methods require an extensive prior

training phase and are limited to a single person. In [58], RSSI measurements of several WiFi links are used to track up to 4 people walking in the same area. Such an approach can in principle be extended towards speed estimation. However, this and other work on tracking typically have to assume very few people (less than 5). Moreover, in order to estimate the speed of a crowd of pedestrians, there is no need to track every individual, as we shall see in this thesis. In summary, to the best of our knowledge, there is no work in the literature that can estimate the speed of a crowd passively. Furthermore, there is no work that can jointly estimate the speed and total number/rate of arrival of people.

In this dissertation, we propose a framework to estimate both the crowd speed and crowd count, passively, and by using only a pair of WiFi links in the area. We then extend our framework to estimate the speed of people in the adjacent regions where there may not be WiFi coverage. Furthermore, we propose to use only the RSSI measurements of WiFi links which can be measured with any generic off-the-shelf device. We next summarize our main contributions in this area.

Contributions:

- We mathematically characterize the cross-correlation between two WiFi link measurements and show that it contains key information about the crowd speed in the area.
- We mathematically characterize the probability of crossing a link and explicitly show its dependency on the total number of people for the scenario of Fig. 1.3 (left), and on the rate of arrival of people for the scenario of Fig. 1.3 (right). Our mathematical characterization is general in the sense that it can include any type of motion patterns dictated by the environment.
- We implement a framework to estimate the crowd speed, total number of people, and rate of arrival of people in an area, using a pair of WiFi links, and validate its performance using a total of 51 experiments, in both indoor and outdoor areas, with

up to 20 people, and show that our framework can accurately estimate the occupancy attributes of an area in a device-free manner.

- We deploy our framework in an aisle of a local retail store, Costco, and estimate the behavior of shoppers in the aisle.

- We extend our framework to estimate the speed of crowd in the adjacent regions where there may not be any WiFi coverage. We conducted a total of 108 experiments, with up to 10 people walking in both an indoor and an outdoor area that has two regions, with a variety of speeds per region, and show that our approach can accurately estimate the speeds of pedestrians in the two adjacent regions.

Chapter 2

Robotic Through-Wall Imaging

In this chapter, we consider a scenario where a number of unmanned vehicles are tasked with seeing a completely unknown area behind thick walls, based on only wireless power measurements using WLAN cards. We show that a proper modeling of wave propagation that considers scattering and other propagation phenomena can result in high-resolution images of the unknown area. More specifically, we develop a theoretical and experimental framework for this problem based on Rytov wave models and integrate it with sparse signal processing and robotic path planning. Our experimental results show high-resolution imaging of three different areas, validating the proposed framework. Moreover, they show considerable performance improvement over the state-of-the-art that only considers the Line Of Sight (LOS) path, allowing us to image more complex areas not possible before. Finally, we show the impact of robot positioning and antenna alignment errors on our see-through imaging framework.

This chapter is organized as follows. In Section 2.1, we mathematically formulate our imaging problem based on Rytov wave approximation. In Section 2.2, we pose the resulting optimization problems and discuss how to solve them based on total variation minimization. In Section 2.3, we introduce the hardware and software structures of our experimental robotic platform, which allows for more autonomy in WiFi measurement collection. In Section 2.4, we then present our imaging results of three different areas

and show the impact of robot positioning and antenna alignment errors.

2.1 Problem Formulation

Consider a completely unknown workspace $\mathbf{D} \subset \mathbb{R}^3$. Let $\mathbf{D}^{\text{out}}$ be the complement of $\mathbf{D}$, i.e., $\mathbf{D}^{\text{out}} = \mathbb{R}^3 \setminus \mathbf{D}$. We consider a scenario where a group of robots in $\mathbf{D}^{\text{out}}$ are tasked with imaging the area $\mathbf{D}$ by using only WiFi. In other words, the goal is to reconstruct $\mathbf{D}$, i.e., to determine the shapes and locations of the objects in $\mathbf{D}$ based on only a small number of WiFi measurements. We are furthermore interested in see-through imaging, i.e., the area of interest can have several occluded parts, like parts completely behind concrete walls and thus invisible to any node outside. Fig. 1.1 shows an example of our considered scenario. The red superimposed volume marks the area that the two unmanned vehicles are interested in imaging but that is completely unknown to them. The area has several occluded parts, such as the parts blocked by the outer concrete wall, which is highly attenuating. Note that both empty and full spaces inside the red volume as well as its outer surfaces are all unknown to the robots and need to be imaged. The robots only have WiFi for imaging. As the robots move outside of $\mathbf{D}$, one robot measures the received signal power from the transmissions of the other robot. The unknown area $\mathbf{D}$ then interacts with each transmission, as dictated by the locations and properties of its objects, leaving its impact on each reception. The robots then need to image the structure based on all the receptions.

In this section, we start with the volume integral wave equation and discuss how it can be linearized and solved under certain assumptions, developing the system models that we shall utilize later for our imaging. The readers are referred to [19, 59] for more details on the wave propagation modeling.

2.1.1 Volume Integral Equations [19]

Let $\mathbf{E}(\mathbf{r})$ be the electric field, $\mathbf{J}(\mathbf{r})$ be the current density, $\epsilon(\mathbf{r})$ be the electric permittivity, and $\mu(\mathbf{r})$ be the magnetic permeability at $\mathbf{r} \in \mathbb{R}^3$, where $\mathbf{r}$ is the position vector in the spherical coordinates.[1] Then, we have the following volume integral equation relating the electric field to the current source and objects in $\mathbf{D}$ [19]

$$\begin{aligned}\mathbf{E}(\mathbf{r}) = j\omega\mu_0 \iiint_{\mathbb{R}^3} \vec{\mathbf{G}}(\mathbf{r},\mathbf{r}') \bullet \mathbf{J}(\mathbf{r}')\, dv' \\ + \iiint_{\mathbb{R}^3} \vec{\mathbf{G}}(\mathbf{r},\mathbf{r}') \bullet (O(\mathbf{r}')\mathbf{E}(\mathbf{r}'))\, dv',\end{aligned} \tag{2.1}$$

where $\vec{\mathbf{G}}(\mathbf{r},\mathbf{r}')$ is the dyadic Green's function given by

$$\vec{\mathbf{G}}(\mathbf{r},\mathbf{r}') = \left(I + \frac{\nabla\nabla}{k_0^2}\right) g(\mathbf{r},\mathbf{r}'), \tag{2.2}$$

$$g(\mathbf{r},\mathbf{r}') = \frac{e^{jk_0|\mathbf{r}-\mathbf{r}'|}}{4\pi|\mathbf{r}-\mathbf{r}'|}, \tag{2.3}$$

$O(\mathbf{r}) = k^2(\mathbf{r}) - k_0^2$ denotes the material property of the object at position $\mathbf{r}$, $k_0^2 = \omega^2\epsilon_0\mu_0$ denotes the wavenumber of the free space,[2] $k^2(\mathbf{r}) = \omega^2\mu_0\epsilon(\mathbf{r})$ denotes the wavenumber of the medium at $\mathbf{r}$, ϵ_0 and μ_0 are the permittivity and permeability of the free space respectively, ω is the angular frequency, and $\bullet$ denotes the vector dot product. The robots are then interested in learning $O(\mathbf{r})$, for $\mathbf{r} \in \mathbf{D}$, as it carries the information of the location/material property of the objects in the workspace. Note that (2.1) is valid for any inhomogeneous, isotropic, and non-magnetic media. Also, $O(\mathbf{r})\mathbf{E}(\mathbf{r})$ is the equivalent current induced in the object at $\mathbf{r}$. This induced current in turn produces an electric field. The total field is then the sum of the electric field due to the current in the transmit antenna, the first term on the right hand side (RHS) of (2.1), and the electric field due

[1] In this dissertation, single-frequency operation is assumed and all the materials are considered isotropic and non-magnetic, i.e., $\mu(\mathbf{r}) = \mu_0$, for all $\mathbf{r} \in \mathbb{R}^3$, where μ_0 is the permeability of the freespace.

[2] In this dissertation, free space refers to the case where there is no object.

to the induced current in the objects (the second term on the RHS of (2.1)).

First, we start by assuming free space in $\mathbf{D}^{\text{out}}$. Then, $\epsilon(\mathbf{r}) = \epsilon_0$, for $\mathbf{r} \in \mathbf{D}^{\text{out}}$, resulting in $k^2(\mathbf{r}) = k_0^2$ and $O(\mathbf{r}) \equiv 0$, for $\mathbf{r} \in \mathbf{D}^{\text{out}}$. When there are no objects in $\mathbf{D}$, we have $k^2(\mathbf{r}) = k_0^2$ and $O(\mathbf{r}) \equiv 0$, for all $\mathbf{r} \in \mathbb{R}^3$, and the second term on the RHS of (2.1) vanishes. This means that the first term is the incident field when there are no objects in $\mathbf{D}$ and the second term is the result of scattering from the objects in $\mathbf{D}$. By denoting the first term on the RHS of (2.1) as $\mathbf{E}_{\text{inc}}(\mathbf{r})$, we then get

$$\mathbf{E}(\mathbf{r}) = \mathbf{E}_{\text{inc}}(\mathbf{r}) + \iiint_{\mathbf{D}} \vec{\mathbf{G}}(\mathbf{r}, \mathbf{r}') \bullet (O(\mathbf{r}')\mathbf{E}(\mathbf{r}'))\, dv', \tag{2.4}$$

where $\vec{\mathbf{G}}(\mathbf{r}, \mathbf{r}')$ is a second-order tensor and can be represented as the following 3×3 matrix in the Cartesian coordinates:

$$\vec{\mathbf{G}}(\mathbf{r}, \mathbf{r}') = \begin{bmatrix} G_{xx}(\mathbf{r}, \mathbf{r}') & G_{xy}(\mathbf{r}, \mathbf{r}') & G_{xz}(\mathbf{r}, \mathbf{r}') \\ G_{yx}(\mathbf{r}, \mathbf{r}') & G_{yy}(\mathbf{r}, \mathbf{r}') & G_{yz}(\mathbf{r}, \mathbf{r}') \\ G_{zx}(\mathbf{r}, \mathbf{r}') & G_{zy}(\mathbf{r}, \mathbf{r}') & G_{zz}(\mathbf{r}, \mathbf{r}') \end{bmatrix}.$$

In reality, there will be objects in $\mathbf{D}^{\text{out}}$. Then, $\mathbf{E}_{\text{inc}}$ denotes the field when there are no objects in $\mathbf{D}$.[3] Without loss of generality, we assume that the transceiver antennas are linearly polarized in the z-direction. This means that we only need to calculate the z-component of the electric field, which depends on the last row of $\vec{\mathbf{G}}(\mathbf{r}, \mathbf{r}')$. Let $\mathbf{J}_{\text{eq}}(\mathbf{r}) = [J_{\text{eq}}^x \; J_{\text{eq}}^y \; J_{\text{eq}}^z]^T = O(\mathbf{r})\mathbf{E}(\mathbf{r})$. We further assume near-zero cross-polarized components J_{eq}^x and J_{eq}^y and take $\mathbf{J}_{\text{eq}}(\mathbf{r}) \approxeq [0 \; 0 \; J_{\text{eq}}^z]^T$. This approximation is reported to have a negligible effect [60]. By using this approximation in (2.4) and only taking the z-component, we

[3] In our experiments, we will not have access to the exact incident field when there is nothing in $\mathbf{D}$. Thus, the two robots make a few measurements in $\mathbf{D}^{\text{out}}$ where there are no objects in between them to estimate and remove the impact of $\mathbf{E}_{\text{inc}}$. If the robots have already imaged parts of $\mathbf{D}^{\text{out}}$, that knowledge can be easily incorporated to improve the performance.

get the following scalar equation:

$$E^z(\mathbf{r}) = E^z_{\text{inc}}(\mathbf{r}) + \iiint_{\mathbf{D}} G_{zz}(\mathbf{r}, \mathbf{r}')O(\mathbf{r}')E^z(\mathbf{r}')\, dv', \tag{2.5}$$

where $E^z(\mathbf{r})$ and $E^z_{\text{inc}}(\mathbf{r})$ are the z-components of $\mathbf{E}(\mathbf{r})$ and $\mathbf{E}_{\text{inc}}(\mathbf{r})$, respectively.

2.1.2 Linearizing Approximations

In (2.5), the received electric field $E^z(\mathbf{r})$ is a non-linear function of the object function $O(\mathbf{r})$, since $E^z(\mathbf{r}')$ inside the integral also depends on $O(\mathbf{r})$. This nonlinearity is due to the multiple scattering effect in the object region [59]. Thus, we next use approximations that make (2.5) linear and easy to solve under the setting of sparse signal processing.

Line Of Sight-Based Modeling [19, 61]

A simple way of modeling the receptions is to only consider the LOS path from the transmitter to the receiver and the impact of the objects on this path. This model has been heavily utilized in the literature due to its simplicity [61]. However, it results in a considerable modeling gap for see-through imaging since it does not include important propagation phenomena such as scattering. In this part, we summarize the LOS model in the context of wave equations.

At very high frequencies, such as in X-ray, the wave can be assumed to travel in straight lines with negligible reflections and diffractions along its path [19]. Then, the solution to (2.5) is given as follows by using Wentzel Kramers Brillouin (WKB) approximation,[4]

$$E(\mathbf{r}) = \frac{C}{\sqrt{\alpha(\mathbf{r})}} e^{j\omega \int_{\mathbb{L}_{T\to R}} \alpha(\mathbf{r}')\, d\mathbf{r}'}, \qquad \text{WKB Approximation} \tag{2.6}$$

[4]Here, the field is along the z-direction, as explained before. From this point on, superscript z is dropped for notational convenience.

where $\alpha(\mathbf{r})$ is a complex number that represents the slowness of the medium at $\mathbf{r}$ and is related to $k(\mathbf{r})$, $\int_{\mathbb{L}_{T\to R}}$ is a line integral along the line joining the positions of the transmitter and the receiver, and c is a constant that depends on the transmitted signal power.

It can be seen that the loss incurred by the ray is linearly related to the objects along that path, resulting in a linear relationship between the received power and the objects, as we shall see. This approximation is the base for X-ray tomography [62]. However, the underlying assumption of this method is not valid at lower frequencies, like microwave frequencies, due to the non-negligible diffraction effects [63]. [61,64], proposed a see-through wall RF-based imaging framework based on this approximation. In this dissertation, our goal is to use a considerably more comprehensive modeling of the receptions (which has been a bottleneck in see-through imaging) by tapping into the wave literature. We show that by addressing the modeling of the receptions through using Rytov wave approximation, we can image areas not possible before.

Rytov Approximation [19]

In general, the field inside any inhomogeneous media can be expressed as

$$E(\mathbf{r}) = e^{j\psi(\mathbf{r})}, \tag{2.7}$$

and satisfies

$$[\nabla^2 + k^2(\mathbf{r})]E(\mathbf{r}) = 0, \tag{2.8}$$

where $\psi(\mathbf{r})$ is a complex phase term. It can then be shown that the solution to (2.8) can be approximated as follows:

$$E(\mathbf{r}) = E_{\text{inc}}(\mathbf{r})e^{j\phi(\mathbf{r})}, \qquad \text{Rytov Approximation} \tag{2.9}$$

where

$$\phi(\mathbf{r}) = \frac{-j}{E_{\text{inc}}(\mathbf{r})} \iiint_{\mathbf{D}} g(\mathbf{r}, \mathbf{r}') O(\mathbf{r}') E_{\text{inc}}(\mathbf{r}')\, dv'. \tag{2.10}$$

The validity of Rytov approximation is established by dimensional analysis in [19] and is accurate at high frequencies,[5] if

$$\delta_\epsilon(\mathbf{r}) \triangleq \frac{\epsilon(\mathbf{r})}{\epsilon_0} - 1 \ll 1,$$

where $\delta_\epsilon(\mathbf{r})$ is the normalized deviation of the electric permittivity from the free space. At lower frequencies, the condition for validity of the Rytov approximation becomes

$$(k_0 L_{\text{obj}})^2 \delta_\epsilon(\mathbf{r}) \ll 1,$$

where L_{obj} is the order of the dimension of the objects. In our case, with a frequency of 2.4 GHz and L_{obj} of the order of 1 m, we satisfy the condition of high frequency, except at the boundaries of the objects, where there are abrupt changes in the material.

For the sake of completion, a more commonly-used linearizing approximation, called Born approximation, is summarized in the appendix A. Rytov approximation is reported to be more relaxed than the Born approximation at higher frequencies [19]. Also, Rytov approximation lends itself to a simple linear form, when we only know the magnitude of the received electric field, as described next. Thus, in this dissertation, we focus on Rytov wave modeling.

[5] In this thesis, high frequency refers to the frequencies at which the size of inhomogeneity of objects is much larger than the wavelength.

2.1.3 Intensity-Only Rytov Approximation

In the aforementioned equations, both magnitude and phase of the received field are needed. In this dissertation, however, we are interested in imaging based on only the received signal power.

Then, by conjugating (2.9), we get

$$E^*(\mathbf{r}) = E^*_{\text{inc}}(\mathbf{r})e^{-j\phi^*(\mathbf{r})}. \tag{2.11}$$

From (2.9) and (2.11), we then have

$$|E(\mathbf{r})|^2 = |E_{\text{inc}}(\mathbf{r})|^2 e^{-2\text{Imag}(\phi(\mathbf{r}))}, \tag{2.12}$$

where Imag(.) and |.| denote the imaginary part and the magnitude of the argument, respectively. Since the received power[6] is proportional to the square of the magnitude of the received field, we have the following equation by taking logarithms on both sides of (2.12):

$$P_{\text{r}}(\mathbf{r})(\text{dBm}) = P_{\text{inc}}(\mathbf{r})(\text{dBm}) + 10\log_{10}(e^{-2})\text{Imag}(\phi(\mathbf{r})), \tag{2.13}$$

where $P_{\text{r}}(\mathbf{r})(\text{dBm}) = 10\log_{10}\left(\frac{|E(\mathbf{r})|^2}{120\pi\times 10^{-3}}\right)$ is the received power in dBm at $\mathbf{r}$, and $P_{\text{inc}}(\mathbf{r})(\text{dBm}) = 10\log_{10}\left(\frac{|E_{\text{inc}}(\mathbf{r})|^2}{120\pi\times 10^{-3}}\right)$ is the power incident in dBm at $\mathbf{r}$ when there are no objects.

To solve (2.12) for object $O(\mathbf{r})$, we discretize $\mathbf{D}$ into N_{D} equal-volume cubic cells. The position of each cell is represented by its center position vector $\mathbf{r}_n$, for $n \in \{1, 2, \cdots, N_{\text{D}}\}$. The electric field and the object properties are assumed to be constant within each cell.

[6]This is the received power by an isotropic antenna. For a directional antenna, this should be multiplied by the gain of the antenna.

We then have

$$O(\mathbf{r}) = \sum_{n=1}^{N_\mathrm{D}} O(\mathbf{r}_n) C_n, \tag{2.14}$$

$$E_\mathrm{inc}(\mathbf{r}) = \sum_{n=1}^{N_\mathrm{D}} E_\mathrm{inc}(\mathbf{r}_n) C_n, \tag{2.15}$$

where $\mathbf{r}, \mathbf{r}_n \in \mathbf{D}$, C_n is a pulse basis function which is one inside cell n and zero outside. By substituting (2.14) and (2.15) into (2.10), we get

$$\begin{aligned}\phi(\mathbf{r}) =& \frac{-j}{E_\mathrm{inc}(\mathbf{r})} \sum_{n=1}^{N_\mathrm{D}} O(\mathbf{r}_n) E_\mathrm{inc}(\mathbf{r}_n) \iiint_{V_n} g(\mathbf{r}, \mathbf{r}')\, dv' \\ \approxeq& \frac{-j}{E_\mathrm{inc}(\mathbf{r})} \sum_{n=1}^{N_\mathrm{D}} g(\mathbf{r}, \mathbf{r}_n) O(\mathbf{r}_n) E_\mathrm{inc}(\mathbf{r}_n) \Delta V,\end{aligned} \tag{2.16}$$

where

$$\iiint_{V_n} g(\mathbf{r}, \mathbf{r}')\, dv' \approxeq g(\mathbf{r}, \mathbf{r}_n) \Delta V, \tag{2.17}$$

V_n is the n^th cell and ΔV is the volume of each cell. Note that C_n is not included in (2.16) since we are evaluating the integral inside cell n where C_n is one.

Let $(\mathbf{p}_i, \mathbf{q}_i)$, for $\mathbf{p}_i, \mathbf{q}_i \in \mathbf{D}^\mathrm{out}$, denote the transmitter and receiver position pair where the i^th measurement is taken. Also, let $\Phi = [\phi_{\mathbf{p}_1}(\mathbf{q}_1)\ \phi_{\mathbf{p}_2}(\mathbf{q}_2)\ \cdots \phi_{\mathbf{p}_M}(\mathbf{q}_M)]^T$, where M is the number of measurements, $\phi_{\mathbf{p}_i}(\mathbf{q}_i) = \frac{-j}{E_{\mathrm{inc},\mathbf{p}_i}(\mathbf{q}_i)} \sum_{n=1}^{N_\mathrm{D}} g(\mathbf{q}_i, \mathbf{r}_n) O(\mathbf{r}_n) E_{\mathrm{inc},\mathbf{p}_i}(\mathbf{r}_n) \Delta V$, and $E_{\mathrm{inc},\mathbf{p}_i}(\mathbf{r}_n)$ is the incident field at $\mathbf{r}_n$ when the transmitter is at $\mathbf{p}_i$. Then, we have

$$\Phi = -jF\ O, \tag{2.18}$$

where F is an $M \times N_\mathrm{D}$ matrix with $F_{i,j} = \frac{g(\mathbf{q}_i, \mathbf{r}_j) E_{\mathrm{inc},\mathbf{p}_i}(\mathbf{r}_j) \Delta V}{E_{\mathrm{inc},\mathbf{p}_i}(\mathbf{q}_i)}$ and $O = [O(\mathbf{r}_1)\ O(\mathbf{r}_2)\ \cdots$

$O(\mathbf{r}_{N_\mathrm{D}})]^T$. Using (2.13) for each measurement and stacking them together, we get

$$\mathbf{P}_{\mathrm{ryt}} = \mathrm{Imag}(\Phi), \tag{2.19}$$

where $\mathbf{P}_{\mathrm{ryt}} = \frac{\mathbf{P}_\mathrm{r}(\mathrm{dBm}) - \mathbf{P}_\mathrm{inc}(\mathrm{dBm})}{10\log_{10}(e^{-2})}$, $\mathbf{P}_\mathrm{r}(\mathrm{dBm}) = [P_{\mathrm{r},\mathbf{p}_1}(\mathbf{q}_1)(\mathrm{dBm})\ P_{\mathrm{r},\mathbf{p}_2}(\mathbf{q}_2)(\mathrm{dBm})\ \cdots\ P_{\mathrm{r},\mathbf{p}_M}(\mathbf{q}_M)(\mathrm{dBm})]^T$, $\mathbf{P}_\mathrm{inc}(\mathrm{dBm}) = [P_{\mathrm{inc},\mathbf{p}_1}(\mathbf{q}_1)(\mathrm{dBm})\ P_{\mathrm{inc},\mathbf{p}_2}(\mathbf{q}_2)(\mathrm{dBm})\ \cdots\ P_{\mathrm{inc},\mathbf{p}_M}(\mathbf{q}_M)(\mathrm{dBm})]^T$, and $P_{\mathrm{r},\mathbf{p}_i}(\mathbf{q}_i)(\mathrm{dBm})$ and $P_{\mathrm{inc},\mathbf{p}_i}(\mathbf{q}_i)(\mathrm{dBm})$ are the received power and incident power corresponding to the transmitter and receiver pair $(\mathbf{p}_i, \mathbf{q}_i)$, respectively. Using (2.18) and (2.19), we get

$$\mathbf{P}_{\mathrm{ryt}} = \mathrm{Real}(FO) = F_\mathrm{R}O_\mathrm{R} + F_\mathrm{I}O_\mathrm{I}, \tag{2.20}$$

where Real(.) is the real part of the argument, and F_R, F_I, O_R and O_I are the real part of F, imaginary part of F, real part of O, and imaginary part of O, respectively. This can be further simplified by noting that $F_\mathrm{R}O_\mathrm{R} \gg F_\mathrm{I}O_\mathrm{I}$ [65]. Therefore, the above equation becomes

$$\mathbf{P}_{\mathrm{ryt}} \approxeq F_\mathrm{R}O_\mathrm{R}, \tag{2.21}$$

which is what we shall use for our RF-based robotic imaging.

2.1.4 Intensity-Only LOS Approximation

Starting from (2.6) and following similar steps to the intensity-only Rytov approximation, we get:

$$\begin{aligned} P_\mathrm{r}(\mathbf{r})(\mathrm{dBm}) =& P_\mathrm{inc}(\mathbf{r})(\mathrm{dBm}) \\ &- 10\log_{10}(e^{-2})\omega \int_{\mathbb{L}_{T\to R}} \mathrm{Imag}(\alpha(\mathbf{r}'))\, d\mathbf{r}', \end{aligned} \tag{2.22}$$

where the integration is the line integral along the line joining the positions of the transmitter and receiver, and $\mathbf{r}$ is the position of the receiver. Denoting $\mathbf{P}_{\text{LOS}} = \frac{\mathbf{P}_{\text{r}}(\text{dBm}) - \mathbf{P}_{\text{inc}}(\text{dBm})}{10\log_{10}(e^{-2})}$ and stacking M measurements together, we have

$$\mathbf{P}_{\text{LOS}} = A_{\text{LOS}}\Gamma, \tag{2.23}$$

where A_{LOS} is a matrix of size $M \times N_{\text{D}}$ with its entry $A_{\text{LOS}i,j} = 1$ if the j^{th} cell is along the line joining the transmitter and receiver of the i^{th} measurement, and $A_{i,j} = 0$ otherwise, $\Gamma = [\alpha_{\text{I}}(\mathbf{r}_1)\ \alpha_{\text{I}}(\mathbf{r}_2) \cdots \alpha_{\text{I}}(\mathbf{r}_{N\text{D}})]^T$, and $\alpha_{\text{I}}(.) = \text{Imag}(\alpha(.))$.

Equation (2.23) is what we then utilize in our setup when showing the performance of the state of the art.

2.2 Brief Overview of Sparse Signal Processing

In the formulations of the Rytov and LOS approximations in Section 2.1, we have a system of linear equations to solve for each approach. However, the system is severely underdetermined as the number of wireless measurements typically amount to a small percentage of the number of unknowns. More specifically, let $\mathbf{x} \in \mathbb{R}^{N_{\text{D}}}$ be a general unknown signal, $\mathbf{y} \in \mathbb{R}^M$ be the measurement vector, and $\mathbf{y} = B_{\text{obs}}\mathbf{x}$ be the observation model, where B_{obs} is an $M \times N_{\text{D}}$ observation matrix. We consider the case where $N_{\text{D}} \gg M$, i.e., the number of unknowns is much larger than the number of measurements. Thus, it is a severely underdetermined problem which cannot be solved uniquely for $\mathbf{x}$ given $\mathbf{y}$. In this section, we briefly summarize how sparse signal processing can be utilized to solve this problem.

Suppose $\mathbf{x}$ can be represented as a sparse vector in another domain as follows: $\mathbf{x} = \Theta\mathbf{X}$, where Θ is an invertible matrix and $\mathbf{X}$ is S-sparse, i.e., $\text{card}(\text{supp}(\mathbf{X})) \ll N_{\text{D}}$, where

card(.) denotes the cardinality of the argument and supp(.) denotes the set of indices of non-zero elements of the argument. Then, we have $\mathbf{y} = K\mathbf{X}$, where $K = B_{\text{obs}}\Theta$ and $\mathbf{X}$ has a much smaller number of the non-zero elements than $\mathbf{x}$. In general, the solution to the above problem is obtained by solving the following non-convex combinatorial problem [66]:

$$\text{minimize} \quad \|\mathbf{X}\|_0, \quad \text{subject to} \quad \mathbf{y} = K\mathbf{X}. \tag{2.24}$$

Since solving (2.24) is computationally-intensive and impractical, considerable research has been devoted towards developing approximated solutions for (2.24).

In our case, we are interested in imaging and localization of the objects in an area. Spatial variations of the objects in a given area are typically sparse. We thus take advantage of the sparsity of the spatial variations to solve our under-determined system.[7] More specifically, let $R = [R_{i,j}]$ denote an $m \times n$ matrix that represents the unknown space. Since we are interested in the spatial variations of R, let

$$D_{h,i,j} = \begin{cases} R_{i+1,j} - R_{i,j} & \text{if } 1 \leq i < m, \\ R_{i,j} - R_{1,j} & \text{if } i = m, \end{cases} \quad \text{and}$$

$$D_{v,i,j} = \begin{cases} R_{i,j+1} - R_{i,j} & \text{if } 1 \leq j < n, \\ R_{i,j} - R_{i,1} & \text{if } j = n. \end{cases}$$

Then, the Total Variation (TV) of R is defined as:

$$\text{TV}(R) = \sum_{i,j} \|\text{D}_{i,j}(R)\|, \tag{2.25}$$

where $\text{D}_{i,j}(R) = [D_{h,i,j}\ D_{v,i,j}]$, and $\|.\|$ can represent either l_1 or l_2 norm. TV minimiza-

[7] It is also possible to solve an l_1 convex relaxation of (2.24). However, our past analysis has indicated a better performance with spatial variation minimization [61].

tion then solves the following convex optimization problem:

$$\text{minimize} \quad \text{TV}(R), \quad \text{subject to} \quad \mathbf{y} = K\mathbf{X}. \tag{2.26}$$

In the context of the current problem formulation, $\mathbf{X}$ represents the object map $\mathbf{D}$, R represents the spatial variations of $\mathbf{X}$, K represents the observation model, i.e., $K = F_R$ for the Rytov approach and $K = A_{\text{LOS}}$ for the LOS approach, and $\mathbf{y}$ represents the received power (after removing path loss). In solving (2.26), l_1 or l_2 norm results in a similar reconstruction [67]. Thus, unless otherwise stated, all results of this thesis are based on l_1 norm.

To solve the general compressive sensing problem of (2.26) robustly and efficiently, TVAL3 (TV Minimization by Augmented Lagrangian and Alternating Direction Algorithms) is proposed in [68]. TVAL3 is a MATLAB-based solver that solves (2.26) by minimizing the augmented Lagrangian function using an alternating minimization scheme [69]. The augmented Lagrangian function includes coefficients which determine the relative importance of the terms $\text{TV}(R)$ and $\|\mathbf{y} - K\mathbf{X}\|$ in (2.26). The readers are referred to [68] for more details on TVAL3. We use TVAL3 for all the experimental results of this dissertation.

2.3 Experiment Setup

In this section, we briefly describe our enabling experimental testbed. In our setup, the robots can take channel measurements over a given route autonomously, and without any coordination between themselves or stopping. More specifically, each robot travels a route autonomously and without any coordination with the other robot or positioning error correction. In the rest of this section, we describe the software and hardware aspects

of our testbed in more details.

In our setup, we use two Pioneer 3-AT (P3-AT) mobile robots from MobileRobots Inc. [70], each equipped with an onboard PC, and an IEEE 802.11g (WLAN) card. Each robot can simultaneously follow a given path and take the corresponding received signal strength measurements (RSSI) as it moves. The data is then stored and transferred back to a laptop at the end of the operation.

2.3.1 Hardware Architecture

P3-AT mobile robots [70] are designed for indoor, outdoor, and rough-terrain implementations. They feature an onboard PC104 and a Renesas SH7144-based micro-controller platform for control of the motors, actuators and sensors. By utilizing a C/C++ application programming interface (API) library provided by MobileRobots, users are able to program and control the robot via the micro-controller platform. Fig. 2.1 shows the P3-AT robot. We have furthermore utilized directional antennas for better imaging results. In order to hold the directional antennas, we have built an additional electromechanical fixture, as can be seen from Fig. 2.1. This antenna is rotated and positioned via a Hitec HA-7955TG digital servo mounted on the antenna fixture. Via a serial port, PWM values are passed from the onboard PC104 to a Digilent Cerebot II micro-controller on the side of the antenna frame. These PWM waveforms are then outputted to the Hitec Servo, specifying a range of 0 - 180 degree angle. We use a GD24-15 2.4 GHz parabolic grid antenna from Laird Technologies [71]. This model has a 15 dBi gain with 21 degree horizontal and 17 degree vertical beamwidth and is suitable for IEEE 802.11 b/g applications.

One of the robots has a D-Link WBR-1310 wireless router attached to its antenna. It constantly outputs a wireless signal for the other robot to measure the signal strength.

Figure 2.1: The figure shows a Pioneer 3-AT robot with the additionally-mounted servomechanism and a directional antenna.

The overall operation is overseen by a remote PC, which is in charge of passing the initial plan to the robots to execute, and collecting the final signal strength readings at the end of the operation. A block diagram of the hardware architecture of the robots is shown in Fig. 2.2.

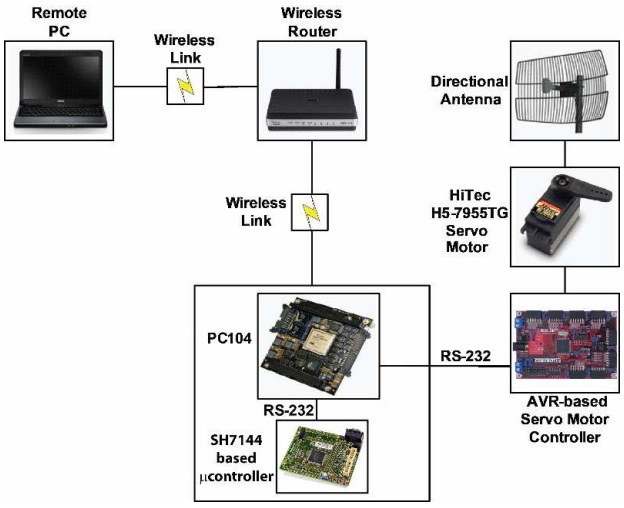

Figure 2.2: Block diagram of the hardware architecture of one of the robots.

2.3.2 Software Architecture

The overall software architecture of our system can be seen in Fig. 2.3. The software system is composed of two application layers, one running on a remote PC to control the experiment and one running on the robots themselves. The programs are developed in C++ using the ARIA library developed by MobileRobots. They communicate via a TCP/IP connection between the robot-side application, which acts as the server, and the PC-side application, which acts as the client. The remote PC is in charge of overseeing the whole operation and giving initial control commands and route information to the robots. The user can specify the route information involving the direction of movement, the length of the route and the coordinates of the starting positions of the robots. Next, we explain our software architecture in more details.

In order to synchronize all the operations - robot movement, antenna alignment and signal strength measurement, the robot execution is divided into four separate in-software threads: the antenna control thread, signal strength thread, motor control thread, and main thread, which respectively control the antenna rotation, manage the reading of the wireless signal strength, operate the motor such as in driving forward, and send the overall commands. The main thread initializes/finalizes other threads and communicates with the remote PC. Before a route begins, the main thread first creates the threads needed to run the other operations and freezes their operations using Mutex. It then receives the path information of both robots from the remote PC. This information is passed to the antenna control and signal strength threads, where it will be used to calculate when to read the signal strength, and how to rotate the antenna over the route to keep the antennas on both robots aligned. Once the threads are properly initialized, the path information is passed to the motor control thread to begin the operation. The measurements gathered by one robot will be stored on its PC and are transferred back

to the remote PC at the end of the operation. This is because any kind of TCP communication introduces unnecessary delays in the code during the measurements. It is necessary, however, to be able to control the robot movement and operation at all times from the remote PC in case of emergency. Therefore, the code is designed to maximize the autonomy and precision of the operation, through threading, while being able to shut down via remote control at any time. This is achieved with the main thread utilizing a polling approach.

2.3.3 Robot Positioning

Accurate positioning is considerably important as the robots need to constantly put a position stamp on the locations where they collect the channel measurements and further align their antennas based on the position estimates. In our setup, our robots utilize onboard gyroscopes and wheel encoders to constantly estimate their positions. Since we use a dead reckoning approach to localize our robots, timing is very important to the accuracy of position estimation. We thus employ precise timers in software to help the robot determine its own position as well as the position of the other robot based on the given speed. More specifically, when the motor control thread begins its operation, timers are simultaneously initiated in all the threads, allowing them to keep track of when and where they are in their operations. Also, the threads' Mutex are released, allowing the robots to move and take measurements.

It is important to note that once the robots start a route, there is no communication or coordination between them. Each robot constantly uses the set speed and timer information to estimate its own location as well as the location of the other robot for antenna alignment and measurement collection. Thus, all the measurements and alignments are naturally prone to positioning errors. Currently, we use speeds up to 10 cm/s. A sample

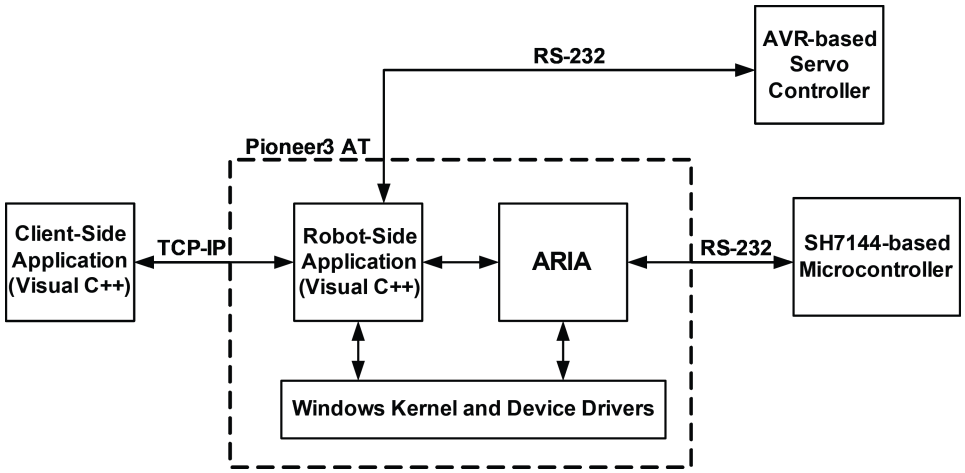

Figure 2.3: Software architecture of the robot platform.

route is shown in Fig. 2.4 (see the 0 degree angle route, for instance). Our current localization error is less than 2.5 cm per one meter of straight line movement, and our current considered routes typically span 10 - 20 meters. Additionally, the robot also experiences a drift from the given path. These robot positioning errors will also result in antenna alignment errors. In Section 2.4, we discuss the impact of both errors on our imaging results in details.

2.3.4 Robot Paths

So far, we have explained the hardware and software aspects of the experimental testbed. Next, we briefly explain the routes that the robots would take. More specifically, the transmitting and receiving robots move outside of $\mathbf{D}$, similar to how CT-scan is done, in parallel, along the lines that have an angle θ with the x-axis. This means that the line connecting the transmitter and receiver would ideally (in the absence of positioning errors) stay orthogonal to the line with angle θ. Sample routes along 0 and 45 degree angles are shown in Fig. 2.4. Both of the robots move with a same velocity of 10 cm/s and take measurements every 0.2 sec (i.e., measurements are taken with 2 cm resolution).

As explained earlier, there is no coordination between the robots when traveling a route. To speed up the operation, we currently manually move the robots from the end of one route to the beginning of another route. This part can also be automated as part of future work. Additionally, random wireless measurements, a term we introduced in [72], where the transmitter is stationary and the receiver moves along a given line, can also be used. In the next section, we only consider the case of parallel routes, as shown in Fig. 2.4. Readers are referred to [73] for more details and tradeoff analysis on using parallel or random routes in the context of LOS reception modeling.

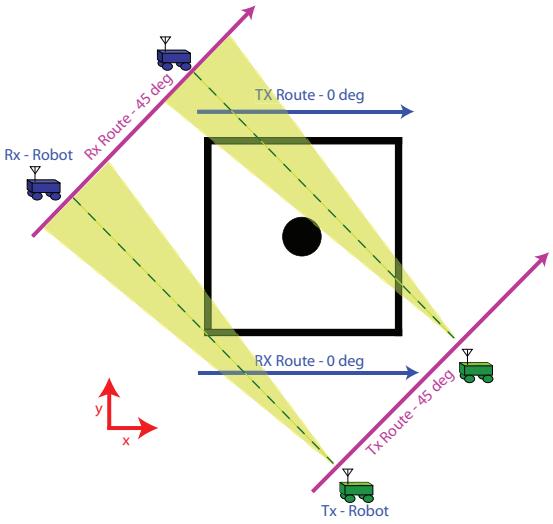

Figure 2.4: Sample routes for measurement collection are shown for 0 and 45 degree angles.

2.4 Experimental Results and Discussions

In this section, we show the results of see-through wall imaging with Rytov wave approximation and further compare them with the state of the art results based on LOS modeling. We consider three different areas, as shown in Fig. 2.7, 2.8 and 2.9 (top-left). We name these cases as follows for the purpose of referencing: T-shape, occluded cylinder, and occluded two columns. Two robots move outside of the area of interest and record the

signal strength. These measurements are then used to image the corresponding unknown regions using both Rytov and LOS approaches, as described in Section 2.1. Fig. 2.7, 2.8 and 2.9 further show the horizontal cuts of these areas. In this dissertation, we only consider 2D imaging, i.e., imaging a horizontal cut of the structure.

Fig. 2.5 shows a sample of the real measurement along the 0 degree line for the T-shape, with the distance-dependent path loss component. As mentioned previously, the distance-dependent path loss component does not contain any information about the objects. Thus, by making a few measurements in the same environment where there are no objects between the robots, it is estimated and removed. To compare how well the WKB (LOS modeling) and Rytov approximations match the real measurements, the simulated received signal loss using each approximation is plotted in Fig. 2.6 for the route along the 0 degree angle for the occluded cylinder structure. As can be seen, the Rytov approximation matches the real measurement considerably better than the LOS modeling.

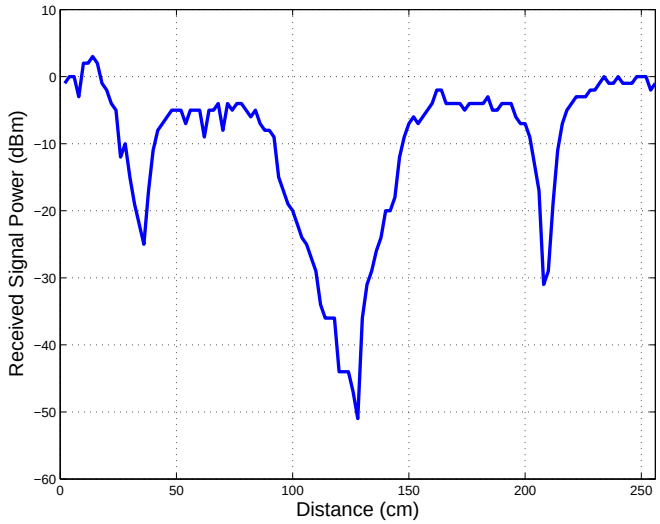

Figure 2.5: Real received signal power along the 0 degree line for the T-shape, with the distance-dependent path loss component removed.

Our imaging results for the T-shape, the occluded cylinder and the occluded two

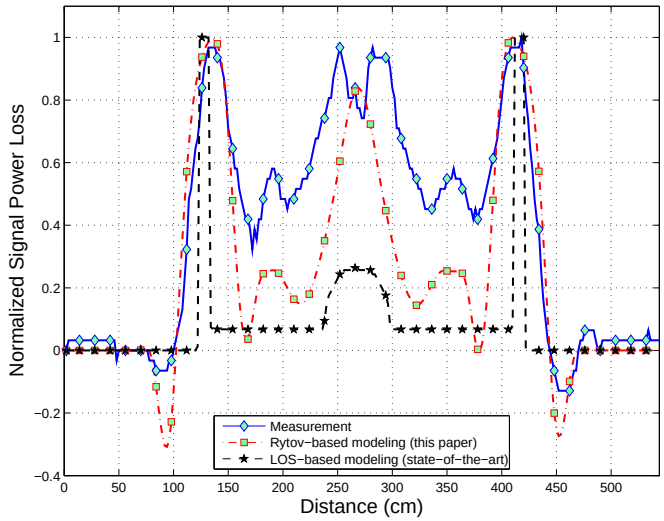

Figure 2.6: Comparisons of the Rytov and LOS approximations for the route along the 0 degree angle for the occluded cylinder. As can be seen, the Rytov approximation matches the real measurement considerably better than the LOS modeling through WKB approximation.

columns are shown in Fig. 2.7, 2.8 and 2.9 respectively. For the T-shape and the occluded cylinder, we have measurements along four angles of 0, 90, 45, and 135 degrees. For the occluded two columns we have measurements along five angles of 0, 90, 80, -10 and 10 degrees. The total measurements thus amount to only 20.12%, 4.7% and 2.6% for the T-shape, the occluded cylinder, and the occluded two columns respectively. Fig. 2.7 (left) shows the T-shape structure with its horizontal cut marked. This horizontal cut, which is the true original image that the robots need to construct, is an area of 0.64 m $\times$ 1.82 m, which results in 2912 unknowns to be estimated. Fig. 2.7 further shows the imaging results with both Rytov and LOS for this structure. As can be seen, Rytov provides a considerably better imaging quality, especially around the edges. The reconstructions after thresholding are also shown in Fig. 2.7, which uses the fact that we are interested in a black/white image that indicates absence/presence of objects (more details on this will follow soon).

Fig. 2.8 shows the imaging of the occluded cylinder. This area of interest is 2.98 m $\times$

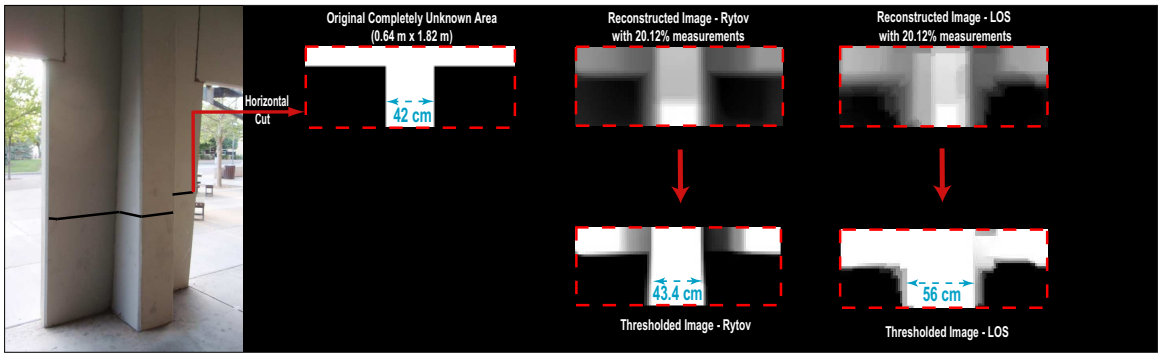

Figure 2.7: The left figures show the T-shape structure of interest that is completely unknown and needs to be imaged, as well as its horizontal cut (its dimension is 0.64 m $\times$ 1.82 m). The white areas in the true image indicate that there is an object while the black areas denote that there is nothing in those spots. Imaging results based on 20.12% measurements are shown for both Rytov and LOS approaches. Sample dimensions of the original and the reconstructed images are also shown. It can be seen that Rytov provides a considerably better imaging result.

2.98 m, amounting to 22201 unknowns to be estimated based on only 4.7% measurements. This structure is more challenging than the T-shape to reconstruct because 1) it is fully behind thick brick walls, and 2) it consists of materials with different properties (metal and brick). Similarly, we can see that Rytov provides a better imaging result for this structure as well, with the details reconstructed more accurately. Thresholded images are also shown.

Fig. 2.9 shows the imaging of the occluded two columns. This area of interest is 4.56 m $\times$ 5.74 m (amounting to 65436 unknowns) and is estimated only with 2.6% WiFi measurements. This structure is more challenging to image than both the T-shape and the occluded cylinder since 1) there are two columns close to each other, which results in a higher multipath and other propagation phenomena and, 2) smaller percentage of measurements are available for imaging (half of that used for the occluded cylinder). The figure shows the thresholded imaging results as well. More specifically, any value above 40% and below 20% of the maximum value is thresholded to the 40% and 20% values respectively (the same thresholding approach is used for the past two areas). As can be

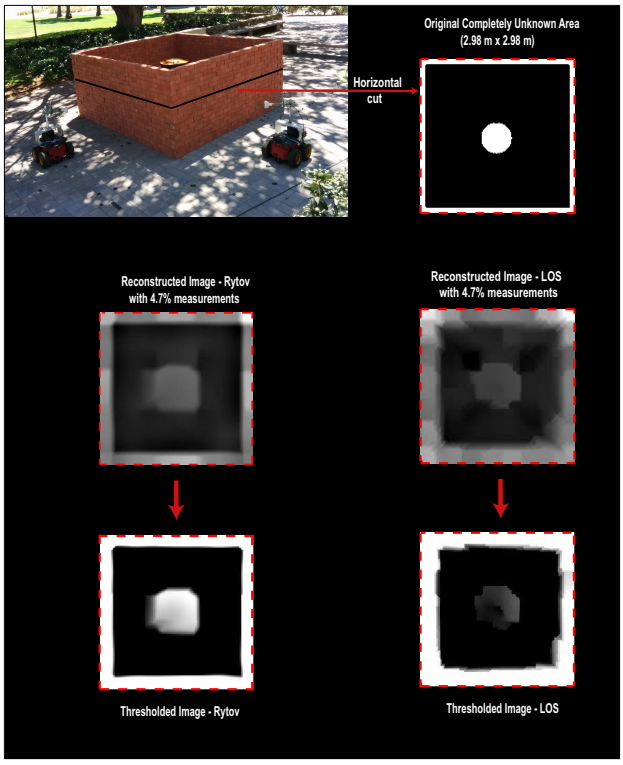

Figure 2.8: The left figures show the occluded cylinder structure of interest that is completely unknown and needs to be imaged, as well as its horizontal cut (its dimension is 2.98 m $\times$ 2.98 m). The white areas in the true image indicate that there is an object while the black areas denote that there is nothing in those spots. Imaging results based on 4.7% measurements are shown for both Rytov and LOS approaches. It can be seen that Rytov provides a considerably better imaging result.

seen from Fig. 2.9, the LOS approach fails to image this more complex structure while Rytov can image it. From Fig. 2.7 and 2.8, it can be seen that imaging based on LOS modeling can vaguely image the details. But for more complex areas such as Fig. 2.9, its performance becomes unacceptable while Rytov can locate the objects fairly accurately. This signifies the importance of properly modeling the receptions.

In general, the computational complexity of our imaging approach depends on the size of the unknown area and the number of gathered measurements. Furthermore, the utilized solver typically converges faster if the model better matches the real measurements. Hence, we expect that the Rytov approach runs faster than LOS approach because of

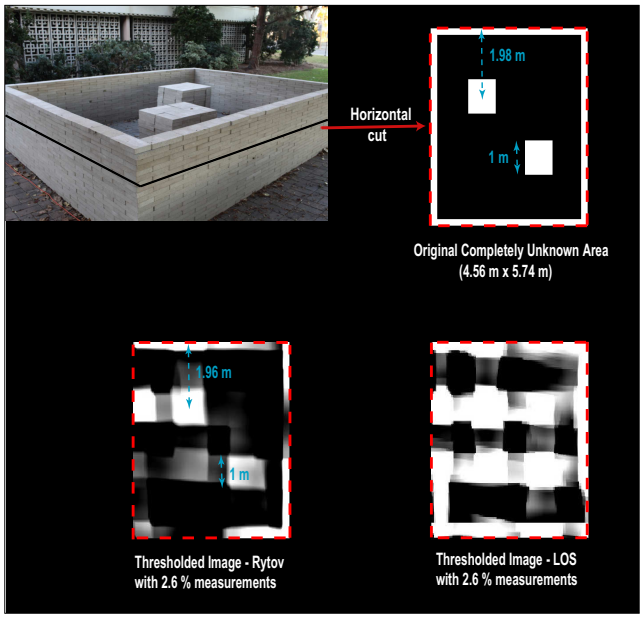

Figure 2.9: The top figures show the occluded two columns structure of interest that is completely unknown and needs to be imaged, as well as its horizontal cut (its dimension is 4.56 m $\times$ 5.74 m). The white areas in the true image indicate that there is an object while the black areas denote that there is nothing in those spots. Imaging results based on 2.6% measurements are shown in the bottom figures for both Rytov and LOS approaches. Sample dimensions are also shown. It can be seen that the LOS approach fails to properly image the occluded objects while Rytov performs significantly better.

its better match with the real measurement. We verify this on a desktop equipped with a 3.7 GHz CPU. For the T-shape with 4096 unknowns and 586 measurements, the Rytov approach takes 3.6 seconds, while the LOS approach takes 5.74 seconds. For the occluded cylinder with 22201 unknowns and 1036 measurements, the Rytov approach takes 17.01 seconds, while the LOS approach takes 27.14 seconds. For the occluded two columns inside with 65436 unknowns and 1699 measurements, the Rytov approach takes 54.8 seconds, while the LOS approach takes 64 seconds. However, it should be noted that Rytov also requires an offline calculation of the F_{R} matrix for a given set of routes. This takes 9 minutes for the occluded cylinder structure for example. Once this matrix is calculated, it can be used for any setup that uses the same routes.

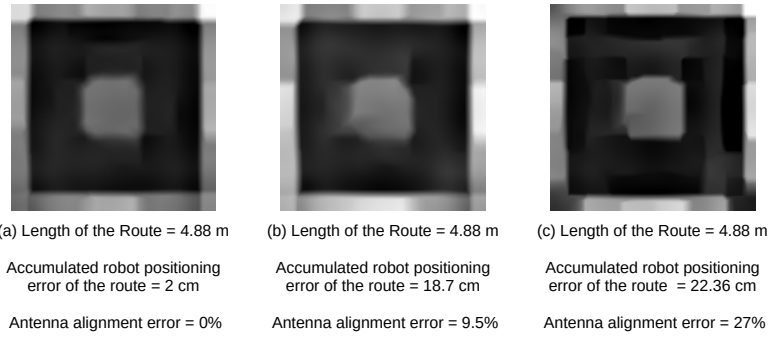

Figure 2.10: The figure shows the effect of robot positioning and antenna alignment errors on imaging based on Rytov approximation. It can be seen that they have negligible impact.

Finally, we note that the measurements of the T-shape were collected with our past experimental setup since we do not have access to this site anymore. However, we expect similar results with our new experimental setup for this site, for the reasons explained in Section 2.4.1.

2.4.1 Effect of robot positioning and antenna alignment errors

As each robot travels a route autonomously and without coordination with the other robot or positioning error correction, there will be non-negligible positioning and antenna alignment errors accumulated throughout the route. We next show the impact of these errors on our see-through imaging performance.

Fig. 2.10 and 2.11 show the impact of localization and antenna alignment errors on Rytov and LOS approaches respectively. More specifically, each figure compares experimental imaging results of three cases with different levels of localization/antenna alignment errors. The most accurate localization case was generated with our old setup where positioning errors were corrected every 1 m. The middle and right cases are both automated but the robot has different speeds, which results in different positioning

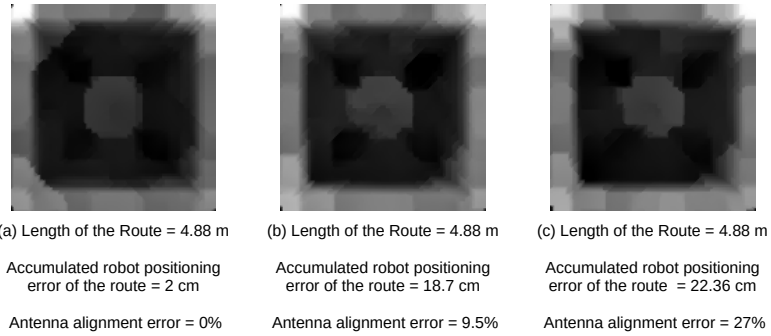

Figure 2.11: The figure shows the effect of robot positioning and antenna alignment errors on imaging based on LOS modeling. It can be seen that they have negligible impact.

accuracy. In each case, the positioning error leads to a non-negligible antenna alignment error, the value of which is reported (as a % of the antenna beamwidth). However, we can see that the combination of both antenna alignment and positioning errors, which are not negligible, has a negligible impact on the imaging result. This is due to the fact that the main current bottleneck in see-through imaging is the modeling of the receptions, which is our main motivation. For instance, as we showed in Fig. 2.6, the gap between the state of the art modeling (LOS) and the true receptions is huge, which we have reduced considerably by a proper modeling of the receptions. However, the gap is still non-negligible as compared to other sources of errors such as robot positioning and antenna alignment errors, as Fig. 2.10 and 2.11 confirm. It is needless to say that if these errors become more considerable, they will inevitably start impacting the results. Thus, Fig. 2.10 and 2.11 imply that with our current setup and the size of the areas we imaged, the impact of robot positioning and antenna alignment errors was negligible on our results.

Chapter 3

Occupancy Estimation

In this chapter, we show how to estimate the total number of people walking in an area based on only WiFi received signal strength measurements (e.g, RSSI) between a pair of stationary transmitter/receiver antennas. We first propose a framework based on understanding two important ways that people leave their signature on the transmitted signal: blocking the Line of Sight (LOS) and scattering effects. By developing a simple motion model, we first mathematically characterize the impact of the crowd on blocking the LOS. We next probabilistically characterize the impact of the total number of people on the scattering effects and the resulting multipath fading component. By putting the two components together, we then develop a mathematical expression for the probability distribution of the received signal amplitude as a function of the total number of occupants, which will be the base for our estimation using Kullback-Leibler divergence. In order to confirm our framework, we run extensive indoor and outdoor experiments with up to and including 9 people and show that the proposed framework can estimate the total number of people with a good accuracy with only a pair of WiFi cards and the corresponding RSSI measurements.

In the second part of this chapter, we focus on counting the total number of people walking inside a building (or in general behind walls), using readily-deployable WiFi transceivers that are installed outside the building, and only based on WiFi received

signal strength measurements (e.g., WiFi RSSI). Since the WiFi power measurements are severely attenuated due to walls, we propose a new methodology for crowd counting for through-wall scenarios. Furthermore, we focus on reducing the prior calibration required in the area of interest. We first observe that the inter-event times, corresponding to the dip events of the received signal, are fairly robust to the attenuation through walls (for instance as compared to the exact dip values). We then propose a methodology that can extract the total number of people from the inter-event times. More specifically, we first show how to characterize the wireless received power measurements as a superposition of renewal-type processes. By borrowing theories from the renewal-process literature, we then show how the probability mass function of the inter-event times carries vital information on the number of people. We validate our framework with 44 experiments in five different areas on our campus (3 classrooms, a conference room, and a hallway), using only one WiFi transmitter and receiver installed outside of the building, and for up to and including 20 people. Our experiments further include areas with different wall materials, such as concrete, plaster, and wood, to validate the robustness of the proposed approach. Overall, our results show that our approach can estimate the total number of people behind the walls with a high accuracy while minimizing the need for prior calibrations.

The rest of this chapter is organized as follows. In Section 3.1, we explain our problem formulation and develop our motion model. In Section 3.2.1, we characterize the probability of crossing the LOS. Multipath effects are then modeled in Section 3.2.2, where a final expression is developed by putting both blocking and multipath effects together. In Section 3.3, we present several indoor and outdoor experimental results confirming that our approach can estimate the total number of people with a good accuracy. In Section 3.4, we then propose our framework to estimate the total number of people by using properties of the inter-event times. In Section 3.5, we thoroughly validate our framework

using several experiments in five different areas on our campus.

3.1 Problem Formulation

Consider a scenario where N people are walking casually in an area as shown in Fig. 1.2. A WiFi transmitter (TX) and receiver (RX) are positioned (both stationary) at the border of this area to collect measurements, as marked in the figure. The goal of this dissertation is to estimate the total number of people based on only the received signal strength measurements over a small period of time. In this section, we present the mathematical formulation of our motion model. It should be noted that in our experiments, we have no control over how people walk and they are simply asked to walk casually. Thus, the purpose of this section is to derive a simple mathematical model for a casual walk.

3.1.1 Workspace Model

Consider a rectangular region of dimension $L \times B$, as shown in Fig. 3.1 (left). We discretize it to form a 2-D discrete workspace $\mathcal{W}$ consisting of cells, wherein the position of each cell is specified by the coordinates of its center. The origin is taken to be at the lower left corner. Moreover, the length and breadth are partitioned into $N_{\text{div},x}$ and $N_{\text{div},y}$ segments respectively. The dimension of a cell is thus $\Delta x \times \Delta y$, with $\Delta x = L/N_{\text{div},x}$ and $\Delta y = B/N_{\text{div},y}$. The workspace can then be summarized by $\mathcal{W} = \{(x, y)|x \in \mathcal{X}, y \in \mathcal{Y}\}$ where $\mathcal{X} = \{\frac{1}{2}\Delta x, \frac{3}{2}\Delta x, \cdots \frac{2N_{\text{div},x}-1}{2}\Delta x\}$ and $\mathcal{Y} = \{\frac{1}{2}\Delta y, \frac{3}{2}\Delta y, \cdots \frac{2N_{\text{div},y}-1}{2}\Delta y\}$.

A transmitter and receiver are located at the coordinates $(L/2, 0)$ and $(L/2, B)$ respectively. N people are moving in this workspace. In our mathematical modeling of this section, we discretize the position of each person to the center of a cell. This is solely for modeling purposes and people are not walking in a discretized manner in our

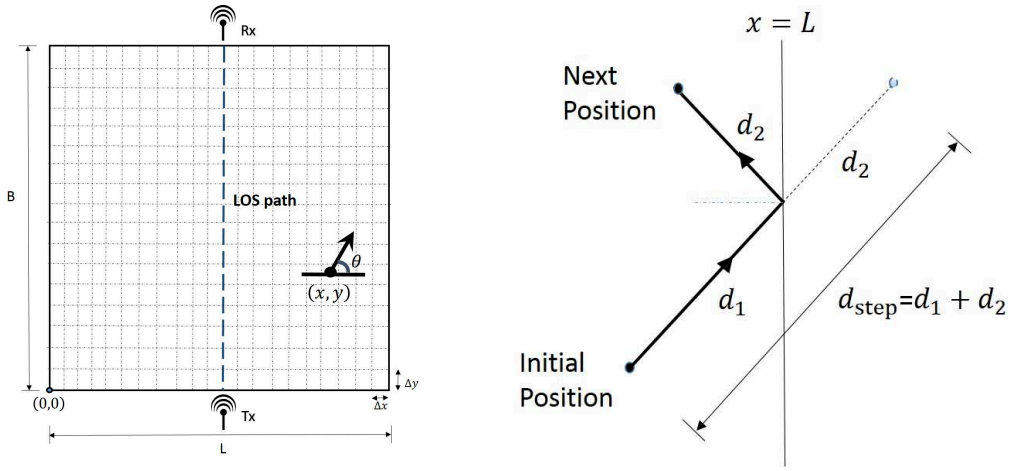

Figure 3.1: (left) An illustration of the workspace, (right) An illustration of the modeled boundary behaviour.

experimental setup.

3.1.2 Motion Model

In general, mathematical modeling of the motion of people is a challenging problem and not the focus of this dissertation. Instead, we are interested in a simple probabilistic motion model in order to characterize the stationary distribution of the position/heading of the people in the next section.

In our experiments, people were asked to walk casually. We observed that people had a tendency to maintain their direction for a while before changing it. In this section we come up with a simple mathematical model to characterize the movement of the people. For the sake of mathematical characterization, we assume that each person moves around the workspace independent of the others and at a speed of d_{step} per iteration.[1] At each iteration, we assume that a person chooses a direction θ (w.r.t the x axis as shown in Fig. 3.1 (left)) and moves a distance of d_{step} in that direction. If a step results in a person crossing the boundary, we assume that the person reflects off the boundary and lands

[1] An iteration refers to a time instant under the discretization of time.

back inside the workspace, as shown in Fig. 3.1 (right). Note that the total distance traveled is still d_{step}, as shown in Fig. 3.1 (right). At every iteration, the position of a person would be quantized to the center of the cell in which she currently resides.

We discretize the angle space $[0, 2\pi)$ into $\vartheta = \{0, \Delta\theta, \cdots, (N_{\text{div},\theta} - 1)\Delta\theta\}$ with $\Delta\theta = \frac{2\pi}{N_{\text{div},\theta}}$. At each iteration, we assume that each person maintains the same heading of the previous iteration, i.e. chooses the same θ, with the probability $p_\theta < 1$, and selects an angle uniformly from ϑ with the probability $1 - p_\theta$. The motion of person i can then be characterized by the following,

$$\theta_i(t+1) = \begin{cases} \theta_i(t) & \text{w.p. } p_\theta \\ \text{uniformly from } \vartheta & \text{w.p. } 1 - p_\theta \end{cases}, \tag{3.1}$$

$$x_i(t+1) = \begin{cases} -x_i(t) - \text{round}_x(d_{\text{step}} \cos\theta_i(t)) \\ \qquad \text{if } x_i(t) + \text{round}_x(d_{\text{step}} \cos\theta_i(t)) < 0 \\ 2L - x_i(t) - \text{round}_x(d_{\text{step}} \cos\theta_i(t)) \\ \qquad \text{if } x_i(t) + \text{round}_x(d_{\text{step}} \cos\theta_i(t)) > L \\ x_i(t) + \text{round}_x(d_{\text{step}} \cos\theta_i(t)) \\ \qquad \text{otherwise} \end{cases}, \tag{3.2}$$

$$y_i(t+1) = \begin{cases} -y_i(t) - \text{round}_y(d_{\text{step}} \sin\theta_i(t)) \\ \qquad \text{if } y_i(t) + \text{round}_y(d_{\text{step}} \sin\theta_i(t)) < 0 \\ 2B - y_i(t) - \text{round}_y(d_{\text{step}} \sin\theta_i(t)) \\ \qquad \text{if } y_i(t) + \text{round}_y(d_{\text{step}} \sin\theta_i(t)) > B \\ y_i(t) + \text{round}_y(d_{\text{step}} \sin\theta_i(t)) \\ \qquad \text{otherwise} \end{cases}, \tag{3.3}$$

where $\text{round}_x(d) = (\arg\min_{k\in\mathbb{Z}} |d - k\Delta x|)\Delta x$ and $\text{round}_y(d) = (\arg\min_{k\in\mathbb{Z}} |d - k\Delta y|)\Delta y$

are functions that round the input to the closest multiple of Δx and Δy respectively. Furthermore $x_i(t)$ and $y_i(t)$ denote the position of the i^{th} person at time t along the x and y axis respectively, and $\theta_i(t)$ represents the angle of person i at time t. Note that we excluded the case of $p_\theta = 1$ as it implies a purely deterministic motion model, which is not a good representation of a casual walk.

3.2 Estimation of the Total Number of People Based on WiFi Power Measurements

In this section, we discuss our proposed approach for estimating the total number of people based on only WiFi power measurements. A person will leave her signature on the received signal in two ways. First, when she crosses the LOS path between the TX and RX, she blocks the transmitted signal, resulting in a drop in the received signal power. Second, she acts as a scatterer of the signal, contributing to multipath fading (MP). As a result, we have two underlying effects: possible blockage of the LOS and multipath fading, both of which carry implicit information of N. Fig. 3.2 shows an example of a received signal power measurement (N=5 in this case). Sample arrows on the figure mark the impact of LOS blockage as well as MP. For a lower level of occupancy, the blocking effect typically results in more pronounced drops as compared to MP.

Our proposed approach is thus based on the understanding and characterization of the impact of N on these two phenomena.[2] We start by modeling the probability of blocking the LOS path in Section 3.2.1. This characterization is then utilized in Section 3.2.2, to mathematically model both effects and find an expression for the overall probability

[2]We note that there are several propagation phenomena when a transmission occurs. Our goal is not to model all these effects but rather have a simple yet comprehensive enough modeling for the purpose of estimating N.

density function (PDF) of the received signal amplitude as a function of N.

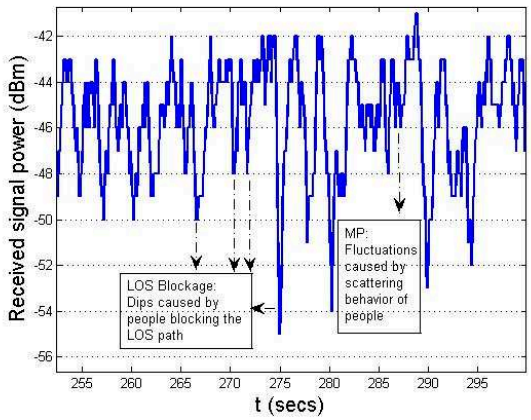

Figure 3.2: Sample received signal power for N=5, where a few examples of LOS blocking and MP effects are marked.

3.2.1 Characterization of the Probability of Blocking the LOS

In this section, we characterize the probability that k number of people cross the LOS in an iteration. We begin by finding the stationary probability distribution of the position and heading of a person. The main reason to characterize a stationary distribution is to make our framework as independent of the details of the motion as possible. We discuss this further in Remark 3.1. This, however, does not imply that we need to collect measurements for a very long period of time in practice. For instance, as we shall see in Section 3.3, we collect measurements for only 300 seconds, and our modeling provides a good approximation.

Asymptotic Distribution of the Position and Heading

In this part, we prove that the position and heading of a person takes a uniform distribution asymptotically.

Let $\Theta(t) \in \vartheta$ be a random variable denoting the heading of a person at time t. Equation (3.1) induces a Markov chain as follows:

$$\mu^{\Theta}(t+1) = P^{\Theta}\mu^{\Theta}(t), \tag{3.4}$$

where $\mu^{\Theta}(t)$ is a column vector with the i^{th} entry as $[\mu^{\Theta}(t)]_i = \Pr(\Theta(t) = (i-1)\Delta\theta)$ for $i \in \{1, 2, \cdots, N_{\text{div},\theta}\}$ and P^{Θ} is a matrix with the $(i,j)^{\text{th}}$ entry as $[P^{\Theta}]_{ij} = \Pr\Big(\Theta(t+1) = (i-1)\Delta\theta | \Theta(t) = (j-1)\Delta\theta\Big)$ for $i, j \in \{1, 2, \cdots, N_{\text{div},\theta}\}$.

Lemma 3.1 *Consider the heading dynamics of (3.1). Then the stationary distribution of $\Theta(t)$ is uniform.*

Proof: From the heading dynamics, we have the probability transition matrix as

$$P^{\Theta} = \begin{pmatrix} p_\theta + \frac{1-p_\theta}{N_{\text{div},\theta}} & \frac{1-p_\theta}{N_{\text{div},\theta}} & \cdots & \frac{1-p_\theta}{N_{\text{div},\theta}} \\ \frac{1-p_\theta}{N_{\text{div},\theta}} & p_\theta + \frac{1-p_\theta}{N_{\text{div},\theta}} & \cdots & \frac{1-p_\theta}{N_{\text{div},\theta}} \\ \vdots & \vdots & \ddots & \vdots \\ \frac{1-p_\theta}{N_{\text{div},\theta}} & \frac{1-p_\theta}{N_{\text{div},\theta}} & \cdots & p_\theta + \frac{1-p_\theta}{N_{\text{div},\theta}} \end{pmatrix}.^{3} \tag{3.5}$$

It can be seen that P^{Θ} is doubly stochastic. By applying the Geršgorin disk theorem [74], it can be easily seen that the spectral radius of P^{Θ} is 1. Since $p_\theta < 1$, we have $P^{\Theta} \succ 0$, i.e. P^{Θ} is positive. Then, by applying the Perron-Frobenius theorem [75], we have $\lim_{t\to\infty}(P^{\Theta})^t = \mathbf{1}_{N_{\text{div},\theta}} e_l^T$, where e_l is the left eigenvector of P^{Θ}, $\mathbf{1}_{N_{\text{div},\theta}}^T e_l = 1$ and $\mathbf{1}_r$ denotes a column vector of ones of size r. It can be easily confirmed that $e_l = \frac{1}{N_{\text{div},\theta}}\mathbf{1}_{N_{\text{div},\theta}}$, since P^{Θ} is doubly stochastic, resulting in $\lim_{t\to\infty}(P^{\Theta})^t = \frac{1}{N_{\text{div},\theta}}\mathbf{1}_{N_{\text{div},\theta}}\mathbf{1}_{N_{\text{div},\theta}}^T$ and

$$\mu^{\Theta} = \lim_{t\to\infty} \mu^{\Theta}(t) = \frac{1}{N_{\text{div},\theta}}\mathbf{1}_{N_{\text{div},\theta}}. \tag{3.6}$$

[3] An additional $\frac{1-p_\theta}{N_{\text{div},\theta}}$ term is present along the diagonal since a person may still select its previous angle when she selects uniformly from ϑ.

This means that the heading takes a uniform distribution asymptotically. ■

We next characterize the asymptotic distribution of the position. Let $X(t) \in \mathcal{X}$ be a random variable denoting the x axis coordinate of a person at time t. Equation (3.2) then induces the following Markov chain,

$$\mu^X(t+1) = P^X \mu^X(t), \tag{3.7}$$

where $\mu^X(t)$ is a column vector with the i^{th} entry $[\mu^X(t)]_i = \Pr(X(t) = \frac{2i-1}{2}\Delta x)$, for $i \in \{1, \cdots, N_{\text{div},x}\}$, and P^X is a matrix with the $(i,j)^{\text{th}}$ entry as $[P^X]_{ij} = \Pr\Big(X(t+1) = \frac{2i-1}{2}\Delta x | X(t) = \frac{2j-1}{2}\Delta x\Big)$ for $i, j \in \{1, \cdots, N_{\text{div},x}\}$.

Lemma 3.2 *Consider the motion dynamics of (3.1)-(3.3). Then, the stationary distribution of $X(t)$ is uniform.*

Proof: Let $\Theta = \lim_{t\to\infty} \Theta(t)$. Let $D_x = \text{round}_x(d_{\text{step}} \cos\Theta)$ be a random variable denoting the distance traveled by a person (rounded to a multiple of Δx) along the x axis when the probability distribution of $\Theta(t)$ has converged to its stationary distribution. The probability mass function (PMF) of D_x, p_{D_x}, is given as

$$\begin{aligned}
p_{D_x}(k\Delta x) &= \sum_{i\in\{1,\cdots,N_{\text{div},\theta}\}: d_{\text{step}}\cos(\frac{i-1}{N_{\text{div},\theta}}2\pi)\in[k\Delta x-\frac{\Delta x}{2}, k\Delta x+\frac{\Delta x}{2})} (\mu^\Theta)_i \\
&= \sum_{i\in\{1,\cdots,N_{\text{div},\theta}\}: d_{\text{step}}\cos(\frac{i-1}{N_{\text{div},\theta}}2\pi)\in[k\Delta x-\frac{\Delta x}{2}, k\Delta x+\frac{\Delta x}{2})} \frac{\Delta\theta}{2\pi} \\
&\approx 2\int_{\theta\in[0,\pi): d_{\text{step}}\cos\theta\in[k\Delta x-\frac{\Delta x}{2}, k\Delta x+\frac{\Delta x}{2})} \frac{1}{2\pi} d\theta \\
&= \int_{k\Delta x-\frac{\Delta x}{2}}^{k\Delta x+\frac{\Delta x}{2}} \frac{1}{\pi\sqrt{d_{\text{step}}^2 - r^2}} dr \\
&\approx \begin{cases} \frac{\Delta x}{\pi\sqrt{d_{\text{step}}^2-(k\Delta x)^2}}, & \text{if } k\in\mathbb{Z} \text{ and } |k\Delta x| < d_{\text{step}} \\ 0 & \text{else} \end{cases},
\end{aligned} \tag{3.8}$$

where the second equality follows since $[\mu^\Theta]_i = \frac{1}{N_{\text{div},\theta}} = \frac{\Delta\theta}{2\pi}$ for $i \in \{1, \cdots, N_{\text{div},\theta}\}$. Moreover, the fourth equality follows from the change of variable $r = d_{\text{step}} \cos\theta$.

The $(j,i)^{\text{th}}$ element of P^X can then be expressed as

$$
\begin{aligned}
[P^X]_{ji} &= \Pr\left(X(t+1) = \frac{2j-1}{2}\Delta x | X(t) = \frac{2i-1}{2}\Delta x\right) \\
&= \begin{cases}
p_{D_x}((j-i)\Delta x) + p_{D_x}((-j-i+1)\Delta x) \\
\qquad \text{if } j \in \{1, \cdots, \lfloor \frac{d_{\text{step}}}{\Delta x} \rfloor\} \\
p_{D_x}((j-i)\Delta x) + \\
\qquad p_{D_x}((2N_{\text{div},x}+1-j-i)\Delta x) \\
\qquad \text{if } j \in \{N_{\text{div},x} - \lfloor \frac{d_{\text{step}}}{\Delta x} \rfloor, \cdots, N_{\text{div},x}\} \\
p_{D_x}((j-i)\Delta x) \\
\qquad \text{else}
\end{cases} \\
&= [P^X]_{ij},
\end{aligned}
\tag{3.9}
$$

where the second terms in the first and second cases denote the probability of a transition from the i^{th} to the j^{th} cell via reflections off of the boundaries, and the last line follows since $p_{D_x}(i\Delta x) = p_{D_x}(-i\Delta x)$. It can be seen that P^X is thus doubly stochastic. Moreover, the graph induced by P^X is strongly connected and aperiodic. This implies that P^X is primitive [76]. Thus, similar to (3.6), we can apply the Perron-Frobenius theorem to deduce that

$$
\mu^X = \lim_{t\to\infty} \mu^X(t) = \frac{1}{N_{\text{div},x}} \mathbf{1}_{N_{\text{div},x}}. \tag{3.10}
$$

■

A similar analysis can be carried out for the probability of the position along the y-axis. Lemma 3.1 and 3.2 show that the position and heading of a person takes a uniform distribution asymptotically.

Remark 3.1 *While we derived the uniform asymptotic distribution for the angle model of (3.1), constant speed, and boundary behavior of Fig. 3.1 (right), we expect that an*

asymptotic stationary distribution will be achieved whenever there is a small amount of randomness in the motion model. A more rigorous characterization of this, however, is a subject of further studies.

Characterization of the Probability of Blocking

In this part, we derive a mathematical expression for the probability of blocking the LOS.

Definition 3.1 *We say a blocking (crossing)*[4] *has occurred at time* $t+1$ *if either* $x_i(t) \leq L/2$ *and* $x_i(t+1) \geq L/2$ *or* $x_i(t) \geq L/2$ *and* $x_i(t+1) \leq L/2$.

Based on the definition above, a cross has also occurred if a person lands exactly on the LOS path or moves along it. Thus, this probability of crossing considers slightly more cases than the case of only cutting the LOS, which is of interest to us. However, as we shall see, since we take $\Delta x \to 0$, the probability of these special cases tends to zero, resulting in the desired probability of crossing.

Theorem 3.1 *The asymptotic probability of a cross of a single person in an iteration can be characterized as*

$$p_{cross} = \frac{2d_{step}}{\pi L}. \tag{3.11}$$

Proof: A crossing occurs if a person who is sufficiently close to the LOS takes a large enough step to go over the LOS line. Based on Lemma 3.2, we can write the following

[4] *We use the terms crossing and blocking interchangeably since a non-zero speed is assumed.*

expression for the probability of a cross of one person (in one time step):

$$\begin{aligned}
p_{\text{cross}} &= 2 \sum_{i=\lfloor \frac{L}{2\Delta x}+\frac{1}{2} \rfloor - \lfloor \frac{d_{\text{step}}}{\Delta x} \rfloor}^{\lfloor \frac{L}{2\Delta x}+\frac{1}{2} \rfloor} [\mu^X]_i \sum_{k=\lceil \frac{L}{2\Delta x}+\frac{1}{2} \rceil - i}^{\lfloor \frac{d_{\text{step}}}{\Delta x} \rfloor} p_{D_X}(k\Delta x) \\
&= 2 \sum_{i=\lfloor \frac{L}{2\Delta x}+\frac{1}{2} \rfloor - \lfloor \frac{d_{\text{step}}}{\Delta x} \rfloor}^{\lfloor \frac{L}{2\Delta x}+\frac{1}{2} \rfloor} \frac{\Delta x}{L} \\
&\qquad \sum_{k=\lceil \frac{L}{2\Delta x}+\frac{1}{2} \rceil - i}^{\lfloor \frac{d_{\text{step}}}{\Delta x} \rfloor} \frac{\Delta x}{\pi \sqrt{d_{\text{step}}^2 - (k\Delta x)^2}} \\
&\approx 2 \int_{L/2-d_{\text{step}}}^{L/2} \int_{L/2-x}^{d_{\text{step}}} \frac{1}{L} \frac{1}{\pi \sqrt{d_{\text{step}}^2 - (r)^2}} dx dr \\
&= 2 \int_0^{d_{\text{step}}} \frac{1}{L} \int_{x/d_{\text{step}}}^1 \frac{1}{\pi \sqrt{1-r^2}} dx dr \\
&= \frac{2 d_{\text{step}}}{\pi L},
\end{aligned} \tag{3.12}$$

where the second equality follows since $[\mu^X]_i = \frac{1}{N_{\text{div},x}} = \frac{\Delta x}{L}$, for $i \in \{1, \cdots, N_{\text{div},x}\}$. ■

Note that p_{cross} is a linear function of d_{step}, as expected. Since there are N people in the workspace, we can have simultaneous crosses.

Corollary 3.1 *Let $p_{K,N}$ denote the PMF of random variable K denoting the number of simultaneous crosses with N people in the workspace. Assuming independent motion models for the people then results in the following expression*

$$\begin{aligned}
p_{K,N}(k) &= Pr(k \text{ simultaneous cross}) \\
&= \binom{N}{k} p_{cross}^k (1 - p_{cross})^{N-k},
\end{aligned} \tag{3.13}$$

where p_{cross} is as defined in Theorem 3.1.

Remark 3.2 *Although, our derivation of p_{cross} is under the assumption of a constant*

speed d_{step}, our result can be extended to the case of a person moving with a variable random speed. Due to p_{cross} being linear in d_{step}, the probability of a cross would then become $p_{cross} = \frac{2\overline{d_{step}}}{\pi L}$, where $\overline{d_{step}}$ denotes the average speed of the person.

3.2.2 Derivation of the PDF of the received signal

In this section, we consider both blocking and MP effects and find an expression for the PDF of the received signal strength as a function of N.

Consider N people walking in the area of interest with a constant speed. As we discussed earlier, each person impacts the received signal by 1) blocking when she crosses the LOS and 2) scattering. Furthermore, there may be several other objects in the area impacting the received signal. We assume that these objects are stationary in our modeling.[5] The baseband equivalent received signal is then given by

$$\begin{aligned} A &= \underbrace{b_0 e^{j\psi_0}}_{\text{LOS}} + \underbrace{\sum_{j=1}^{M} b_j e^{j\psi_j}}_{\text{MP due to static objects}} + \underbrace{\sum_{i=1}^{N} a_i e^{j\phi_i}}_{\text{MP due to walking people}}, \\ &= a_0 e^{j\phi_0} + \sum_{i=1}^{N} a_i e^{j\phi_i} \\ &= A_{\text{LOS,ST}} + A_{\text{MP}}, \end{aligned} \tag{3.14}$$

where b_0 and ψ_0 are the amplitude and phase of the LOS path respectively, a_i and ϕ_i are the amplitude and phase of the path resulting from scattering off of the i^{th} person respectively, and b_j and ψ_j, for $j \neq 0$, are the amplitude and phase of the path resulting from scattering off of the j^{th} static object respectively. Then $\sum_{j=1}^{M} b_j e^{j\psi_j}$ denotes the impact of other static objects on the received signal, with M representing the total number of such static objects. Let $A_{\text{LOS,ST}} \triangleq b_0 e^{j\psi_0} + \sum_{j=1}^{M} b_j e^{j\psi_j} = a_0 e^{j\phi_0}$ denote the

[5] During the experiment, other surrounding objects such as leaves may move. However, the impact of their motion is typically negligible as compared to other effects.

summation of the LOS component and the MP due to the static objects. Furthermore, let $A_{\text{MP}} \triangleq \sum_{i=1}^{N} a_i e^{j\phi_i}$ represent the MP component due to people walking. The phase of each path, ϕ_i, for $i = 1, 2...N$, and ψ_j, for $j = 0, 1, 2...M$, is assumed to be uniformly distributed in $[0\ 2\pi]$.[6] ϕ_i is assumed independent of a_i and ϕ_j, and a_i is taken independent of a_j, for $j \neq i$ [78]. Note that the Doppler shifts due to the scatterer motion is small and thus not considered in this dissertation.

We are interested in deriving the PDF of the received signal amplitude $|A|$. Since $A_{\text{LOS,ST}}$ and A_{MP} are independent, we have [77]

$$C_A(U) = C_{A_{\text{LOS,ST}}}(U) C_{A_{\text{MP}}}(U),$$

where $C_{A_{\text{LOS,ST}}}(U)$, $C_{A_{\text{MP}}}(U)$ are the characteristic functions of $A_{\text{LOS,ST}}$ and A_{MP} respectively, and U is the corresponding variable of the characteristic functions.

[6] This assumption is justifiable since we operate at a high frequency [77].

$C_{A_{\mathrm{MP}}}(U)$ can be characterized as follows:

$$\begin{aligned}
C_{A_{\mathrm{MP}}}(U) &= \mathrm{E}_{A_{\mathrm{MP}}}(e^{jU\bullet A_{\mathrm{MP}}}) \\
&= \mathrm{E}_{A_{\mathrm{MP}}}(e^{jU\bullet(\sum_{i=1}^{N} a_i e^{j\phi_i})}) \\
&= \mathrm{E}_{A_{\mathrm{MP}}}(\prod_{i=1}^{N} e^{jU\bullet(a_i e^{j\phi_i})}) \\
&= \prod_{i=1}^{N} \mathrm{E}_{a_i,\phi_i}(e^{jU\bullet(a_i e^{j\phi_i})}) \\
&\qquad \text{(since } a_i, \phi_i \text{ independent of } a_j, \phi_j) \\
&= \prod_{i=1}^{N} \mathrm{E}_{a_i,\phi_i}(e^{j|U|a_i cos(\phi_i - \angle(u))}) \\
&= \prod_{i=1}^{N} \mathrm{E}_{a_i}(J_0(a_i|U|)),
\end{aligned} \tag{3.15}$$

where J_0 is the zeroth-order Bessel function of the first kind, $\mathrm{E}_a(.)$ represents the expectation w.r.t a, and $\bullet$ represents the dot product. Similarly, the characteristic function of $A_{\mathrm{LOS,ST}}$ is given by

$$C_{A_{\mathrm{LOS,ST}}}(U) = \mathrm{E}_{a_0}(J_0(a_0|U|)). \tag{3.16}$$

Note that the characteristic functions depend only on the magnitude of U and therefore

are circular symmetric [78]. The PDF of A is then given as

$$\begin{aligned} p_A(Z) &= \frac{1}{4\pi^2}\int_{|U|=0}^{\infty}\int_{\angle U=0}^{2\pi} e^{-jU\bullet Z} C_A(U)|U|d|U|d\angle U \\ &= \frac{1}{4\pi^2}\int_{|U|=0}^{\infty}\int_{\angle U=0}^{2\pi} e^{-j|U||Z|\cos(\angle U-\angle Z)} C_A(U)|U|d|U|d\angle U \\ &= \frac{1}{4\pi^2}\int_{|U|=0}^{\infty}|U|\Big(\int_{\angle U=0}^{2\pi} e^{-j|U||Z|\cos(\angle U-\angle Z)} d\angle U\Big) \\ &\qquad\qquad C_A(U)d|U| \\ &= \frac{1}{2\pi}\int_{|U|=0}^{\infty}|U|J_0(|U||Z|)C_A(U)d|U| \\ &= \frac{1}{2\pi}\int_{|U|=0}^{\infty}|U|J_0(|U||Z|)\Big(\prod_{i=1}^{N}\mathrm{E}_{a_i}(J_0(a_i|U|))\Big) \\ &\qquad\qquad \mathrm{E}_{a_0}(J_0(a_0|U|))d|U|. \end{aligned} \tag{3.17}$$

Then, the PDF of $|A|$ can be found as

$$\begin{aligned} p_{|A|}(z) &= \int_{\angle A=0}^{2\pi} z p_A(A) d\angle A \\ &= z\int_{|U|=0}^{\infty}|U|J_0(|U|z)\Big(\prod_{i=1}^{N}\mathrm{E}_{a_i}(J_0(a_i|U|))\Big) \\ &\qquad\qquad \mathrm{E}_{a_0}(J_0(a_0|U|))d|U|. \end{aligned} \tag{3.18}$$

Random variable a_0 can only take discrete values corresponding to the received signal strength when different number of people are along the LOS path. Thus by using Theorem 3.1, we have the following for the PDF of a_0 [7]

$$p_{a_0} = \sum_{k=0}^{N}\binom{N}{k} p_{\text{cross}}^{k}(1-p_{\text{cross}})^{N-k}\delta(a_0 - B_k), \tag{3.19}$$

where B_k is the received signal amplitude when k people are along the LOS path,[8] and

[7] Note that this is the PDF of the received signal amplitude when there is no MP component due to people walking, i.e. only the LOS component and MP due to static objects are present.

[8] Note that impact of static objects is inherently included in B_k.

$\delta(.)$ is the Dirac delta function. Using (3.19), we get

$$\mathrm{E}_{a_0}(J_0(a_0|U|)) = \sum_{k=0}^{N} \binom{N}{k} p_{\mathrm{cross}}^{k}(1-p_{\mathrm{cross}})^{N-k} J_0(|U|B_k). \tag{3.20}$$

In order to evaluate the characteristic function of A_{MP}, we need to characterize the PDF of a_i for $i \neq 0$, i.e. the amplitude of each component of MP due to people walking. Since a_i for $i \neq 0$ is the amplitude of the scattered signal from only one scatterer (one person), Rayleigh statistics cannot be used [78]. In a different context, a K-distribution is widely used to model the sea clutter and echo signal from biological tissues when the number of scatterers are low [78], [79], [80]. We thus use K-distribution to model the PDF of a_i for $i \neq 0$ as follows [78],

$$p_{a_i} = \frac{2b}{\Gamma(1+\nu)}\Big(\frac{ba}{2}\Big)^{\nu+1} K_\nu(ba) \quad \nu > -1, i \neq 0 \tag{3.21}$$

where $K_\nu(.)$ is the modified Bessel function of the second kind, and b and ν are the parameters of the distribution. Since the scatterers are taken to have identical statistics, we get

$$\prod_{i=1}^{N} \mathrm{E}_{a_i}(J_0(a_i|U|)) = (\mathrm{E}_{a_i}(J_0(a_i|U|)))^N. \tag{3.22}$$

Therefore the PDF of $|A|$ is given by

$$\begin{aligned} p_{|A|,N}(z) &= z\int_{|U|=0}^{\infty} |U| J_0(|U|z)(\mathrm{E}_{a_i}(J_0(a_i|U|)))^N \mathrm{E}_{a_0}(J_0(a_0|U|))d|U| \\ &= z\int_{|U|=0}^{\infty} |U| J_0(|U|z) f(N) d|U|, \end{aligned} \tag{3.23}$$

where we added the subscript N to emphasize the dependency on N, and

$$f(N) = (\mathrm{E}_{a_i}(J_0(a_i|U|)))^N \mathrm{E}_{a_0}(J_0(a_0|U|)). \tag{3.24}$$

3.3 Experimental Results

In this section, we show that our proposed framework can estimate the number of people well in several different cases in both indoor and outdoor environments. We start by briefly summarizing our experimental setup.

We use an 802.11g card for both the transmitter and the receiver. More specifically, the transmitter uses D-Link WBR-1310 wireless router [81], broadcasting a wireless signal. The receiver then constantly measures its receptions. In our setup, the transmitter and receiver are stationary and mounted on two Pioneer 3-AT mobile robots from MobileRobots Inc. [70], as shown in Fig. 3.3. It should be noted that any other object could have been used to hold the TX/RX (since the TX and RX are not moving). However, the automation through the use of robots hold promises for the future extensions of this work. The overall operation is then overseen by a remote PC, which is in charge of communicating the execution plan and collecting the final received signal strength (RSS) readings at the end of the operation.

We run two different sets of experiments in both outdoor and indoor environments. In the first set of experiments, we use directional antennas for both the transmitter and the receiver. We then show that in this case, modeling the received signal with only $A_{\mathrm{LOS,ST}}$ of (3.14) suffices for the estimation of the number of people. In the second case, we use omnidirectional antennas at both the transmitter and the receiver. We then show that a good estimation of the total number of people can be achieved by using our proposed modeling of (3.23).

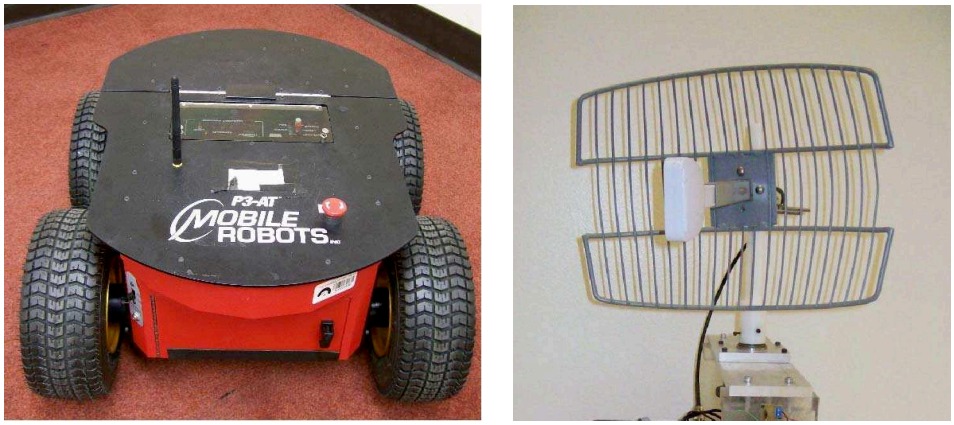

Figure 3.3: (left) Pioneer 3-AT Robot with an omnidirectional antenna, (right) GD24-15 2.4 GHz parabolic grid directional antenna.

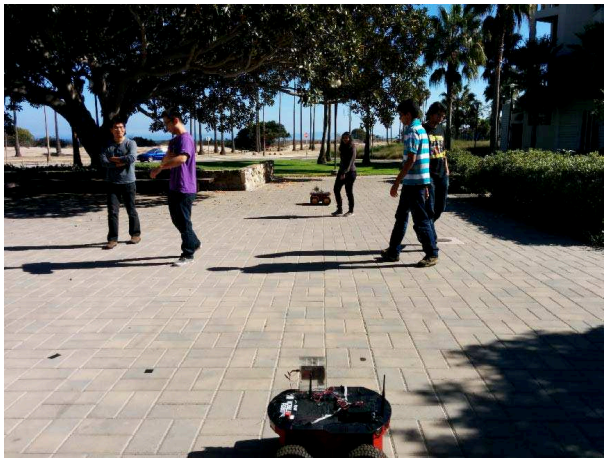

Figure 3.4: Outdoor Site

Fig. 3.4 shows the outdoor site, which has the dimensions $L = 7$ m and $B = 10$ m. Fig. 3.5 then shows the indoor site with the dimensions $L = 4.4$ m and $B = 7.5$ m. These dimensions are assumed to be known to the estimator. Experiments are carried out with 1, 3, 5, 7 and 9 people. People are told to walk casually in the area and bounce of the boundary when they approach it. The data is collected for 300 seconds, at the rate of 50 samples/s. A constant velocity of 1 m/s is assumed for the estimation process. Note that this is only for the purpose of mathematical modeling and estimation, and that we have no control over the speed of the people when they walk.

Figure 3.5: Indoor site

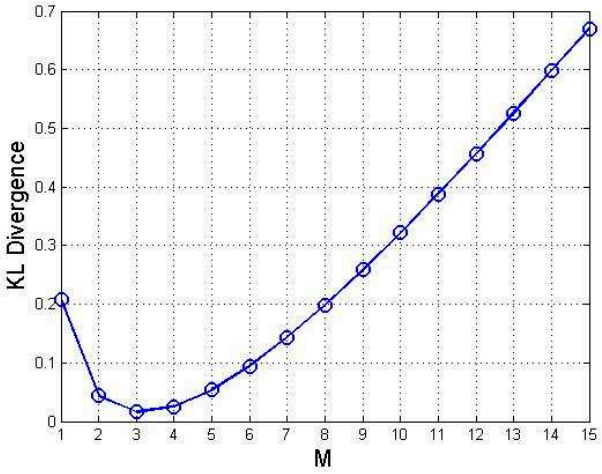

Figure 3.6: KL divergence $D_{\mathrm{KL}}(p_{K,\mathrm{exp}}||p_{K,M})$ between the theoretical and experimental PMF of simultaneous crosses, as a function of M, for the case of $N = 3$ (with directional antennas) in the outdoor site. It can be seen that the curve is minimized at $N_{\mathrm{est}} = 3$, resulting in an accurate estimation of the total number of people.

The environment of interest has other objects that will interact with the transmitted signal,[9] as discussed in (3.14), and their impact is modeled in $A_{\mathrm{LOS,ST}}$. As can be seen from (3.23), prior estimation of B_ks is needed for our approach. In order to acquire this, prior measurements are made when k number of people are walking on the straight line

[9]We assume that these objects are not moving. However, when we carry out our experiments, movements of vehicles and leaves (in the outdoor environment) were naturally inevitable.

connecting the transmitter and the receiver (in order to average the attenuation over several possible combinations). We should note that in practice this approach is scalable for the following reason. As the number of people increases, the value of B_k starts to saturate. Thus, we only need to collect prior measurements in order to estimate B_k for the lower values of k. In addition, dynamical system models can also be utilized to further fine tune the estimation of B_k at the higher values of k. Let $\widehat{B_k}$ represent the prior estimation of B_k in the rest of this section. As for the MP part (A_{MP} in (3.14)), we further need a prior estimation of b and ν. We measure these parameters a priori by having one person move in the area without crossing the LOS path. Then, the PDF of the collected measurements is matched to the convolution of the K-distribution of (3.21) and the PDF of the LOS path when no people are around, in order to find the best fit of b and ν.

3.3.1 Estimation of the Number of People in Outdoor Environments

In this section, we show our results in outdoor environments with both directional and omnidirectional antennas.

Estimation with Directional Antennas

In this part, directional antennas are used at both the transmitter and the receiver. More specifically, we use GD24-15 2.4 GHz parabolic grid antennas from Laird Technologies, as shown in Fig. 3.3. This model has a 15 dBi gain with 21 degree horizontal and 17 degree vertical beamwidth and is suitable for IEEE 802.11 b/g applications [71]. This is an important case to study as it brings an understanding to the blocking characterization of Section 3.2.1 (first term in the second equation of (3.14)). More specifically, we see

that, in this case, the impact of the crowd on the transmitted signal is mainly captured through the first term in (3.14), i.e. people impact the signal when they cross the LOS, and the multipath effect, due to scattering off of people, is negligible.

From (3.13), we have $p_{K,N}$, the theoretical PMF for the number of simultaneous crosses per time, as a function of N. Since we are not considering the impact of MP due to people walking in this case, this equation will be the base for our estimation of N. Let $p_{K,\text{exp}}$ denote this estimated PMF. We then find $N_{\text{est,dir}}$ such that it minimizes the Kullback-Leibler (KL) divergence between the experimental and theoretical PMFs:

$$N_{\text{est,dir}} = \arg\min_{M} D_{\text{KL}}(p_{K,\text{exp}}||p_{K,M}), \tag{3.25}$$

where $D_{\text{KL}}(p_1||p_2)$ is the KL divergence [82] between the two distributions p_1 and p_2. Fig. 3.6 further shows the corresponding KL divergence curve as a function of M for a sample case for $N = 3$ in the outdoor environment. It can be seen that the curve is minimized at $N = 3$, resulting in the accurate estimation of N in this case.

Table 3.1 shows the performance of our approach for different number of people, for a sample case in the outdoor environment. It can be seen that our approach can estimate the number of people considerably well in this case. To see the variability of the results in different runs, we further run 5 experiments on 5 different days for each number of occupants indicated in the first row of Table 3.1. Fig. 3.7 (left) shows the resulting Cumulative Distribution Function (CDF) of the estimation error of all the cases (5 runs) in terms of the number of people for the outdoor case and with directional antennas. It can be seen that, the estimation error is 0 or 1 person 92% of the time and 2 or less 100% of the time.

So far, we have presented our results based on the collected measurements of 300

Number of People in the Area	1	3	5	7	9
Estimated Number of People	1	3	4	7	8

Table 3.1: Sample performance of our approach for the case of directional antennas in the outdoor environment.

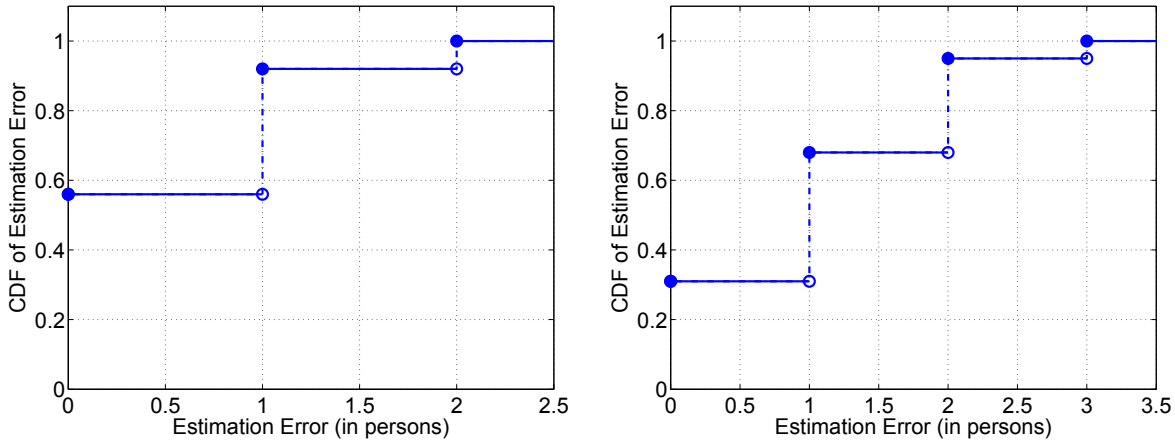

Figure 3.7: The CDF of the estimation error for the case of (left) directional TX/RX and (right) omnidirectional TX/RX antennas in the outdoor environment, based on several experiments with up to and including 9 people. It can be seen that we can estimate the total number of people with a good accuracy.

seconds. In order to see the impact of the measurement time on the estimation error, Fig. 3.8 (left) further shows occupancy estimation, as a function of time, for three sample experiments in the outdoor environment. It can be seen that the estimation converges to within an error of 1 of its final value after 100 seconds for these sample cases. This suggests that a shorter time duration could have also resulted in a similar performance in these cases. In general, the time duration should be chosen such that the experiment has reached its steady state. An upper bound for this time duration can be obtained based on the size of the area, the assumed walking speed, and an upper bound on the expected number of people.

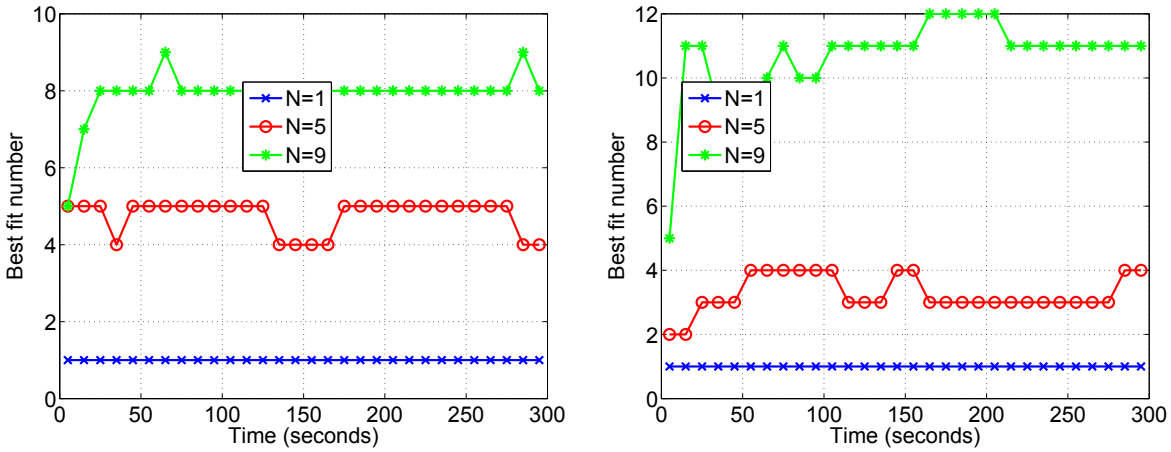

Figure 3.8: Sample occupancy estimations, as a function of time, for the case of (left) directional TX/RX and (right) omnidirectional TX/RX antennas in the outdoor environment. It can be seen that the estimation converges to within 1 person of its final value in 100 seconds.

Estimation with Omnidirectional Antennas

In this scenario, omnidirectional antennas are used at both the transmitter and the receiver. Thus, both LOS and MP components need to be considered, which makes the estimation process more challenging. The PDF of the received signal amplitude is as derived in (3.23), which is an implicit function of N. Let p_{exp} represent the PDF of the measured received signal amplitude. Then, we estimate the total number of people through the following KL divergence minimization:

$$N_{\text{est,omni}} = \arg\min_{M} D_{\text{KL}}(p_{\text{exp}}||p_{|A|,M}). \tag{3.26}$$

Table 3.2 shows the performance of our approach for different number of people for a sample case in the outdoor environment. It can be seen that the estimation performance is considerably good for this sample case. To see the variability of the results in different runs, we further run 5 experiments on 5 different days for each number of occupants indicated in the first row of Table 3.2. Fig. 3.7 (right) shows the resulting Cumulative

Number of people in the Area	1	3	5	7	9
Estimated Number of People	1	3	4	7	8

Table 3.2: Sample performance of our approach for the case of omnidirectional antennas in the outdoor environment.

Distribution Function (CDF) of the estimation error of all the cases (5 runs) in terms of the number of people.

It can be seen that the estimation error is 2 or less 96% of the time, which is a good accuracy. As expected, probability of error is higher as compared to Fig. 3.7 (left) where directional antennas were used. Fig. 3.8 (right) shows occupancy estimation, as a function of time, for sample experiments with omnidirectional antennas. It can be seen that the estimation converges to within an error of 1 of its final value after 100 seconds for these cases as well. Finally, Fig. 3.9 compares the corresponding experimental and theoretical PDFs for sample cases with different number of people. Each plot shows the amplitude PDF of the experimental data and the best fit theoretical PDF obtained by minimizing the KL divergence. The resulting N is then shown as $N_{\text{est,omni}}$. It can be seen that the experimental and theoretical pdfs are matching well.

3.3.2 Estimation of the Number of People in Indoor Environments

In this section, we show our results for estimating the level of occupancy in indoor. The site details are shown in Fig. 3.5 and summarized earlier in Section 3.3. The rest of the experimental setup is the same as for the outdoor case. As expected, the indoor environment will experience more multipath effect due to static objects. Our results indicate that we can still estimate the total number of people with a good accuracy.

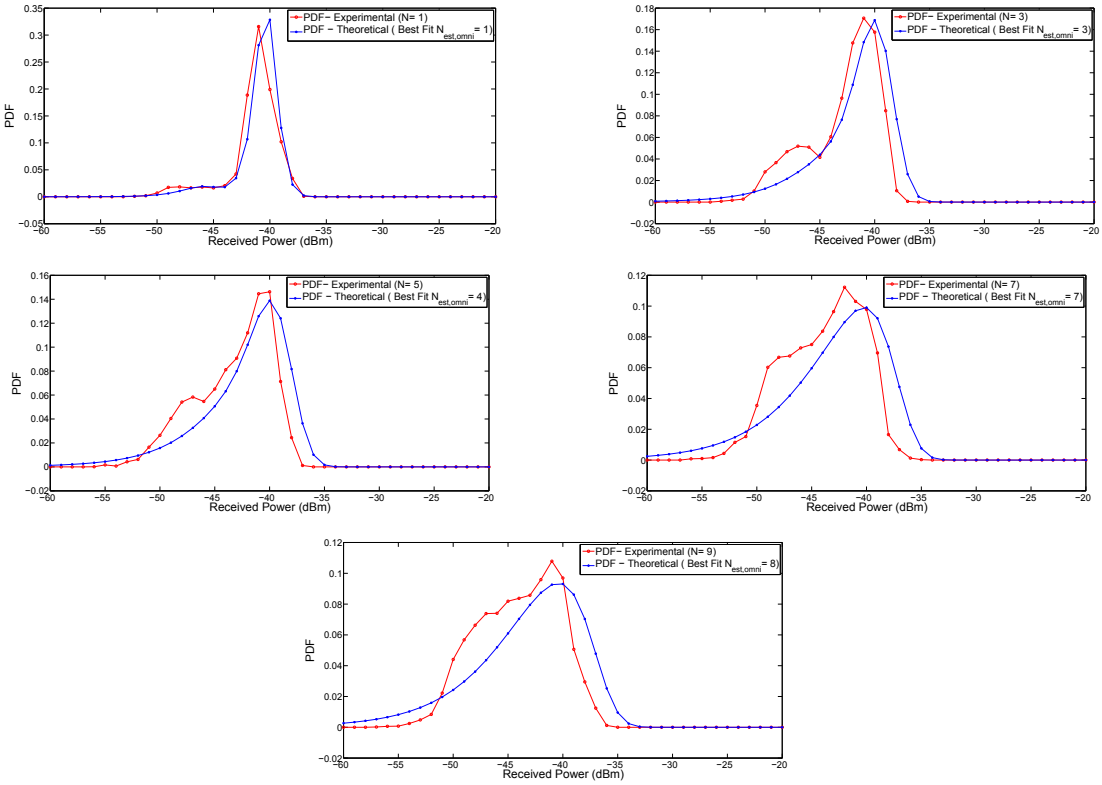

Figure 3.9: A Comparison of the theoretical PDF of (3.23) and the experimental PDF for different cases (with omnidirectional antennas) in the outdoor environment.

Number of People in the Area	1	3	5	7	9
Estimated Number of People	1	3	4	6	7

Table 3.3: Sample performance of our approach for the case of directional antennas in the indoor environment.

Estimation with Directional Antennas

Table 3.3 shows the performance of our approach for different number of people for a sample case in the indoor site when directional antennas are used. In this case, (3.19) suffices to estimate the number of people, as discussed earlier. It can be seen that our approach can estimate the level of occupancy well in an indoor setting. To see the variability of the results in different runs, we further run 7 experiments on 7 different days for each number of occupants indicated in the first row of Table 3.3. Fig. 3.10 (left) then shows the resulting Cumulative Distribution Function (CDF) of the estimation error of all the cases (7 runs) in terms of the number of people for the indoor site. It can be seen that the estimation error is 0 or 1 88% of the time and 2 or less 100% of time, showing a good performance.

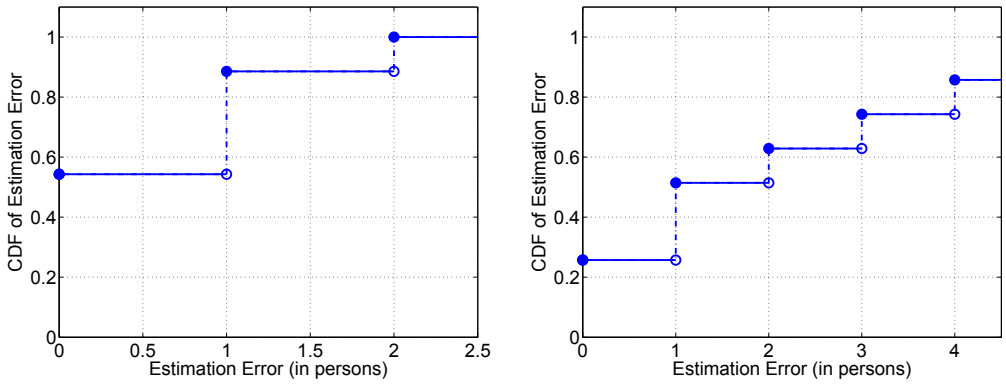

Figure 3.10: The CDF of the estimation error for the case of (left)directional TX/RX and (right) omnidirectional TX/RX antennas in the indoor environment, based on several experiments with up to and including 9 people. It can be seen that we can estimate the total number of people with a good accuracy.

Number of people in the Area	1	3	5	7	9
Estimated Number of People	2	3	8	10	11

Table 3.4: Sample performance of our approach for the case of omnidirectional antennas in the indoor environment.

Estimation with Omnidirectional Antennas

Next, we test our proposed approach with omnidirectional antennas in the indoor site of Section 3.2.2). Table 3.4 shows the performance of our approach for different number of people for a sample case. It can be seen that our approach can also estimate the level of occupancy well in an indoor setting with omnidirectional antennas. To see the variability of the results in different runs, we further run 7 experiments on 7 different days for each number of occupants indicated in the first row of Table 3.4. Fig. 3.10 (right) then shows the resulting Cumulative Distribution Function (CDF) of the estimation error of all the cases (7 runs) in terms of the number of people. It can be seen that the estimation error is 2 or less 63% of time, confirming a successful indoor performance with typical omnidirectional antennas that come as part of the 802.11 WLAN cards.

3.4 Crowd Counting Through Walls

So far, we established a framework to estimate the occupancy in an area where wireless sensors are present. In this section, we consider a more general scenario of occupany estimation where the wireless sensors are not necessarily in the same area. Consider an area that is enclosed by walls, such as a room, where N people are walking. Fig. 3.11 shows an example of this. Our goal is then to estimate the number of people walking in this area, using only RSSI measurements of WiFi nodes that are located outside of the area. As wireless signals can pass through the walls, we can in principle utilize our framework derived in the previous section for crowd counting in the through-wall

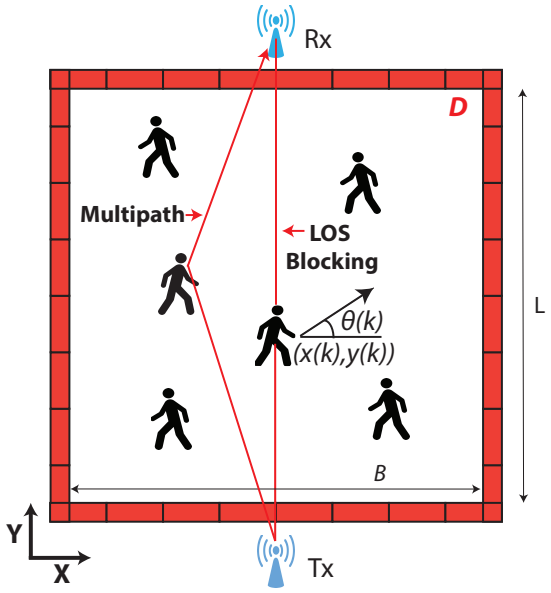

Figure 3.11: An illustration of the workspace with people walking inside. The red outer boundary denotes the walls. The WiFi Tx and Rx are located behind the walls and collect wireless measurements as people walk in the region. The goal in this section is then to estimate the number of people in the workspace using only the wireless measurements.

scenario. However, when the attenuation due to walls become severe, the wireless power measurements will be close to the noise floor of the receiver when people are blocking the LOS link. For instance, a 20 cm concrete wall can attenuate the signal by 40 dB. Therefore, our previous framework will have higher error in counting the number of people in this scenario. Furthermore, as we may not have access to the area of interest before hand, the focus in this section is to estimate the occupancy with minimal prior calibration. In this section, we propose a new framework to estimate the number of people walking inside an occluded area using only the RSSI of WiFi nodes located outside of the area. Specifically, we first model the motion of a single person as a discrete-time random process. We then utilize theories from the Renewal process literature to characterize the impact of multiple people and identify the statistics that can be used to estimate the number of people. As we shall see, the inter-event times of the resulting process carry vital information on the number of people, as we shall mathematically characterize.

3.4.1 Motion of a Single Person as a Renewal-type Process

Consider a scenario where N people are walking in the workspace D, as shown in Fig. 3.11. Without loss of generality, assume that the transmitter and the receiver are at the midpoint of the corresponding walls. The time intervals between successive crosses (i.e., LOS crossings) implicitly carry vital information about the total number of people walking in the area, as we show in the next section. In this section, we first mathematically characterize the statistics of the time intervals between successive crosses, when a single person is walking in D. We then utilize the results derived here to model the impact of N on the statistics of the cross times in the next section, when N people are walking in D.

Consider a single person walking in the workspace D. Let $\mathcal{E}$ denote an event of the person crossing the LOS link. Due to the non-deterministic nature of the walk, the times at which event $\mathcal{E}$ happens are random in nature. Let $X_1, X_2, \ldots, X_T$ denote a sequence of random variables such that,

$$X_i = \begin{cases} 1 & \text{if } \mathcal{E} \text{ happens at time instant i} \\ 0 & \text{otherwise.} \end{cases} \tag{3.27}$$

Let $S_1, S_2, \ldots, S_{n+1}$ denote the times at which event $\mathcal{E}$ occurs and let $T_1, T_2, \ldots, T_n$ denote the inter-event times. We have discretized the time to a step size of δt. Thus, S_i, for $1 \leq i \leq n+1$, and T_i, for $1 \leq i \leq n$, are non-negative integers.

Fig. 3.12 shows a sample realization of the process along with the sample occurrence times and the inter-event times. Under the casual motion model, the positions/headings will have a uniform distribution asymptotically in theory and after a sufficient time in practice [55]. We thus assume that the positions/headings have no spatial bias in our derivations. Then, we have,

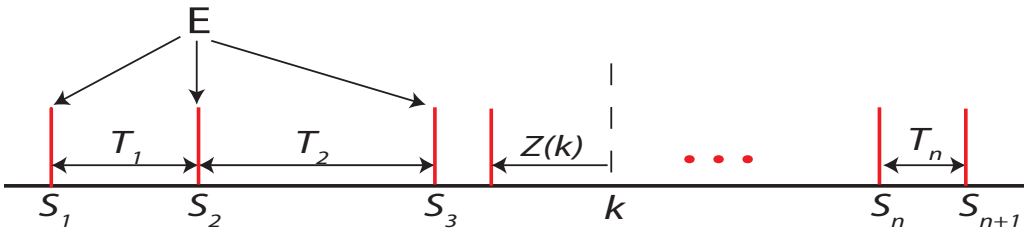

Figure 3.12: A sample realization of the event sequence, where an event is crossing the LOS link. The events occur at $S_1, S_2, \ldots, S_{n+1}$. The inter-event times are denoted by $T_1, T_2, \ldots, T_n$.

$$\begin{aligned} \text{Prob}(T_i = k) &= \text{Prob}(X_{i+k} = 1, \ldots X_{i+1} = 0 \mid X_i = 1) \\ &= \text{Prob}(X_{j+k} = 1, \ldots X_{j+1} = 0 \mid X_j = 1) \\ &= \text{Prob}(T_j = k) \ \forall \ i, j, \text{and } k, \end{aligned} \tag{3.28}$$

where Prob(.) denotes the probability of the argument. This implies that $\{T_i\}$, for $i \in \{1, 2, \ldots, n\}$, are identically distributed. If the inter-event times are also independent, then the process is called a Renewal process [83]. However, the inter-event times of our case are not necessarily independent. We thus use the term "Renewal-type process" in this dissertation, to refer to this type of process where the inter-event times are identically distributed but not independent. We next characterize the PMF of the inter-event times.

Let f denote the PMF of the inter-event times T_i. Let $Z(k)$ denote the backward recurrence time at k, i.e., the time from time instant k that we need to travel back before encountering an event, as shown in Fig. 3.12. Let $\}(\ddagger; \|)$ denote the PMF of $Z(k)$. We next characterize the relationship between f and $g(z; k)$, which we shall utilize in Section 3.4.2.

Let $h(k)$ denote the probability that $\mathcal{E}$ occurs at time k, i.e., $h(k) = \text{Prob}(k = S_j)$ for some j, where Prob(.) denotes the probability of the argument. Then, $g(z; k)$, i.e., the probability that we need to travel backward z time steps from time k to encounter an event, is the product of the probability of an event occurring at time $k - z$ and the

probability that there is no event at times $\{k-z+1, k-z+2, \ldots k-1\}$, given that an event occurs at $k-z$. Formally, $g(z;k)$ can be written as

$$g(z;k) = h(k-z)F_c(z), \tag{3.29}$$

where $F_c(z)$ is the complimentary cumulative distribution function (CCDF) of the inter-event times. As shown in [55], h is given by the following:

$$p_c \triangleq h(k-z) = \frac{2v\delta t}{B\pi},\ \forall\ k \geq z. \tag{3.30}$$

Therefore,

$$g(z;k) = p_c F_c(z),\ \forall\ k \geq z. \tag{3.31}$$

3.4.2 Motion of Multiple People as a Superposition of Renewal-type Processes

In this section, we characterize the PMF of the inter-event times when N people are walking in D and show that it contains useful information about the total number of people N. We then propose a ML estimator to estimate N, based on our characterization of the inter-event times.

Consider N people walking in the workspace D. Let $\{X_i^j\}$, for $1 \leq i \leq T$, denote the sequence of events as defined in (3.27), but for the j^{th} person. Let $\{Y_i\}$, for $1 \leq i \leq T$, denote the corresponding superposed sequence. We define $\{Y_i\}$ as $Y_i = \sum_{j=1}^{N} X_i^j$. Fig. 3.13 shows sample individual and superposed event sequences, for the case of N people, along with their sample occurrence and inter-event times. For the superposed sequence of events, we say that an event occurred at time i if $Y_i \neq 0$. In other words, an event occurs at time i if at least one person crosses the LOS link at time i. Since multiple events can

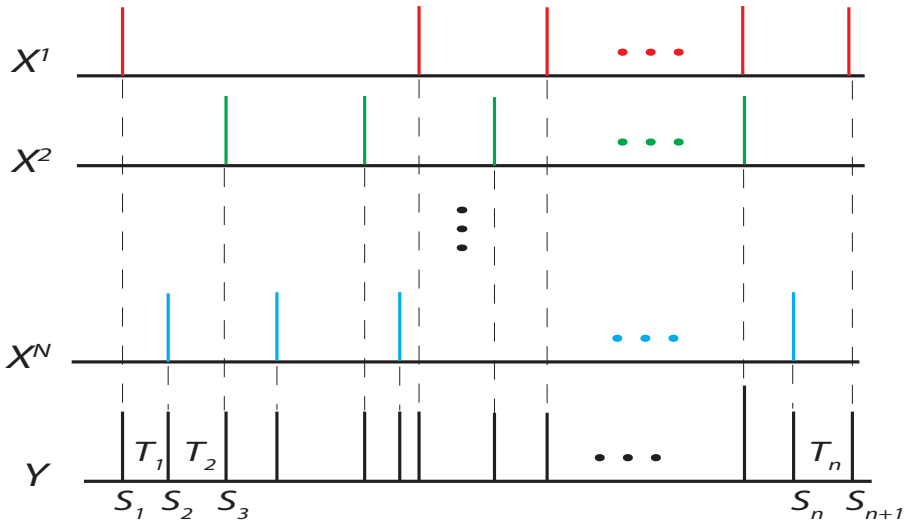

Figure 3.13: A sample realization of the event sequence (Y) for the superposed process, which corresponds to N people walking in the area of interest. An event $\mathcal{E}$ here corresponds to any crossing of the LOS link. The events occur at $S_1, S_2, \ldots, S_{n+1}$. The inter-event times are denoted by $T_1, T_2, \ldots, T_n$. The processes corresponding to individual people are also shown (X_i s).

occur at the same time, we have $Y_i \in \{0, 1, ..., N\}$. However, we do not distinguish the events based on the value of Y_i, as our proposed method does not rely on the exact values of Y_i and only depends on if it is zero or non-zero, which will result in a more robust estimator to measurement errors.

Let $f_p(z_p; N)$ denote the PMF of the inter-event times of the superposed process due to N people. Let $Z_p(k)$ and $g_p(z_p; k)$ denote the backward recurrence time at k and its corresponding PMF respectively.

Theorem 3.2 *We have the following expression for the PMF of the inter-event time:* $f_p(z_p; N) = c\Delta g_p(z_p; k), \forall\, k \geq z_p$, *where* c *is a normalizing constant that is not a function of* N, *and* Δ *is the forward difference operator.*

Proof: The backward recurrence time, $Z_p(k)$, for the superposed process can be written as

$$Z_p(k) = \min\left\{Z^1(k), Z^2(k), \ldots, Z^N(k)\right\}, \tag{3.32}$$

where $Z^j(k), \text{for } 1 \leq j \leq N$, is the backward recurrence time for the j^{th} event sequence, and $\min\{.\}$ denotes the minimum of the arguments. Then, since people are walking independently, we have,

$$\text{Prob}(Z_p(k) \geq z_p) = \prod_{j=1}^{N} \text{Prob}(Z^j(k) \geq z_p). \tag{3.33}$$

By substituting (3.31) in (3.33), we get,

$$\text{Prob}(Z_p(k) \geq z_p) = \left[\sum_{m=z_p}^{\infty} p_c F_c(m) \right]^N, \ \forall \ k \geq z_p, \tag{3.34}$$

where $F_c(.)$ is the CCDF of the inter-event times for the case of $N = 1$, and p_c is the probability of crossing for the case of $N = 1$, as defined in Section 3.4.1. From (3.34), we get the corresponding PMF as follows:

$$g_p(z_p; k) = -\Delta \text{Prob}(Z_p(k) \geq z_p), \ \forall \ k \geq z_p. \tag{3.35}$$

By following steps similar to (3.29), (3.30), and (3.31), we get the PMF of the inter-event times for the superposed process as follows,

$$\begin{aligned} f_p(z_p; N) &= c\Delta g_p(z_p; k) \quad \text{for } k \geq z_p \\ &= c\Delta \left[\left(\sum_{m=z_p}^{\infty} p_c F_c(m) \right)^N - \left(\sum_{m=z_p+1}^{\infty} p_c F_c(m) \right)^N \right]. \end{aligned} \tag{3.36}$$

This proves the theorem. ■

It can be seen from (3.36) that the PMF of the inter-event times is an implicit function of the number of people N. We next use this PMF to derive an ML-based estimator for the number of people N. Given the inter-event times, we can estimate the number of people

by maximizing the log-likelihood of the inter-event times. Specifically, assuming the inter-event times are independent, the log-likelihood of the observed inter-event times, $T_1, T_2, \ldots, T_n$, can be characterized as a function of the number of people M as follows:

$$LL(M) = \sum_{i=1}^{n} \log(f_p(T_i; M)). \tag{3.37}$$

We can then estimate the number of people by maximizing the log-likelihood function,

$$\widehat{N}_{\text{renew}} = \arg\max_{M} LL(M), \tag{3.38}$$

where $\widehat{N}_{\text{renew}}$ is the estimate of the number of people based on the underlying renewal-type process and the inter-event times. We note that we derived (3.37) under the assumption that T_i's are independent. As we mentioned earlier, this is not necessarily the case for our process. Thus, the ML estimator of (3.38) is not the optimum, but can provide a good estimate of the number of people, as we shall see in the next section, while maintaining a low computational complexity.

In order to implement our derived estimator, one needs to identify the inter-event times due to the LOS blocking. Furthermore, an estimate of $F_c(z)$, the CCDF of the inter-event times when single person is walking, is needed. In the next section, we show how the inter-event times and $F_c(z)$ can be estimated in practice.

3.5 Experimental Results

In this section, we validate our proposed framework through extensive experiments. We start by explaining our experimental setup and then present the experimental results for five different areas with up to and including 20 people.

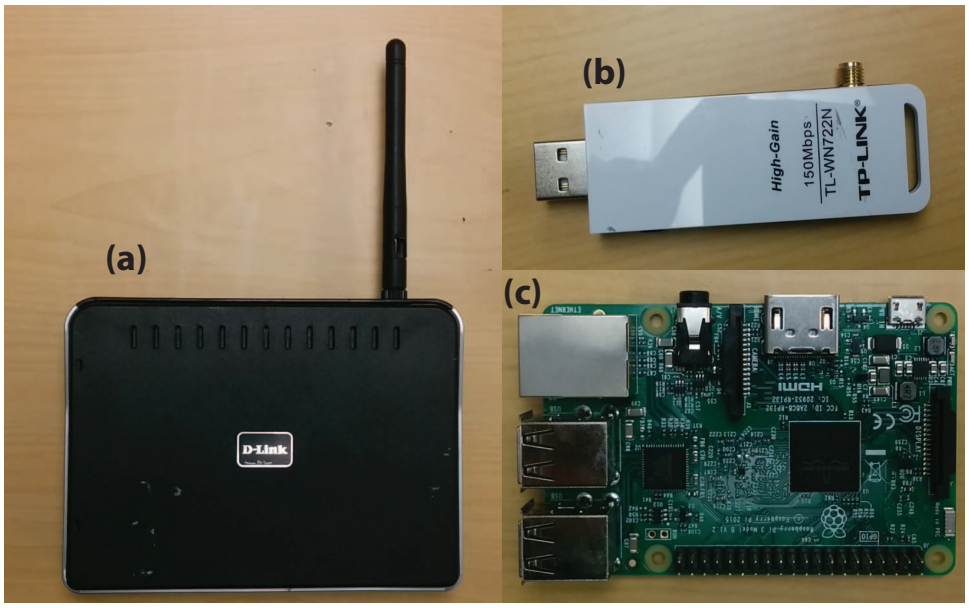

Figure 3.14: (a) D-link WBR-1310 Router used as a WiFi Tx, (b) the WLAN card used as a WiFi Rx, and (c) Raspberry Pi board that controls the measurement operation and stores the WiFi RSSI measurements.

3.5.1 Experiment Setup

As shown in Fig. 3.11, our experimental setup consists of a pair of WiFi nodes for transmission and reception of wireless signals. One of the WiFi nodes is configured as a Tx, which constantly transmits wireless signals. The other WiFi node, which acts as a Rx, measures the signals that are emitted from the Tx node and records the corresponding signal strength. We use a D-Link WBR-1310 WiFi router [84] as a Tx node, which operates using 802.11g wireless standard. For the Rx WiFi node, we use a TP-Link Wireless N150 WLAN card [85] in 802.11g mode. This wireless card needs to be interfaced with a computer in order to make WiFi measurements. In our setup, we then use a Raspberry Pi (RPI) board [86] for this purpose, i.e., to collect and store WiFi RSSI measurements. Fig. 4.2 shows the WiFi router, the WLAN card, and the RPI board used in our experiments. Omnidirectional antennas that come along with the WiFi router/card are used for transmitting and receiving the wireless signals. We use standard

2.4 GHz frequency of WiFi in all our experiments.

Using the aforementioned experimental setup, we then run several experiments when up to 20 people walk in the area of interest. We next first discuss the processing of the experimental data, which is followed by our experimental results.

3.5.2 Initial Data Processing

In Section 3.4, we developed a framework to estimate the number of people based on the PMF of the inter-event times, where an event refers to an instant of time where $l > 0$ people are crossing the LOS link. Since the RSSI measurements are significantly attenuated when people cross the LOS link. Therefore, the RSSI measurements contain information about the times at which a cross has occurred and hence about the inter-event times. However, the received measurements are not only affected by the LOS blockage but also by the multipath fading that is caused by scattering off of the people that are not necessarily on the direct LOS. Therefore, we need to identify the times at which a LOS cross has occurred in the presence of multipath.

Our analysis of several measurements has shown that the fluctuations and dips caused by multipath are typically much smaller than those caused by any LOS blockage. Fig. 3.15 (left), for instance, shows the RSSI measurements of an experiment with 9 people walking in an area, while Fig. 3.15 (right) shows the corresponding RSSI measurements in the same area but when the same number of people were instructed not to cross the LOS link. More specifically, 4 people were instructed to walk on one side of the LOS link, with the other 5 walking on the other side, without any person crossing the LOS link. Since there is no LOS blocking in this second case, the fluctuations in the RSSI measurements are solely due to the multipath effect. As can be seen, the measurements in Fig. 3.15 indicate that the effect of LOS blocking is more significant compared to

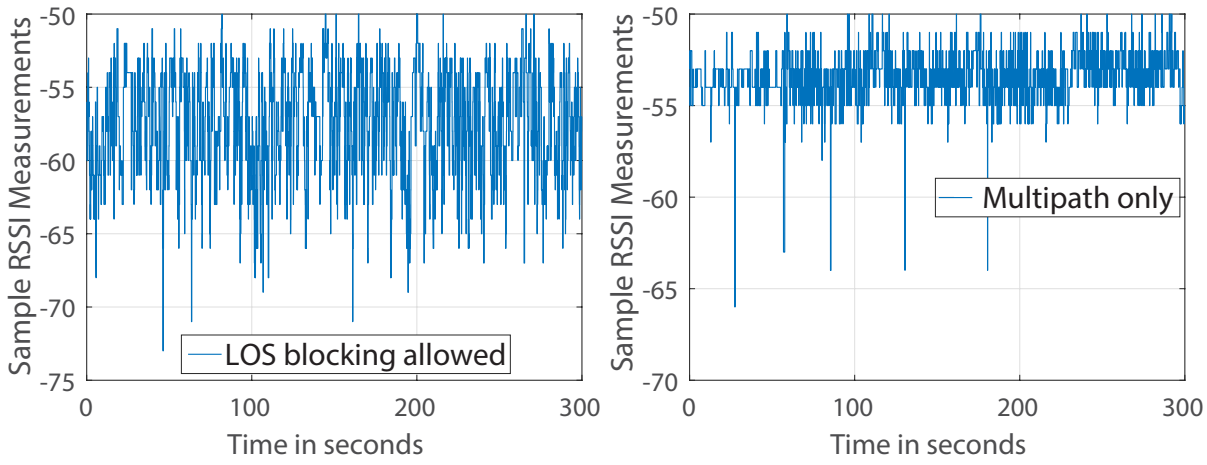

Figure 3.15: (left) shows a sample RSSI power measurement when 9 people are walking inside a building while (right) shows the RSSI power measurements in the same environment and for the same number of people when people are instructed not to cross the LOS link. The right figure thus mainly captures the fluctuations due to multipath fading. By comparing the two figures, it can be seen that the effect of LOS blocking is considerably more significant as compared to the fluctuations due to multipath.

Number of people in the Area	1	3	5	7	9
Estimated Number of People	1	3	4	7	9

Table 3.5: A sample result for counting through walls based on our proposed approach, for the classroom scenario of Fig. 3.16 on our campus (Area 1).

the multipath effect. Specifically, the fluctuations in the RSSI measurements due to multipath are concentrated around the mean level of the RSSI signal, while blocking the LOS causes a pronounced dip in the signal level.

Based on several similar observations, we then contribute any dip in the RSSI signal level that is larger than a sufficiently-large threshold, T_{LOS}, to people blocking the LOS link.[10] Furthermore, if T_{LOS} is chosen properly (not too large), then the chance of filtering a dip that was due to the LOS blockage becomes low. Thus, we utilize this approach in our experiments in order to identify the events of people crossing the LOS and hence the inter-event times.

[10]Note that we are only interested in detecting the time instants where any number of people block the LOS link, without the need to know the particular number of people that are along the LOS.

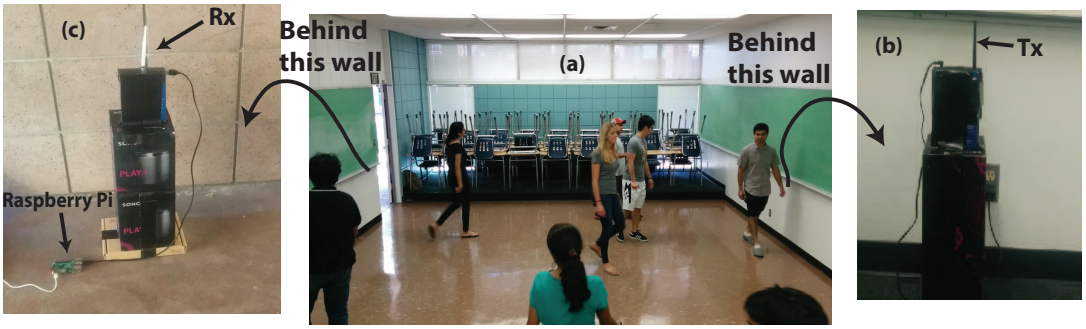

Figure 3.16: (a) The first area of interest (Area 1), a closed classroom on our campus with wall made of concrete, where people are walking, (b) the Tx WiFi node located outside the classroom, behind one of the walls of the classroom as marked, and (c) the Rx WiFi node, along with the Raspberry Pi board that is used to control the data collection, which is located outside of the classroom behind the wall that is indicated.

In terms of the choice of the threshold, we choose the threshold T_{LOS} of 5 dB in all our experiments, based on several observations similar to Fig. 3.15. This means that any dip that is larger than T_{LOS} is labeled as a LOS blockage. We note that, based on our observations, the choice of T_{LOS} is not strongly dependent on the area of interest, which allows us to set it without the need to make prior measurements in a specific area of interest. We thus use the same value of T_{LOS} in all the five areas of interest considered in the next section. Furthermore, as we shall see in the sensitivity analysis of Section 3.5.5, the threshold T_{LOS} is not sensitive to the specifics of the scenario such as the density of people and their walking speeds. Thus, T_{LOS} estimated with a specific number of people walking at a specific speed can be used to estimate a different number of people walking at other speeds, and more importantly in other areas. Finally, Section 3.5.5 explicitly shows that our experimental results are not that sensitive to the assumed T_{LOS} and moderate errors in estimating T_{LOS} are well tolerated.

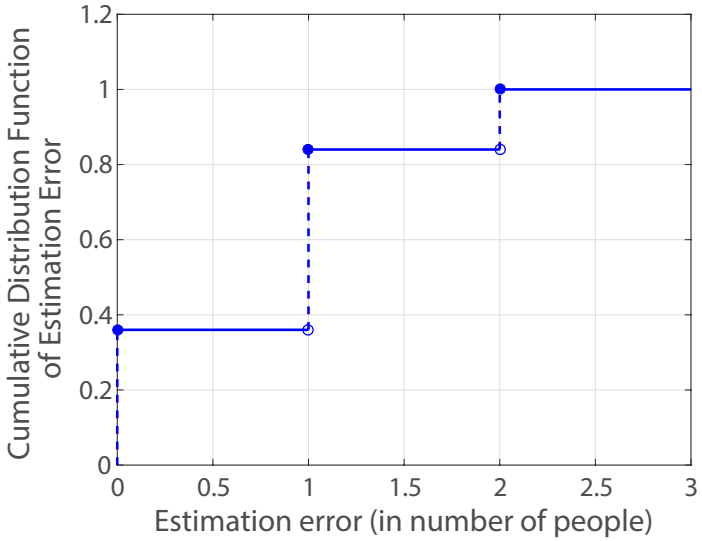

Figure 3.17: The cumulative distribution function of counting estimation error based on 5 sets of experiments in the classroom area of Fig. 3.16 on our campus (Area 1). In each set of experiment, we asked 1, 3, 5, 7, and 9 people to walk in the classroom.

3.5.3 Considering the Temporal Width of a Dip

In practice, when a person crosses the LOS, the drop in the signal level is not an impulse drop. Rather, crossing the LOS link takes a finite amount of time, which means that each dip will have a small temporal duration. Let $T_{\min}$ denote this time. Therefore, a person crossing the LOS link blocks the signal for a period of time $T_{\min}$. This then implies that we can not identify inter-event times that are less than $T_{\min}$. In other words, any two events of crossing the LOS with an inter-event time smaller than $T_{\min}$ are not identifiable. Therefore, given that we can only identify inter-event times that are larger than $T_{\min}$ in practice, we modify our derived PMF of (3.36) to account for this. Then, $T_i,\ \forall\ i \in 1, 2, \ldots, n$, is given as follows:

$$T_i | T_i \geq T_{\min} \sim f_p^{\text{mod}}(m; N) \triangleq \frac{f_p(m; N)}{\sum_{r=T_{min}}^{\infty} f_p(r; N)} \tag{3.39}$$

Figure 3.18: (left) The second area of interest between two concrete walls (Area 2), and (right) an example where people are walking in between these walls. The WiFi nodes are located outside of the area of interest, behind the walls, as indicated in the left figure. Readers are referred to the color pdf for better visibility.

Number of people in the Area	1	3	5	7	9
Estimated Number of People	3	5	6	6	7

Table 3.6: A sample result for counting through walls based on our proposed approach, for the two-wall hallway scenario of Fig. 3.18 on our campus (Area 2).

f_p in (3.37) is then replaced with f_p^{mod} to estimate the total number of people.

The value of $T_{\min}$ depends on the speed of people. In this dissertation, we have assumed that people are walking casually. Based on simple experimental tests of one person crossing a link at a walking speed, we have chosen $T_{\min} = 1$ second in our results of the next section. We note that we do not need to measure this value in the particular experimental site of interest, as it is not that dependent on a particular site, but is rather more a function of the speed of people. Furthermore, as we shall see in section 3.5.5, the experimental results are not that sensitive to the exact value of the assumed speed (and thus not that sensitive to the exact value of $T_{\min}$).

The PMF of inter-event times in (3.39) is a function of the CCDF of a single person

Number of people in the Area	3	5	7	9
Estimated Number of People	3	4	6	7

Table 3.7: A sample result for counting through walls based on our proposed approach, for the classroom scenario of Fig. 3.19 on our campus (Area 3).

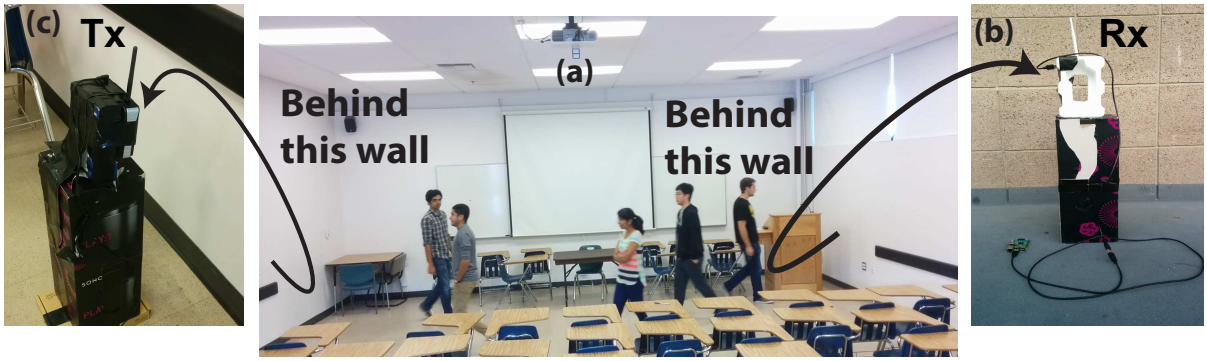

Figure 3.19: (a) The third area of interest (Area 3), a closed classroom on our campus where people are walking. The room is enclosed by concrete walls on all four sides, (b) the Rx WiFi node located outside the classroom, behind one of the walls of the classroom as marked, and (c) the Tx WiFi node which is located outside of the classroom behind the wall that is indicated.

inter-event times, $F_c(z)$, as shown in (3.36). In this dissertation, we obtain $F_c(z)$ using simulations. More specifically, we simulate motion of 1 person using the motion model. We then identify the times at which the person crosses the LOS link and extract the inter-event times. $F_c(z)$ is then obtained using these simulated inter-event times for a single person. We note that such a simulation is low in computation time (e.g., 1 s), since it involves only one person.

3.5.4 Experimental Results and Discussion

To validate the proposed framework of Section 3.4, we ran several experiments using the aforementioned experimental setup. We next present the results.

Fig. 3.16 shows the first experimental area (Area 1), which is a closed classroom on our campus, bounded by concrete walls on all four sides. We asked people to walk inside the room while the WiFi nodes are located outside of the room, as shown in Fig. 3.16. The walls are made of concrete bricks which are highly attenuating. The thickness of each wall is 20 cm based on our assessment. The dimensions of inside of the room, where people are walking, are $L = 6.3$ m and $B = 7.8$ m, with the Tx and Rx positioned at $\frac{B}{2}$

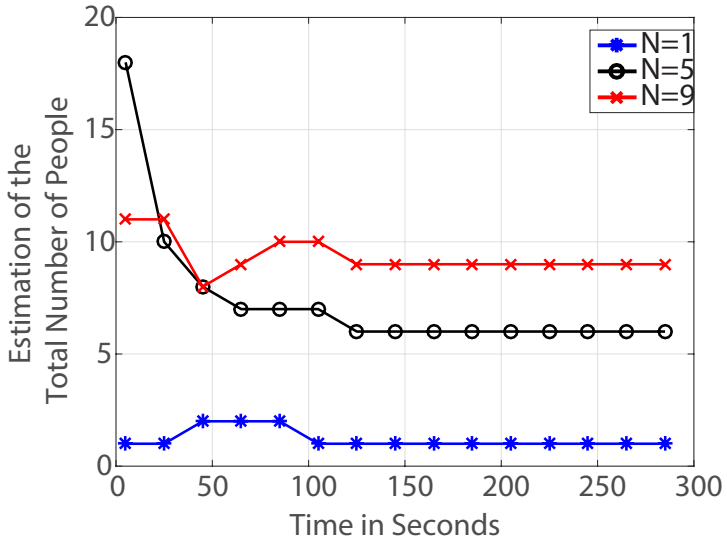

Figure 3.20: Estimation of the total number of people as a function of time, for the classroom of Fig. 3.16 (Area 1) and for the three cases where 1, 5 and 9 people are walking. It can be seen that the estimates converge to within one person of their final values within the first 100 seconds.

(See Fig. 3.11).

We have conducted several experiments in Area 1 when $1, 3, 5, 7$, and 9 people walked inside the room. In each experiment, the measurements are collected for 300 seconds at 20 samples/sec. People are assumed to have a casual walking speed, which we take it to be 1 m/s in our theoretical modeling.[11] Table 3.5 shows sample results for the estimation of the number of people. It can be seen that our approach can estimate the total number of people walking inside the classroom with a high accuracy, by making WiFi measurements from outside, behind the classroom walls. To further validate our framework statistically, we have run a series of experiments on different times/days to collect statistics of the estimation error. More specifically, we have run experiments on 5 different occasions in the classroom area of Fig. 3.16 (Area 1). In each run, $1, 3, 5, 7$, and 9 people are asked to walk in the classroom. Fig. 4.22 shows the Cumulative Distribution

[11]Note that we do not ask people to walk with a specific speed or in a specific pattern during the experiments. Instead, we simply ask them to walk casually in the area of interest.

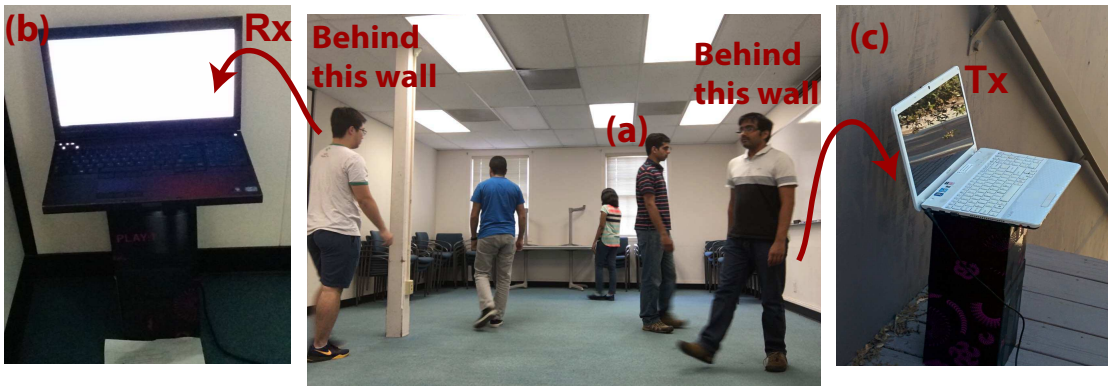

Figure 3.21: (a) The fourth area of interest (Area 4), a closed conference room on our campus where people are walking. The room is enclosed by wooden walls on all four sides, (b) the Rx WiFi node located outside the room, behind one of the walls of the room as marked, and (c) the Tx WiFi node which is located outside of the room behind the wooden wall that is indicated.

Number of people in the Area	1	2	3	4	5	6	7	8	9
Estimated Number of People	2	2	5	4	6	6	8	8	11

Table 3.8: A sample result for counting through walls based on our proposed approach, for the classroom scenario of Fig. 3.21 on our campus (Area 4).

Function (CDF) of the estimation error based on these repeated measurements. It can be seen from the CDF plot that the estimation error is 1 person or less 81% of the time and 2 people or less 100% of the time, confirming a good statistical performance.

To further validate our approach, we next run experiments in an outdoor area occluded by walls. Fig. 3.18 shows the outdoor area of interest (Area 2). As can be seen, two parallel walls are constructed with concrete bricks. The thickness of each wall is 5 cm in this case. The dimensions of the area of interest are $L = 10$ m and $B = 7$ m. People are then asked to walk in the hallway created in between the walls, while a Tx and a Rx

Number of people	1	3	5	9
Estimated Threshold (dB)	4	4	4	5

Table 3.9: Sensitivity of the estimated threshold T_{LOS} to the number of people walking in the area. It can be seen that the optimum threshold is not that sensitive to the number of people in the area.

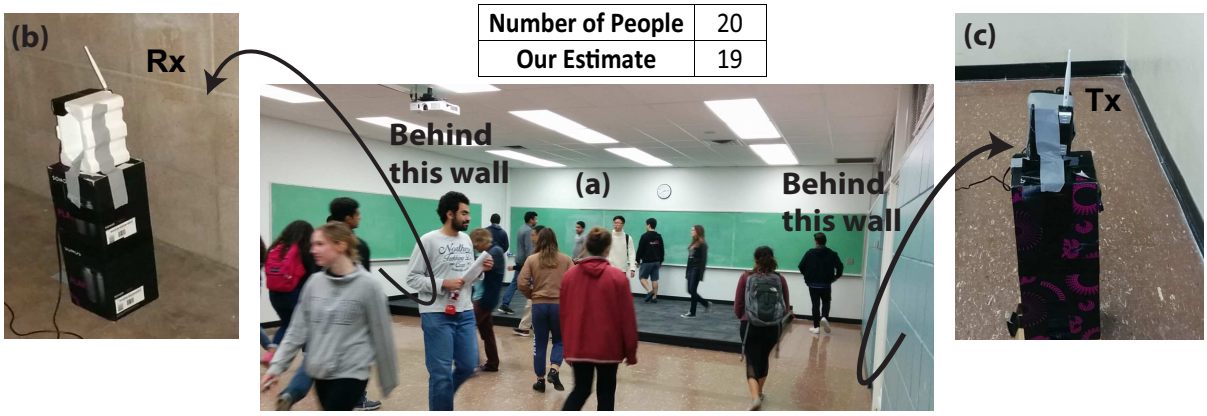

Figure 3.22: (a) The fifth area of interest (Area 5), a closed classroom on our campus where people are walking. The room is enclosed on all four sides by walls that are made of a mixture of concrete and plaster, (b) the Rx WiFi node located outside the classroom, behind one of the walls of the classroom as marked, and (c) the Tx WiFi node which is located outside of the classroom behind the wall that is indicated. The performance of our framework with 20 people walking in this area is also shown. It can be seen that our framework accurately estimates the number of people.

node are mounted outside of each wall. Table 3.6 shows a sample result obtained in Area 2. As can be seen, the number of people is estimated with a good accuracy. Fig. 3.19 shows a third area of interest (Area 3), which is another classroom on our campus. The area is bounded by concrete walls on all four sides. People walk in part of this room with the dimensions of $L = 7.8$ m and $B = 3.96$ m as shown in Fig. 3.19. Note that Area 3 has rich multipath due to the furniture in the room. Table 3.7 shows a sample result obtained in Area 3. It can be seen that the number of people are estimated accurately.

To further validate our framework with walls made of different material than concrete, we ran experiments in a room enclosed by wooden walls. Fig. 3.21 shows the fourth area of interest (Area 4), which is a conference room on our campus. The dimensions of the area of interest are $L = 4.1$ m and $B = 7.5$ m. We then run experiments with up to and including 9 people in this area. Table 3.8 shows the performance of our framework in this case. It can be seen that our framework can estimate the number of people with a high accuracy, which shows the robustness of our approach to the wall material.

So far, we demonstrated experimental results with up to and including 9 people in 4 different areas on our campus. To test the scalability of our approach, we further run experiments with 20 people walking inside a classroom. Fig. 3.22 shows the fifth area of interest which is a classroom on our campus enclosed on all four sides by walls that are made of a mixture of concrete and plaster (Area 5). The dimensions of this area are $L = 7.9$ m and $B = 12.6$ m. We then run experiments with 20 people walking inside this classroom as shown in Fig. 3.22. Our framework estimates the number of people inside as 19 in this case, which shows the scalability of our framework to the higher number of people with only one WiFi link.[12] This experiment further tests the proposed approach with a third kind of wall material, a mixture of plaster and concrete, and confirms its robustness. Overall, considering all five areas, our framework can estimate up to and including 20 people with an error of 2 people or less 100% of the time and with an error of 1 person or less 75% of the time.

So far, we have demonstrated that the proposed framework can estimate the total number of people walking inside an occluded area of interest with a high accuracy. In all the experimental results so far, we have used data collected for 300 seconds. Next, we show the time we need to wait before the estimates converge to their final values. More specifically, Fig. 3.20 shows the estimates as a function of time for an experiment with 1, 5, and 9 people for the classroom scenario of Fig. 3.16 (Area 1). It can be seen that the estimates converge to within 1 person of their final values within the first 100 seconds.

Overall, our experimental results confirm that the proposed framework can estimate the number of people inside a room or a building, or in general behind walls, solely from WiFi RSSI measurements acquired from outside, with a good accuracy.

[12]We note that as the size of the area and the number of people increases, at some point we inevitably have to use more links. However, the fact that 20 people can be counted through walls with only one WiFi link in an area of the size 100 m^2 is promising for how this approach will scale to bigger areas and more people.

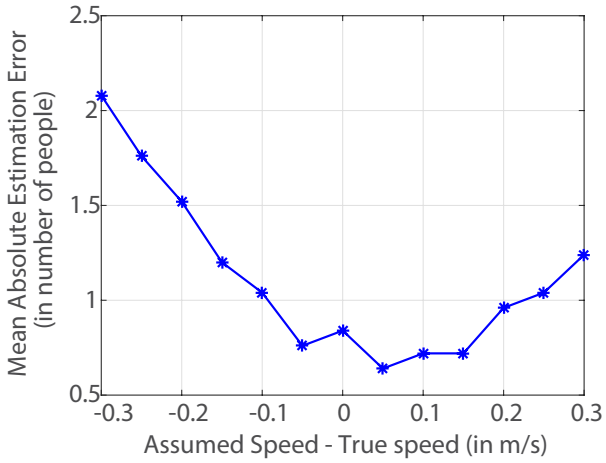

Figure 3.23: Sensitivity of our crowd counting to the errors in the assumed walking speed. The casual speed of people is assumed to be 1 m/s. Other speeds were then assumed in our derivations when estimating the number of people. It can be seen that our framework is robust to moderate errors in the assumed speed.

Speed of People	Standing Still	Normal Walking	Running
Estimated Threshold (dB)	4	5	4

Table 3.10: Sensitivity of the optimum threshold T_{LOS} to the speed of people walking in the area. It can be seen that the estimated optimum threshold is not that sensitive to the speed of people in the area.

3.5.5 Sensitivity Analysis

In the experimental results of this section, we took T_{LOS} as 5 dB and assume a walking speed of 1 m/s. We next show that the our framework is not sensitive to the exact value of T_{LOS} and the speed of people and that moderate errors in both can be well tolerated. Furthermore, we show that the estimation of T_{LOS} is not that sensitive to the specifics of the scenarios such as the density of people and their walking speeds. This then greatly reduces the calibration demand of our approach as T_{LOS} estimated with a specific number of people walking at a specific speed in the calibration phase can be used to estimate a different number of people walking at a different speed in the estimation phase. We

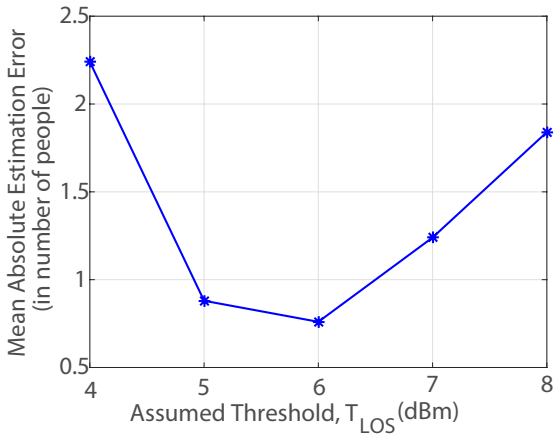

Figure 3.24: Sensitivity of our crowd counting to the errors in the assumed threshold T_{LOS}. It can be seen that our framework is robust to moderate errors in the assumed value of the threshold.

furthermore have only calibrated T_{LOS} in one area and have used it in the other 4 areas in all our experiments, which indicates the generalizability of it across different areas, further reducing the calibration burden, which is important for behind-wall scenarios.

Sensitivity to the Assumed Walking Speed

The results of Section 3.5.4 assumed that the people in the area of interest are walking at an average speed of 1 m/s, based on the typical walking speed of humans. However, the average walking speed could vary slightly from this value depending on the person or the environment, for instance due to the density of people in the region. In this section, we consider the effect of errors in the assumed walking speed (as compared to the true speed of people) on the estimation of the number of people.

In order to analyze the effect of the assumed walking speed and its deviation from the true speed of people during the experiment, consider an experiment where people are told to walk casually, which amounts to a speed of around 1 m/s. We then assume that people are walking at a speed of v m/s in our derivations and estimate the number of people based on our framework. Fig. 3.23 shows the mean absolute estimation error in the number

of people as a function of the error in the assumed walking speed. At each assumed speed, the estimates with different number of people (N=1, 3, 5, 7, and 9) walking in the classroom area of Fig. 3.16 are obtained over 5 repeated sets of experiments. The mean of the absolute error is then shown in Fig. 3.23. It can be seen that the estimation error is less than 2 people in most of the assumed speed range, showing the robust nature of our framework to small errors in the assumed walking speed of the people as compared to the true speed.

Sensitivity to the Assumed Threshold

As explained in Section 3.5.2, a threshold T_{LOS} is used to separate the dips of the wireless measurements that are due to people blocking the LOS path from the dips due to multipath. The time instants at which these dips occur are then used to estimate the number of people in the area as explained in Section 3.4. As discussed in Section 3.5.2, we have used $T_{\text{LOS}} = 5$ dB in all our results. However, the true optimal value of T_{LOS} is hard to quantify. In this section, we consider the impact of the choice of T_{LOS} on the estimates of the number of people. More specifically, we consider a range of values for T_{LOS} and estimate the number of people. At each T_{LOS}, the estimates with different number of people (N=1, 3, 5, 7, and 9) walking in the classroom area of Fig. 3.16 are obtained over 5 repeated sets of experiments. The mean of the absolute error is then shown in Fig. 3.24. As can be seen, the mean error is less than 2 people for a wide range of T_{LOS}, which shows the robust nature of our framework to moderate errors in the estimated threshold T_{LOS}.

Sensitivity of the Threshold to the Density and Speed of People

As explained in Section 3.5.2, the threshold T_{LOS} is estimated by collecting wireless measurements when people are walking without blocking the LOS link. This threshold is

then used to separate the LOS blockage from the multipath. For instance, the estimate of $T_{\mathrm{LOS}} = 5$ dB used in all our experiments is obtained in the calibration phase when 9 people are walking on either side of the LOS link in one area. In this section, we consider the effect of the number of people walking in the area and their walking speed in estimating T_{LOS}. More specifically, we let different number of people (N=1, 3, 5, and 9) walk on either side of the LOS link without blocking the LOS link as explained in Section 3.5.2. Furthermore, we let 9 people walk at three different speeds of standing still, normal walking, and running. Table 3.9 and 3.10 show the estimated threshold as a function of the number of people in the area and their walking speeds, respectively. It can be seen that the estimated threshold is not that sensitive to the number of people walking in the area or to their speeds, which explains the good accuracy of our results with different number of people and with an assumed speed of 1 m/s.

Chapter 4

Joint Crwod Counting and Crowd Speed Estimation

In this chapter, we propose a framework to sense occupancy attributes of an area, such as speed of a crowd traversing through the area, the total number of people in the area, and the rate of arrival of people into the area, using only the received power measurements (e.g., RSSI) of two WiFi links, and without relying on people to carry any device. We first show that the cross-correlation between the two WiFi link measurements and the probability of crossing a link implicitly carry key information about the occupancy attributes and develop a mathematical model to relate these parameters to the occupancy attributes of interest. Based on this, we then propose a system to estimate the occupancy attributes and validate it with 51 experiments in both indoor and outdoor areas, where up to (and including) 20 people walk in the area with different possible speeds, and show that our framework can accurately estimate the occupancy attributes. For instance, our framework achieves a Normalized Mean Square Error (NMSE) of 0.047 (4.7%) when estimating the speed of a crowd, an NMSE of 0.034 (3.4%) when estimating the arrival rate to the area, and a Mean Absolute Error (MAE) of 1.3 when counting the total number of people. We finally run experiments in an aisle in Costco, showing how we can estimate the key attributes of buyers' motion behaviors.

We then extend our framework to the scenario where we estimate the crowd speeds in multiple regions where people could be walking with different speeds by having wireless links in only one region. More specifically, we use a pair of WiFi links in one region, whose received power measurements (e.g., RSSI) are then used to estimate the crowd speed, not only in this region, but also in adjacent WiFi-free regions. We first prove how the cross-correlation and the probability of crossing the two links implicitly carry key information about the pedestrian speeds and develop a mathematical model to relate them to pedestrian speeds. We then validate our approach with 108 experiments, in both indoor and outdoor, where up to 10 people walk in two adjacent areas, with variety of speeds per region, showing that our framework can accurately estimate these speeds with only a pair of WiFi links in one region.

This chapter is organized as follows. In Section 4.2, we mathematically characterize two key statistics, the cross-correlation between two WiFi links, and the probability of crossing a link, and show how they carry vital information on the crowd speed and number of people/arrival rate, and propose a methodology to estimate them accordingly. In Section 4.3, we thoroughly validate our framework with 51 experiments where up to 20 people walk in both indoor and outdoor areas, and for both closed and open scenarios. We further test our methodology in Costco. We then describe the problem setup for multiple regions in Section 4.4. In Section 4.5, we mathematically characterize two key statistics, the probability of crossing and the cross-correlation between a pair of WiFi links, and show how they carry vital information on the speeds of pedestrians in both regions, and present a methodology to estimate these speeds accordingly. In Section 4.6, we thoroughly validate our framework with several experiments.

4.1 Problem Setup

To keep our framework applicable to many scenarios, we consider two possible general cases, as shown in Fig. 4.1. The first case (Fig. 4.1(a)), can represent a museum, a conference, or an exhibit-type setting where the total number of people inside the overall area changes slowly with time such that it can be considered constant over a small period of time. People can have any motion behavior in this area and can possibly traverse the area several times back and forth, depending on their interest. We refer to this case as the **closed area** case. The second case (Fig. 4.1(b)), on the other hand, captures the cases where people can enter and exit through both ends, and can form flow directions through the area. Then the total number of people can change rapidly with time and cannot be considered a constant. This case represents scenarios like train stations or a store aisle. We then refer to the second case as the **open area** case. As we shall show in this chapter, the estimation of occupancy attributes can be achieved under the same unifying framework for both cases, by estimating the rate of arrival of people for the open case, and the total number of people in the area (over a small period of time) for the closed case.

4.2 Proposed Methodology and System Design

In this section, we propose a system to estimate the occupancy attributes of an area, i.e., the speed of a crowd as well as the total number (or arrival rate for the open case), using only a pair of WiFi links, as shown in Fig. 4.1. More specifically, we first show that the cross-correlation between the two links is mainly a function of the crowd speed. We next derive a mathematical expression for the probability of pedestrians crossing a WiFi link. Our analysis shows that these parameters carry key information

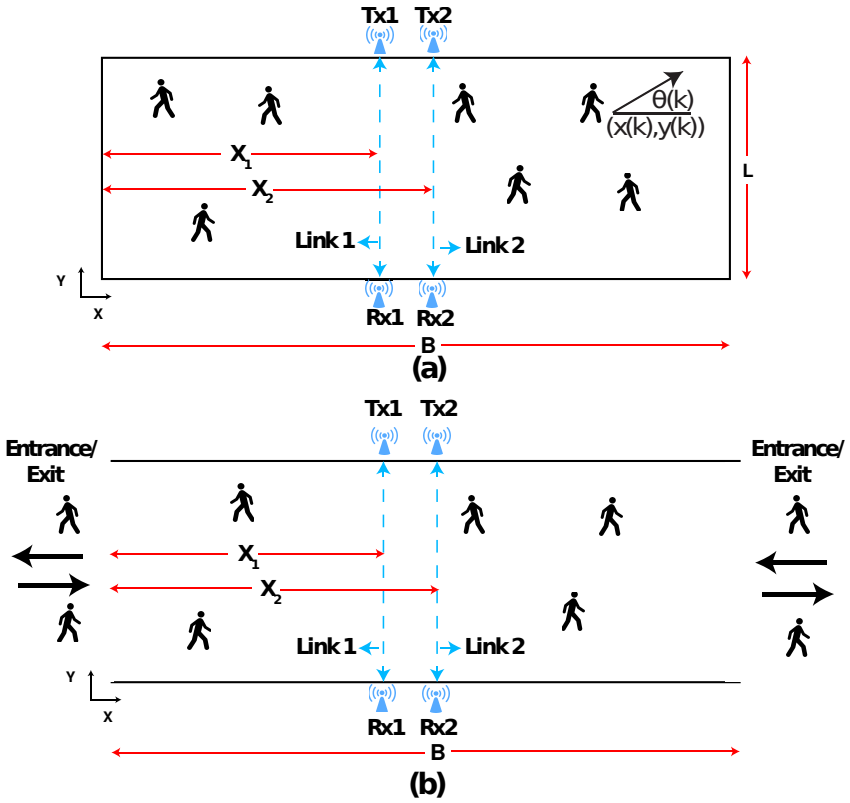

Figure 4.1: Two example scenarios of the problem of interest, (a) a closed and (b) an open area. A pair of WiFi links are located in the area. We are then interested in estimating the occupancy attributes of the area, based on only WiFi RSSI measurements of the links. (a) shows an example of a closed area, such as an exhibition or a museum, where the total number of people inside the area changes slowly with time and people can traverse back and forth or change directions inside the area any number of times depending on their interest. For a closed area, we are then interested in estimating the total number of people in the area and their walking speed, (b) shows an example of an open area such as a train station, where people can come and go from both sides and can form flow directions. In this scenario, we are then interested in estimating the walking speed and the rate of arrival of people into the area.

on the speed/number of the pedestrians, which we then use to estimate the occupancy attributes. We next start by summarizing a probabilistic model to capture the motion dynamics of a casual walk in the area, followed by discussing how occupants affect the received signal power.

4.2.1 Pedestrian Motion Model

In this chapter, we extend the pedestrian motion model developed in chapter 3, which captures casual walking patterns, to more general cases where environmental characteristics can also be captured.

Consider the motion of a single person in the workspace. Let $x(k)$, $y(k)$, and $\theta(k)$ denote the position along x-axis, the position along y-axis, and the heading of the person w.r.t. the x-axis, at time k, respectively, as marked in Fig. 4.1(a). In a casual walk, a person keeps walking in a particular direction while occasionally changing his/her direction. This walking pattern can then be captured by the following model as discussed in chapter 3:

$$\theta(k+1) = \begin{cases} \theta(k) & \text{with probability } p \\ \text{Uniformly in } \mu & \text{with probability } 1-p. \end{cases} \tag{4.1}$$

For the case of Fig. 4.1(a), people can change their direction any time and can traverse the area back and forth as many times as they wish. In this chapter, we make the motion model more general by using $\mu = [-\theta_{\max},\ \theta_{\max}] \cup [\pi - \theta_{\max},\ \pi + \theta_{\max}]$, to capture this behavior. $\theta_{\max}$ then defines the maximum angle for the direction of motion, and is an environment-dependent parameter. For instance, in long hallways, people may have a pattern more close to a straight line, resulting in a smaller $\theta_{\max}$, while in a supermarket, people may often deviate from a straight line to check out grocery items. Parameterizing the motion model with $\theta_{\max}$ then allows us to capture the characteristics of different environments. For this closed-area case, we assume that when a person encounters any of the four boundaries of the area, she/he reflects off of the boundary, similar to a ray of light.[1]

[1]This boundary behavior is only assumed for the purpose of modeling. In our experiments, we have

For the case of open area of Fig. 4.1(b), on the other hand, we assume that people walk mainly in the forward direction, entering from one end, and exiting from the opposite end of the area. Such a motion behavior can characterize the motion in many open areas, such as exhibitions and aisles. Thus, we take $\mu = [-\theta_{\max},\ \theta_{\max}]$ or $\mu = [\pi - \theta_{\max},\ \pi + \theta_{\max}]$ depending on the direction of motion.

Based on Eq. (4.1), the position dynamics are then given as follows for both open and closed cases:

$$\begin{aligned} x(k+1) &= x(k) + v\delta t\ \cos(\theta(k)) \\ y(k+1) &= y(k) + v\delta t\ \sin(\theta(k)), \end{aligned} \tag{4.2}$$

where δt is the time step and v is the walking speed.

Our proposed methodology relies on the LOS blockage events. Thus we first extract the LOS blockage event sequence from the RSSI measurements, as explained in Chapter 3.

4.2.2 Cross-correlation to Estimate the Crowd Speed

In this section, we propose to use the cross-correlation between the LOS event sequences, corresponding to the two WiFi links, and show that it contains implicit information about the walking speed of the pedestrians in an area.

Consider the closed area of Fig. 4.17(a). Let $Y_1(k)$ and $Y_2(k)$ denote the event sequences corresponding to Link 1 and Link 2, defined as,

$$Y_i(k) = \begin{cases} l & \text{if } E_l \text{ happens at time } k \\ 0 & \text{otherwise} \end{cases}, \text{ for } \ i \in \{1, 2\},$$

no control over how people walk.

where E_l denotes an event corresponding to l people blocking the LOS path. The cross-correlation between the two event sequences, $Y_1(k)$ and $Y_2(k)$, is then given by

$$R_{Y_1Y_2}(\tau, v) = \frac{\mathrm{Cov}\Big(Y_1(k), Y_2(k+\tau)\Big)}{\sqrt{\mathrm{Var}\Big(Y_1(k)\Big)\mathrm{Var}\Big(Y_2(k+\tau)\Big)}}, \tag{4.3}$$

where τ represents the time-lag, and Cov(. , .), and Var(.) denote the covariance and variance of the arguments, respectively. Since the pedestrians walk independent of each other, we have, $Y_i(k) = \sum_{j=1}^{N} Y_i^j(k)$, for $i \in \{1, 2\}$, where $Y_i^j(k) = 1$ if the j^{th} person blocks Link i at time k, and is 0 otherwise. N is the total number of people in the area, which we take to be constant over the estimation period for the closed case.

Lemma 4.1 *The cross-correlation, $R_{Y_1Y_2}(\tau, v)$, between the event sequences $Y_1(k)$ and $Y_2(k)$ is a function of only the speed of the people v in the area and is independent of the number of people in the area for the case of closed area.*

Proof: Consider the closed area of Fig. 4.17(a). Since we assume independent motion for the pedestrians, it can be easily confirmed that the numerator and the denominator of Eq. (4.3) are proportional to N, resulting in the cross-correlation becoming independent of N. This can be seen by substituting $Y_i(k)$ in (4.3), and further simplifications, which results in

$$R_{Y_1Y_2}(\tau, v) = \frac{\Pr(Y_2^j(k+\tau) = 1 | Y_1^j(k) = 1) - p_{c,\text{single person}}}{1 - p_{c,\text{single person}}}, \tag{4.4}$$

for any $j \in \{1, 2, \cdots, N\}$, where $p_{c,\text{single person}}$ denotes the probability of crossing a link by a single person. While it is considerably challenging to derive a closed-form expression for the cross-correlation, the dependency on the crowd speed can be easily seen. For instance, the first term in the numerator of Eq. (4.4), $\Pr(Y_2^j(k+\tau) = 1 | Y_1^j(k) = 1)$, is

the probability that the j^{th} person is at Link 2 at time $k+\tau$, given that she/he is at Link 1 at time k. Clearly this depends on the speed at which the j^{th} person is walking. Hence the cross-correlation in Eq. (4.4) contains information about the speed of the pedestrians. ■

Lemma 4.2 *For the case of the open area, the cross-correlation $R_{Y_1Y_2}(\tau, v)$ is a function of only the speed of the people v and is independent of the rate of arrival, when the arrivals follow a Poisson process.*

Proof: The Lemma can be proved after a few lines. We skip the proof due to space limitations. ■

For the case of open area of Fig. 4.1(b), deriving an expression for the cross-correlation, for a general arrival process distribution is considerably challenging. However, our extensive simulations with various speed and arrival rate combinations show that the cross-correlation is mainly a function of the speed of the people in the area.

The strong dependency of the cross-correlation on the crowd speed, for both open and closed cases, then allows us to devise a simple low-complexity approach for estimating it. More specifically, we simulate a single person walking in the area, according to the motion dynamics in Eq. (4.2) and with different possible speeds, and generate the event sequences corresponding to the two links in the area. We then generate a database for the cross-correlation function $R_{Y_1Y_2}(\tau, v)$ for a range of walking speeds v. Since the cross-correlation is independent of the number of people in the area, the database for $R_{Y_1Y_2}(\tau, v)$, obtained with 1 person walking in the area (or one rate of arrival for the open case), is valid for any number of people in the area. This makes the database generation a one-time and low complexity operation. The walking speed in an area is

then estimated by matching the cross-correlation with the database as follows:

$$\widehat{v} = \min_{v} \sum_{\tau=0}^{\tau=T} \Big(R^{\text{exp}}_{Y_1,Y_2}(\tau) - R_{Y_1,Y_2}(\tau, v) \Big)^2, \tag{4.5}$$

where $R^{\text{exp}}_{Y_1,Y_2}(\tau)$ is the cross-correlation between the two event sequences obtained during the real experiment.

4.2.3 Characterization of the Probability of Crossing

To build a complete picture of occupancy attributes, we next show that the pair of links can also estimate the total number of people or their arrival rate to the area as well. We first characterize the probability of crossing for the case of the closed area of Fig. 4.1(a), the analysis of which is more involved since a person can reverse the direction of motion anytime and can bounce back and forth in the area as many times as he/she wishes. We then show how to extend the analysis to the case of open area of Fig. 4.1(b), putting everything under one unifying umbrella. A key feature of our analysis is using a generalized motion model where different motion behaviors can be captured through the parameter $\theta_{\max}$ of Section 4.2. We then show how to derive a mathematical expression for the probability of crossing a link, under this motion model.

Head Counting for the Case of Closed Area

Consider Fig. 4.1(a) and the motion model of Eq. (4.2). Since the heading, and the positions along the x-axis and y-axis at time $k+1$, depend only on the corresponding values at time k, we use a Markov chain model to describe the motion dynamics of each pedestrian. We then use the properties of the corresponding Markov chain to mathematically derive the probability of crossing a given link by a single pedestrian and show its dependency on the walking speed of the pedestrian. This is then followed by

characterizing the probability that any number of people cross a given link, and showing its dependency on the total number of people and their speed.

For the purpose of modeling, we discretize the work-space and assume that people can choose only discrete positions along x-axis, y-axis, and the heading direction.[2] More specifically, $\theta(k) \in \mu^d = \{-\theta_{\max},\ -\theta_{\max} + \Delta\theta,\ \cdots,\ \theta_{\max}\} \cup \{\pi - \theta_{\max},\ \pi - \theta_{\max} + \Delta\theta,\ \cdots, \pi + \theta_{\max}\}$, $x(k) \in \{0,\ \Delta x,\ \cdots,\ B\}$, and $y(k) \in \{0,\ \Delta y,\ \cdots,\ L\}$, where $\Delta\theta$, Δx, and Δy denote the discretization step size for heading and position along x-axis and y-axis respectively. Let N_θ denote the number of discrete angles for the heading.

Let $\Theta(k)$ denote the random variable representing the heading of a pedestrian at time k. Let $\pi^\theta(k)$ represent the corresponding probability vector with the i^{th} element $(\pi^\theta(k))_i = \Pr(\Theta(k) = (\mu^d)_i)$, where $\Pr(.)$ is the probability of the argument, and $(\mu^d)_i$ denotes the i^{th} element of the set μ^d. Then from Eq. (4.1), we have the following Markov chain for the heading $\Theta(k)$:

$$\pi^\theta(k+1) = \pi^\theta(k) P^\Theta, \tag{4.6}$$

where P^Θ is the probability transition matrix for the heading with $(P^\Theta)_{ij} = \Pr(\Theta(k+1) = (\mu^d)_j | \Theta(k) = (\mu^d)_i)$ and is given by $(P^\Theta)_{ij} = \delta(i-j) \times p + \frac{1-p}{N_\theta} = (P^\Theta)_{ji}$, where $\delta(.)$ is the Dirac-delta function, $N_\theta = \text{card}(\mu^d)$, and $\text{card}(.)$ denotes the number of elements in the argument. Since the probability transition matrix P^Θ is symmetric, it is a doubly-stochastic matrix, which implies a uniform stationary distribution for $\Theta(k)$ [75]. This implies that the probability that a pedestrian heads in any given direction (in μ^d) is the same asymptotically.

Let $X(k)$ denote the random variable representing the position of a pedestrian along the x-axis at time k. Similar to the heading direction, we can describe the dynamics of $X(k)$ using a Markov chain. Let P^X denote the corresponding probability transition

[2]This is only for the purpose of mathematical characterization. In practice, the position and heading of the pedestrians are naturally not limited to these discrete values.

matrix for $X(k)$. Similar to the heading dynamics we can show that the stationary distribution of $X(k)$ and $Y(k)$ are uniform [55]. We next use these properties of the motion dynamics to derive the probability that a pedestrian crosses the LOS path.

We say that a pedestrian crosses/blocks a given link[3] located at X_i along the x-axis, at time $k+1$, if either $x(k+1) \geq X_i$ and $x(k) \leq X_i$ or $x(k+1) \leq X_i$ and $x(k) \geq X_i$. Consider Fig. 4.1(a) and the motion model of Eq. (4.1)-(4.2). Consider a time interval T, discretized to δt. We then define the probability of crossing link i as follows:

$$p_c = \text{Number of blockage events in time interval [0 T]} \times \frac{\delta t}{T}$$

We then have the following theorem for the probability of crossing a link by a single pedestrian.

Theorem 4.1 *The probability of crossing a link by a single pedestrian in the area is given by* $p_{c,\text{single person}} = \frac{v\delta t \ \text{sinc}(\theta_{\max})}{B}$, *where* $\text{sinc}(\theta_{\max}) \triangleq \frac{\sin(\theta_{\max})}{\theta_{\max}}$ *with* $\theta_{\max}$ *in radians.*

Proof: See the appendix for the proof of this Theorem. ■

We next consider the probability of crossing when there are N people in the area. Since, we assume that people in the area walk independent of each other, the probability of crossing, p_c is given as $p_c(N, v) = 1 - (1 - p_{\text{c, single person}})^N$. The number of people in the area can then be estimated as follows:

$$\widehat{N} = \min_N (p_c(N, \widehat{v}) - p_c^{\text{exp}})^2, \tag{4.7}$$

where $p_c^{\text{exp}} = \frac{p_{c,1}^{\text{exp}} + p_{c,2}^{\text{exp}}}{2}$ and $p_{c,i}^{\text{exp}}$ for $i \in \{1, 2\}$, is the probability of crossing corresponding to Link i obtained from the experiment.

[3]In this chapter, we consider WiFi links that are located parallel to the y-axis (see Fig. 4.1). However, the derivation of the probability of crossing can be extended to any general link configuration following a similar approach.

Remark 4.1 If $\theta_{\max}$ is assumed 90 the derivation of Theorem 1 simplifies to the expression derived in [55]. Theorem 1 then generalizes the derivation of p_c to accommodate any $\theta_{\max}$, thus making it applicable to any environment.

Rate of Arrival Estimation for the case of Open Area

Consider the scenario of Fig. 4.1(b) in which people can enter/exit from either side of the area as marked. In this case, the number of people in the area changes with time and hence it is a random variable. As we discussed in Section 4.2.2, the cross-correlation is mainly a function of the speed of people, and thus Eq. (4.24) can be utilized to estimate the speed of the pedestrians for both open and closed areas. However, we need to extend the probability of crossing analysis to the case of time-varying number of people in order to estimate the rate of arrival to the area, as we show in this part.

Let λ denote the rate of arrival of people into the area (from both ends). In scenarios modeled by the open area, such as a retail store, people typically enter an aisle, spend a random amount of time in the area depending on their interest, before exiting it. Therefore, assuming that the rate of departure is the same as the rate of arrival λ is a reasonable assumption. Furthermore people typically walk mainly in the forward directions rarely turning back. Under these assumptions, the probability of crossing a link in the area can be related to the rate of arrival into the area as follows:

$$p_c = \text{Number of events in time interval [0 T]} \times \frac{\delta t}{T} = \lambda \delta t.$$

We then estimate the rate of arrival, λ, from the crossing probability of each WiFi link as $\widehat{\lambda} = \frac{p_{c,1}^{\exp} + p_{c,2}^{\exp}}{2\delta t}$.

4.3 Performance Evaluation

In this section, we evaluate the performance of our proposed system using extensive experiments. We start with several experiments in closed areas, where different number of people (up to 20) walk with a variety of speeds, in both indoor and outdoor environments, and show that our proposed approach can accurately estimate the occupancy attributes. In particular, our experiments with 20 people show that our system can estimate occupancy attributes for highly-dense areas. We then show our experimental results for the open-area cases, in both outdoor and indoor environments. Finally, we test our system in a local retail store, Costco, to estimate the rate of arrival and the speed of people in an aisle. Overall, our extensive tests indicate that the proposed approach can accurately estimate the occupancy attributes for both closed and open areas.

4.3.1 Experiment Setup

In all our experiments, a pair of WiFi links, located in the area of interest, make RSSI measurements as people walk in the area. Each WiFi link uses a WBR 1310 router as a Tx and a TP-Link wireless N150 WLAN card as a receiver. The Rx of each WiFi link is interfaced with a RaspberryPi (RPI) which controls the data collection operation and stores the corresponding RSSI measurements. Fig. 4.2 shows the WiFi router, WLAN card, and RPI used in our experiments. This setup is used in all the experiments of the chapter.

In order to derive the cross-correlation from the experimental data, the receivers of the two WiFi links need to be synchronized in time. To achieve this, we interface the Rx nodes of both WiFi links to the same RPI and program them to receive the wireless signals from their corresponding transmitters at the same time instants. The data is collected at a rate of 20 samples/second at each receiver of the WiFi link. Each link is

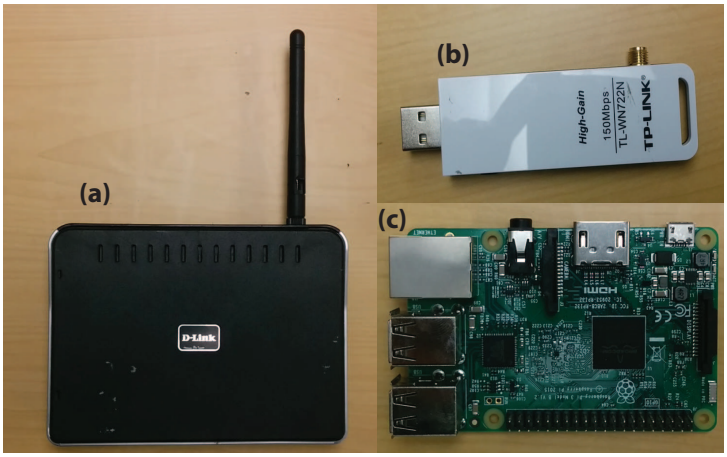

Figure 4.2: (a) D-Link WBR 1310 wireless router along with an omni-directional antenna, (b) the TP-Link wireless N150 WLAN card, (c) Raspberry Pi board used to control the data collection process and synchronize the two WiFi links.

configured to operate in a different sub-channel of the 2.4 GHz wireless band to avoid any interference. Specifically, we use sub-channel 1, which operates at 2.41 GHz for one link, and sub-channel 11, which operates at 2.47 GHz, for the other link. This separates the two links by the widest frequency margin.

Pedestrian Walking Speeds

As shown in Fig 4.1, our experiments involve different number of people walking at different speeds in the area. We consider three different speeds 0.3 m/s (slow), 0.8 m/s (normal walking), and 1.6 m/s (fast) in our experiments. We ask people to walk casually at a given speed in an experiment. To help people walk at the correct speed, we make use of a mobile application called "Frequency Sound Generator" which generates an audible tone every second. Each person then listens to this application on his/her mobile and takes a step of length v. This ensures correct speeds for people walking in the area. In order to take steps of length v, we have people practice their step lengths to match v prior to the experiments. This procedure is employed only to ensure an accurate ground-truth for the speeds, which is used in assessing the performance of our approach. In our

experiments in the aisle of Costco, the speeds of people are naturally determined by their interests in each region, and as such there is no control over peoples' speeds.

Separation of LOS from MP

As shown in Section 4.2, our framework is based on the event sequences of a pair of WiFi links located in the area, with the events corresponding to people crossing a WiFi link. Therefore, we need to first extract the event sequences of each WiFi link from the corresponding RSSI measurements. We next describe this process.

To convert the RSSI measurements into an LOS event sequence, we first identify all the dips in the RSSI measurements and the associated times at which the dips occur. Let k_j^i, for $j \in \{1, 2, \cdots, J_i\}$, denote these times for link i, and let $Z_i(k_j^i)$ denote the corresponding RSSI measurement at time k_j^i on link i. The event sequence, $Y_i^{\exp}(k)$, for $i \in \{1, 2\}$, is then obtained from the RSSI measurements as follows:

$$Y_i^{\exp}(k) = \begin{cases} l & \text{if } k = k_j^i \text{ and } Z_i(k_j^i) \text{ is closest to } R_{l,i} \\ 0 & \text{otherwise} \end{cases},$$

where $R_{l,i}$ denotes the RSSI measurement of the i^{th} WiFi link when l people simultaneously block the i^{th} link. We find the values of $R_{l,i}$ by performing a small calibration phase in which l (up to 2) people simultaneously block the i^{th} WiFi link and the corresponding RSSI is measured.[4] Note that small variations in $R_{l,i}$ due to factors such as different dimensions of people crossing the WiFi link have a negligible impact on our results. For instance, we collect $R_{l,i}$ data for only 2 people in the calibration phase, while a total of 10 different people walk in each campus experiment.

[4]We need to collect this only for small l as the probability of l people simultaneously blocking the LOS link is negligible for higher l.

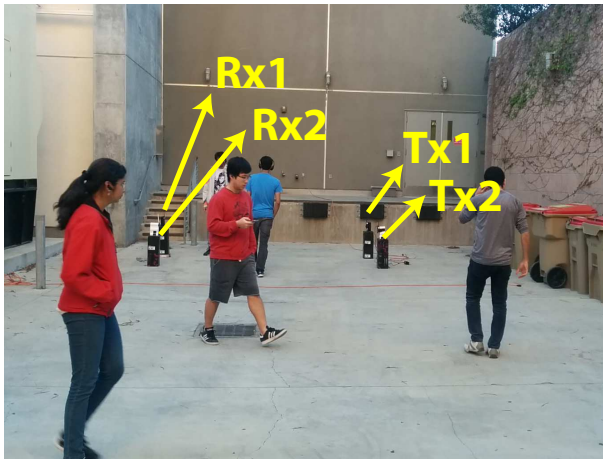

Figure 4.3: The outdoor area of interest. The dimensions of the area are $L = 4.26\ m$ and $B = 14.3\ m$. Two WiFi links, each consisting of a transmitter and a receiver, are located in the area, as marked.

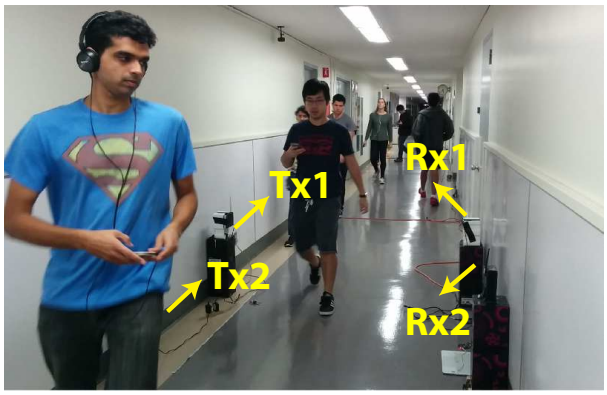

Figure 4.4: The indoor area of interest. The dimensions of the area are $L = 4.26\ m$ and $B = 9.76\ m$. Two WiFi links are located in the area, as marked on the figure.

4.3.2 Experimental Results and Discussion

In this section, we extensively validate our proposed system with several experiments using the aforementioned experiment setup. We first show our results for the case of closed area, followed by the open area, and the retail store results.

Closed Area: Fig. 4.3 and 4.4 show the considered outdoor and indoor closed areas of interest respectively. The dimensions of the outdoor area are $B = 14.3\ m$ and $L = 4.26\ m$ and the transceivers are marked on the figure. For the case of indoor, on

Figure 4.5: A snapshot of the experiment when a large number of people (20) are walking in the indoor area of interest.

True Headcount and Speed $(N,\, v)$	Estimated Headcount and Speed in Outdoor Area $(\widehat{N},\, \widehat{v})$	Estimated Headcount and Speed in Indoor Area $(\widehat{N},\, \widehat{v})$
(5, 0.3)	(5, 0.4)	(6, 0.5)
(5, 0.8)	(4, 0.9)	(4, 1)
(5, 1.6)	(4, 1.9)	(4, 1.6)
(9, 0.3)	(10, 0.4)	(9, 0.5)
(9, 0.8)	(9, 0.9)	(10, 0.9)
(9, 1.6)	(7, 1.9)	(7, 1.9)

Table 4.1: Sample performance of our proposed system to estimate the total number and the speed of the people in closed areas – the middle and right columns show the performance for the outdoor area of Fig. 4.3 and the indoor area of Fig. 4.4 respectively.

the other hand, the dimensions are $B = 20\ m$, $L = 2.25\ m$, and the transceivers are marked on the figure. In our first series of experiments, we collect measurements in these areas when 5 and 9 people walk with 3 different speeds in each area (6 different possibilities). Table 4.1 then shows the estimates of the occupancy attributes obtained by our system in the outdoor and indoor areas. It can be seen that the proposed system accurately estimates both the number of people and their walking speeds in both indoor and outdoor settings.

NMSE of Speed Estimates	MAE of Headcount Estimates
0.046 (4.6%)	1.3 person

Figure 4.6: Average performance (averaged over several trials) in closed areas – the table shows the Normalized Mean Square Error (NMSE) of the speed estimation, and the Mean Absolute Error (MAE) of head counting, based on several experiments in both indoor and outdoor settings.

True Headcount and Speed (N, v)	Estimated Headcount and Speed ($\widehat{N}$, $\widehat{v}$)
(20, 0.3)	(22, 0.4)
(20, 1.6)	(19, 1.6)

Figure 4.7: Performance of our system in very crowded areas – the table shows the performance when 20 people walk, with a variety of speeds, in the indoor area of Fig. 4.5. It can be seen that our approach can estimate the speed and number of people accurately even at high crowd densities.

To further validate our system statistically, we repeat experiments for each combination of N and v on 3 different days for both the indoor and outdoor areas, running a total of 36 experiments. Table 4.6 then shows the NMSE of the speed estimation of all the experiments as 0.046 (i.e., 4.6%) and the MAE in estimating the total number of people as 1.3, which further confirms the high accuracy of our proposed system. Fig. 4.8 and 4.9 further show the cumulative distribution function (CDF) of the normalized square error (NSE) for speed estimation and the CDF of the absolute error for head counting, respectively. It can be seen that the NSE of speed estimation is less than or equal to 0.1, 92% of the time, and the occupancy estimates are within 1 person error 70% of the time and within 2 people error 92% of the time, thus establishing the robust nature of our proposed system. We further note that the proposed system has a low computational complexity. For instance, it took 0.2 seconds to solve for the case of $N = 20$ and $v = 0.3$. Furthermore, it converges after collecting RSSI measurements for a couple of minutes, with several cases (those with higher speeds) converging in much less than a minute.

We next consider the impact of the environment on the estimation performance. More specifically, Fig. 4.10 and 4.11 compare the CDF error curves of the indoor and outdoor areas, for speed estimation and head counting respectively. It can be seen that both the

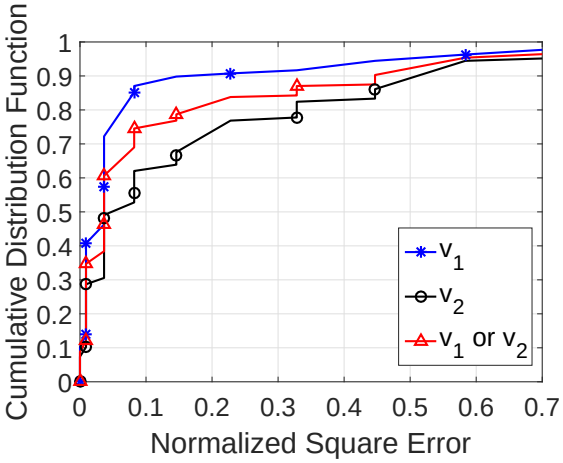

Figure 4.8: CDF of the NSE for crowd speed estimation in closed areas (both indoor and outdoor). It can be seen that our approach can estimate the crowd speed with a good accuracy.

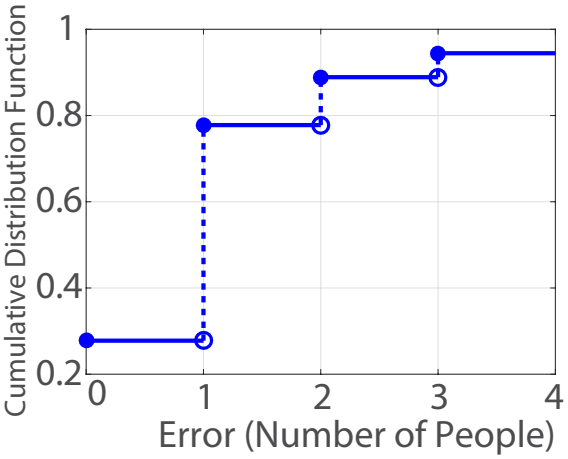

Figure 4.9: CDF of the absolute error for head counting in closed areas. It can be seen that our approach can estimate the number of people with a good accuracy.

indoor and outdoor areas have similar performances.

To further validate our proposed system in very dense areas, we run a number of experiments where 20 people walked in the area of Fig. 4.5, with 2 different speeds. As the figure shows, the area can get very crowded when 20 people are present. Table 4.7 then shows the performance of our system. It can be seen that our approach can estimate the occupancy attributes well even when the area is considerably dense.

Open Area: In this section, we validate the performance of our proposed system in open areas. More specifically, we run experiments in the same outdoor and indoor areas of Fig. 4.3 and 4.4 but we allow people to enter/exit the area. In other words, people enter the area from one side, walk in the area at the given speed, but with any motion pattern they desire, and then exit the area from the other end. We then run several experiments for different combinations of rate of arrival into the area and walking speed in the area. More specifically, we consider Poisson-distributed arrival times with two rates of 0.2 person/second and 0.1 person/second, and walking speeds of 0.3, 0.8,

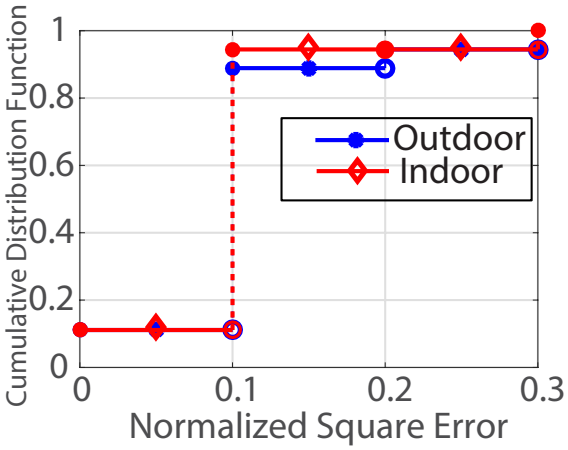

Figure 4.10: CDF of the NSE for crowd speed estimation as a function of the location. It can be seen that the performance in outdoor and indoor locations are comparable.

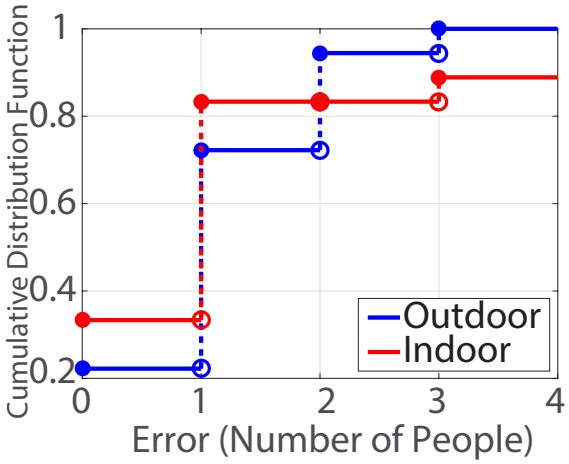

Figure 4.11: CDF of the absolute error for head counting as a function of the location. It can be seen that the performance in outdoor and indoor locations are comparable.

True Arrival Rate and Crowd Speed (λ, v)	Estimated Arrival Rate and Speed in Outdoor Area $(\widehat{\lambda}, \widehat{v})$	Estimated Arrival Rate and Speed in Indoor Area $(\widehat{\lambda}, \widehat{v})$
(0.2, 0.3)	(0.2, 0.4)	(0.22,0.4)
(0.2, 0.8)	(0.16, 0.8)	(0.21, 0.7)
(0.2, 1.6)	(0.15, 1.6)	(0.14, 2.2)
(0.1, 0.3)	(0.1, 0.3)	(0.14, 0.1)
(0.1, 0.8)	(0.1, 1)	(0.1, 1)
(0.1, 1.6)	(0.09, 1.5)	(0.08,2)

Figure 4.12: A sample performance of our system when estimating the arrival rate and speed of the people in open areas – the middle and right columns show the performance for the outdoor area of Fig. 4.3 and indoor area of Fig. 4.4 respectively, while the left column shows the groundtruth.

and 1.6 m/s. Table 4.12 shows the performance of our approach when estimating the arrival rate and speed of a crowd, for both outdoor and indoor areas. It can be seen that the proposed system can accurately estimate the occupancy attributes of an open area. Fig. 4.13 and 4.14 further show the CDF of the normalized square error for speed and arrival rate estimation respectively. It can be seen that the NSE of speed estimation is

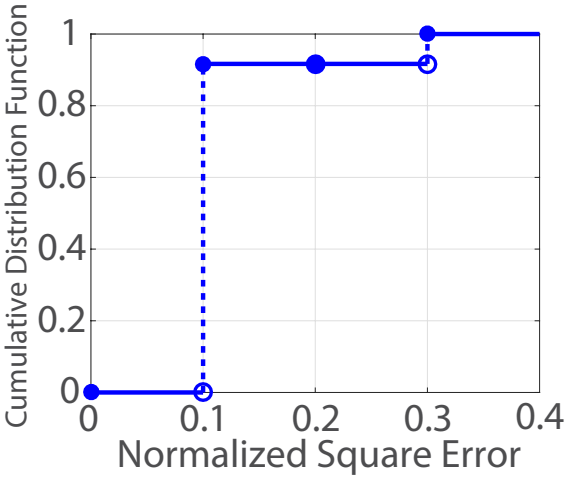

Figure 4.13: CDF of the NSE for crowd speed estimation in open areas (both indoor and outdoor). It can be seen that our approach can estimate the crowd speed with a good accuracy.

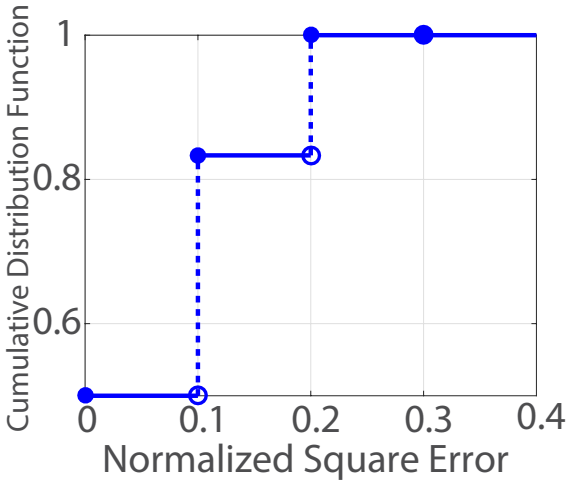

Figure 4.14: CDF of the normalized square error for crowd arrival rate estimation in open areas (both indoor and outdoor). It can be seen that our approach can estimate the crowd arrival rate with a good accuracy.

within 0.1, 83% of the time, and the NSE of rate estimation is within 0.2, 100% of the time, thus establishing the robust nature of our proposed system.

Costco Experiments

In this section, we use our proposed system to estimate the motion behavior of the buyers in an aisle of a retail store, Costco. Since people constantly come and go through the aisle, this will be an example of the open area scenario. We then estimate the rate of arrival of people into the aisle, and the speed at which people walk while they are exploring the aisle, thus assessing the popularity of the products in the aisle.

Fig. 4.15 shows the aisle of interest in our local Costco. This aisle contains a specific type of merchandise, snacks and cookies in this case. Both ends of the aisle are open and people can enter/exit from either end of the aisle. It is expected that people walk at a slow pace if the products in the aisle generate interest and they consider buying them. We are thus interested in estimating such behaviors. A pair of WiFi links are located

Figure 4.15: The Costco experiment – the figure shows the considered "snacks and cookies" aisle in Costco along with a pair of WiFi links positioned along the aisle to make wireless measurements.

along the aisle, as indicated in Fig. 4.15, and make wireless measurements as people walk through the aisle. We then use our approach of Section 4.2 to estimate the speed of people in the aisle as well as their rate of arrival into the aisle.

More specifically, we collect wireless RSSI measurements for 15 minutes as people walk through the aisle shown in Fig. 4.15. We manually record the times at which people arrive from either entrance of the aisle, through visual observation since camcording was not allowed, and compute the true rate of arrival. Fig. 4.16 shows the estimated rate of arrival as a function of time. It can be seen that our framework accurately estimates the rate of arrival of people into the aisle using a pair of WiFi links. Note that the rate of arrival on that particular day/time was 1 person per minute (or 0.016 people/second). Thus, our estimation converges relatively fast, within 400 seconds, which is the time 6

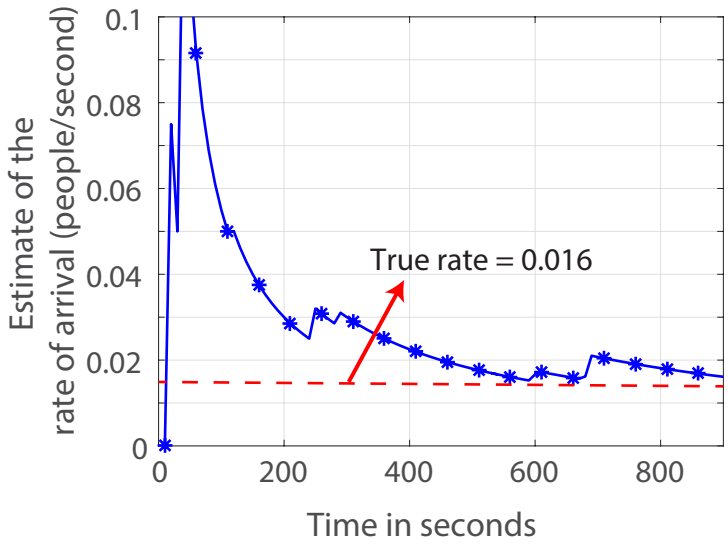

Figure 4.16: The estimate of the rate of arrival of people into the aisle of Fig. 4.15 at Costco, as a function of time. It can be seen that our framework correctly estimates the rate of arrival.

people visited the aisle. Furthermore, the average ground-truth speed of people walking in that aisle is estimated as 0.48 m/s, by manually recording the entrance and exit times of people. The average speed of people walking in the aisle is then estimated as 0.2 m/s using our framework, which is consistent with the ground-truth, and indicates a significant slowdown, showcasing the popularity of the aisle.

Overall, our extensive experiments (total of 51) confirm that the proposed approach can estimate the crowd speed and total number (or arrival rate) robustly and with a high accuracy.

4.4 Problem Setup: Two Regions

In this section, we consider the scenario where N pedestrians are walking in an area that consists of two adjacent regions, Region 1 and Region 2, with region-dependent speeds, as shown in Fig. 4.17. A pair of WiFi links are located in one region, which make RSSI measurements as people walk in the two regions. The goal of this section is to

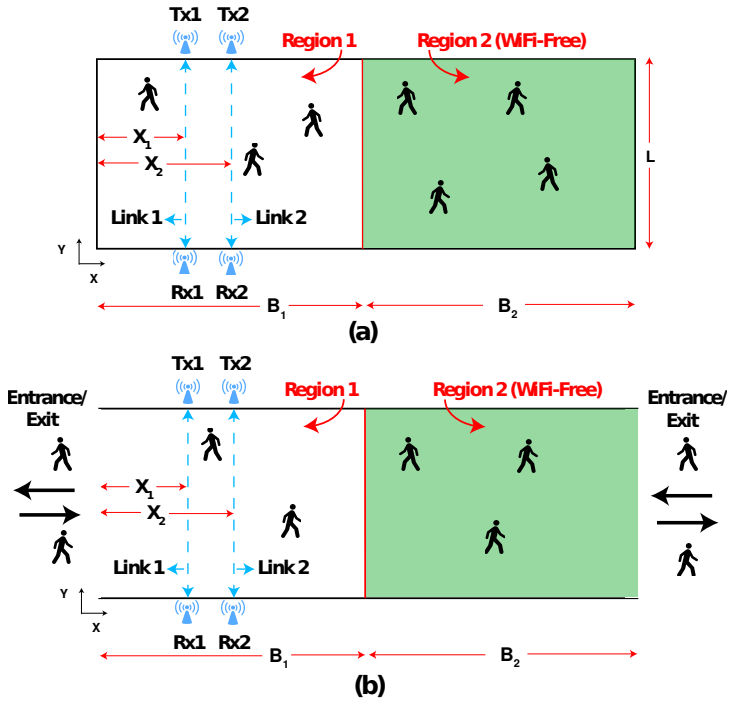

Figure 4.17: Two example scenarios of the problem of interest, where an area consists of two regions, Region 1 and Region 2, as indicated. People move casually throughout the area with a specific speed in each region. A pair of WiFi links are located in Region 1. We are then interested in estimating the region-dependent speeds of both regions, based on only WiFi RSSI measurements of the links and signal availability in Region 1. (a) shows an example of a closed area, such as an exhibition or a museum, where the total number of people inside the area changes slowly with time and people can traverse back and forth or change directions inside the area any number of times depending on their interest, whereas (b) shows an example of an open area such as a train station, where people can come and go from both regions and can form flow directions.

estimate the speeds of the pedestrians in the two adjacent regions, using the WiFi measurements of the links located in one region. As we show in this section, the estimation of the region-dependent speeds can be achieved for both cases under the same unifying framework. We assume that, N, the total number of people in the area (or N_{avg}, the average number of people for time-varying cases such as Fig. 4.17b) is known. Assuming the knowledge of the total number of people in the area is reasonable for many applications. For instance, in stores, there may be mechanisms (such as door sensors) to count

the total number of people in the store. Then, it would be of interest to estimate the speed of shoppers in different regions. We further note that the total number of people can also be estimated with additional sensing in the area. Thus, in this section we focus on estimating the region-dependent speeds, assuming N (or N_{avg}), and based on minimal sensing in only one region.

4.5 Estimation of pedestrian speeds: two regions

In this section, we propose a framework to estimate the region-dependent speed of pedestrians in two adjacent regions, using a pair of WiFi links located in only one region, as shown in Fig. 4.17. More specifically, we first derive a mathematical expression for the probability of pedestrians crossing a WiFi link. We then characterize the cross-correlation between the two links. Our analysis shows that these parameters carry key information on the speeds of the pedestrians in both regions, which we then use to estimate the speeds. A key feature of our approach is that it only relies on WiFi signal availability in the region where the links are but can deduce the speed of the crowd in the adjacent possibly WiFi-free region. In this section, we first characterize the probability of crossing and the cross-correlation for the case of the closed area of Fig. 4.17a, the analysis of which is more involved since a person can reverse the direction of motion anytime and can bounce back and forth in the area as many times as he/she wishes. We then show how to extend the analysis to the case of open area of Fig. 4.17b, putting everything under one unifying umbrella.

4.5.1 Probability of Crossing a Link

Consider Fig. 4.17a and the motion model of Eq. (4.1)-(4.2). Since the heading, and the positions along the x-axis and y-axis at time $k+1$, depend only on the corresponding

values at time k, we use a Markov chain model to describe the motion dynamics of each pedestrian. We then use the properties of the corresponding Markov chain to mathematically derive the probability of crossing a given link by a single pedestrian and show its dependency on the speeds of each region. This is then followed by characterizing the probability that any number of people cross a given link. We note that the probability of crossing problem of interest to this section is considerably different from that of [55], since there are two regions with links in only one region. As such, a new characterization and methodology is required as we develop in this section.

For the purpose of modeling, we discretize the work-space and assume that people can choose only discrete positions along x-axis, y-axis, and the heading direction.[5] More specifically, $\theta(k) \in \mu^d = \{-\theta_{\max},\ -\theta_{\max} + \Delta\theta,\ \cdots,\ \theta_{\max}\} \cup \{\pi - \theta_{\max},\ \pi - \theta_{\max} + \Delta\theta,\ \cdots, \pi + \theta_{\max}\}$, $x(k) \in \{0,\ \Delta x,\ \cdots,\ B_1 + B_2\}$, and $y(k) \in \{0,\ \Delta y,\ \cdots,\ L\}$, where $\Delta\theta$, Δx, and Δy denote the discretization step size for heading and position along x-axis and y-axis respectively. Let N_θ denote the number of discrete angles for the heading. Furthermore, let N_1 and N_2 represent the number of discrete positions along the x-axis in Region 1 and Region 2 respectively.

Let $\Theta(k)$ denote the random variable representing the heading of a pedestrian at time k. Let $\pi^\theta(k)$ represent the corresponding probability vector with the i^{th} element $(\pi^\theta(k))_i = \text{Prob}(\Theta(k) = (\mu^d)_i)$, where Prob(.) is the probability of the argument, and $(\mu^d)_i$ denotes the i^{th} element of the set μ^d. Then from Eq. (4.1), we have the following Markov chain for the heading $\Theta(k)$:

$$\pi^\theta(k+1) = \pi^\theta(k) P^\Theta, \tag{4.8}$$

where P^Θ is the probability transition matrix for the heading with $(P^\Theta)_{ij} = \text{Prob}(\Theta(k+$

[5] This is only for the purpose of mathematical characterization. In practice, the positions and heading of the pedestrians are naturally not limited to these discrete values.

1) = $(\mu^d)_j|\Theta(k) = (\mu^d)_i)$ and is given by $(P^\Theta)_{ij} = \delta(i-j) \times p + \frac{1-p}{N_\theta} = (P^\Theta)_{ji}$, where $\delta(.)$ is the Dirac-delta function, $N_\theta = \text{card}(\mu^d)$, and card(.) denotes the number of elements in the argument. Since the probability transition matrix P^Θ is symmetric, it is a doubly-stochastic matrix, which implies a uniform stationary distribution for $\Theta(k)$ [75]. This implies that the probability that a pedestrian heads in any given direction (in μ^d) is the same asymptotically.

Let $X(k)$ denote the random variable representing the position of a pedestrian along the x-axis at time k. Similar to the heading direction, we can describe the dynamics of $X(k)$ using a Markov chain. Let P^X denote the corresponding probability transition matrix for $X(k)$. We then have the following lemma for the stationary distribution of $X(k)$.

Lemma 4.3 *The stationary distribution of $X(k)$ is given by $\gamma = [c_1 e_1 \; c_2 e_2]$, where c_1, c_2 are constants, and e_1, e_2 are N_1 and N_2-dimensional row-vectors with all their elements as 1.*

Proof: Let P^X be partitioned as $P^X = \begin{bmatrix} P_{11} & P_{12} \\ P_{21} & P_{22} \end{bmatrix}$, where P_{11} is a square matrix of dimension N_1. Further, P_{ij}, for $i, j \in \{1, 2\}$, specify the transition probabilities from positions in Region i to positions in Region j. The stationary distribution of the partitioned transition matrix P^X is shown in [87] to be $\gamma = [k_1\gamma_1 \; k_2\gamma_2]$, where k_1 and k_2 are constants, and γ_1 and γ_2 are the stationary distribution vectors corresponding to the probability transition matrices, S_{11} and S_{22}, defined as follows:

$$\begin{aligned} S_{11} &= P_{11} + P_{12}(I_{N_2} - P_{22})^{-1}P_{21} \\ S_{22} &= P_{22} + P_{21}(I_{N_1} - P_{11})^{-1}P_{12}, \end{aligned} \tag{4.9}$$

where I_{N_1} and I_{N_2} are the identity matrices of dimensions N_1 and N_2 respectively.

Consider any two positions, $r\Delta x$ and $q\Delta x$, along the x-axis that are in the same region (i.e., with the same speed). Then, based on [55], $\text{Prob}(r\Delta x \rightarrow q\Delta x) = \text{Prob}(q\Delta x \rightarrow r\Delta x)$, where $\text{Prob}(r\Delta x \rightarrow q\Delta x)$ denotes the probability of going from $q\Delta x$ to $r\Delta x$ in one time step. Since the speed of the pedestrians is the same within a region, we then have,

$$P_{11} = P_{11}^T \text{ and } P_{22} = P_{22}^T. \tag{4.10}$$

Furthermore, by choosing the step size Δx such that $q\Delta x$ can be reached from $r\Delta x$ in one time step if and only if $|q - r| \leq 1$, we have the following property for P_{12} and P_{21}.

$$\begin{aligned} &(P_{12})_{ij} \neq 0 \text{ iff } i = N_1, j = N_1 + 1 \\ &(P_{21})_{ij} \neq 0 \text{ iff } i = N_1 + 1, j = N_1. \end{aligned} \tag{4.11}$$

By substituting Eq. (4.10) and (4.11) in (4.9), we get, $S_{11} = S_{11}^T$ and $S_{22} = S_{22}^T$. Since S_{11} and S_{22} are symmetric, the corresponding stationary distributions are uniform, implying $\gamma_1 = \frac{e_1}{N_1}$, and $\gamma_2 = \frac{e_2}{N_2}$. Therefore, the stationary distribution of P^X is $\gamma = [c_1 e_1 \; c_2 e_2]$, where $c_1 = \frac{k_1}{N_1}$ and $c_2 = \frac{k_2}{N_2}$ are constants. This proves the lemma. ■

Lemma 1 states that the position of a pedestrian along the x-axis has a uniform asymptotic distribution within each region.

We next derive the probability that a pedestrian crosses a link, given that the pedestrian is in a region where there is a link (Region 1 in this case). We then use this conditional probability of crossing the link, along with Lemma 1, to derive the overall probability of crossing. We first mathematically define crossing/blocking a link. We then have the following lemma for the conditional probability of crossing a given link, given that the pedestrian is in the region where there is a link.

Lemma 4.4 *Given that a person is in Region 1, the probability of crossing a given link in*

Region 1 is given by $p_{c|1} = \frac{v_1 \delta t \ \mathrm{sinc}(\theta_{\max})}{B_1}$, *where* $\mathrm{sinc}(\theta_{\max}) \triangleq \frac{\sin(\theta_{\max})}{\theta_{\max}}$ *with* $\theta_{\max}$ *in radians.*

Proof: Consider a link located in Region 1 of Fig. 4.17a, whose x-coordinate is X_i. X_i, for instance, can represent X_1 or X_2 of Fig. 4.17a. Let the position of the person at time k be $x(k) \leq X_i$. The person crosses the link at time $k+1$, if he/she chooses a direction $\theta(k)$ at time k such that $x(k) + v_1 \delta t \cos(\theta(k)) \geq X_i$, which results in $|\theta(k)| \leq \cos^{-1}\Big(\frac{X_i - x(k)}{v_1 \delta t}\Big)$, where $|.|$ is the absolute value of the argument. Since $|\theta(k)| \leq \theta_{\max}$, in order to cross the link, the heading direction should be as follows:

$$|\theta(k)| \leq \min\Big\{\theta_{\max},\ \cos^{-1}\Big(\frac{X_i - x(k)}{v_1 \delta t}\Big)\Big\}. \tag{4.12}$$

Since the heading direction is uniformly distributed over μ^d, the probability that a person at $x(k)$ crosses the link in Region 1 at time $k+1$, $p_{c|1}^{x(k)}$, is given by,

$$p_{c|1}^{x(k)} = \frac{\min\Big\{\theta_{\max},\ \cos^{-1}\Big(\frac{X_i - x(k)}{v_1 \delta t}\Big)\Big\}}{2\theta_{\max}},\ \text{for } x(k) \leq X_i. \tag{4.13}$$

By symmetry, it can be seen that $p_{c|1}^{x(k)}$, for $x(k) \geq X_i$, is given by,

$$p_{c|1}^{x(k)} = \frac{\min\Big\{\pi - \theta_{\max},\ \pi - \cos^{-1}\Big(\frac{x(k) - X_i}{v_1 \delta t}\Big)\Big\}}{2\theta_{\max}}, \tag{4.14}$$

The probability of crossing the link given the person is in Region 1, $p_{c|1}$, is then obtained by summing over all the positions in Region 1 from which a cross can occur:

$$p_{c|1} = \sum_{x(k) = X_i - v_1 \delta t}^{X_i + v_1 \delta t} \frac{\Delta x}{B_1} p_{c|1}^{x(k)}, \tag{4.15}$$

where $\frac{\Delta x}{B_1}$ is the probability that a pedestrian is located at any given position in Region

1. By substituting Eq. (4.13) and (4.14) in (B.1) and letting $\delta t \to 0$, we get,

$$p_{c|1} = \frac{1}{2B_1\theta_{\max}} \int_{X_i - v_1\delta t}^{X_i + v_1\delta t} \min\Big\{\theta_{\max},\ \cos^{-1}\Big(\Big|\frac{X_i - x(k)}{v_1\delta t}\Big|\Big)\Big\} dx. \tag{4.16}$$

By simplifying Eq. (4.16) further, we get

$$p_{c|1} = \frac{v_1\delta t \sin(\theta_{\max})}{B_1\theta_{\max}}, \tag{4.17}$$

which proves the lemma. ■

By using Lemma 1 and Lemma 2, we then have the following theorem for the probability of crossing a given link by a single pedestrian.

Theorem 4.2 *The probability of crossing a given link by a single pedestrian,* $p_{c,\text{single person}}$*, walking with the speed* v_1 *in Region 1 and speed* v_2 *in Region 2, is given by,* $p_{c,\text{single person}} = \frac{v_1 v_2 \delta t \,\text{sinc}(\theta_{\max})}{v_1 B_2 + v_2 B_1}$.

Proof: The probability of crossing a given link in Region 1 by a single pedestrian is given by,

$$p_{c,\text{single person}} = c_1\ p_{c|1}, \tag{4.18}$$

where c_1, defined in Lemma 1, denotes the probability of the pedestrian being in Region 1, and $p_{c|1}$ is the conditional probability that the pedestrian crosses the given link in Region 1, if he/she is in Region 1.

To find the probability c_1, we use the pseudo-aggregation properties of the underlying Markov chain [88]. More specifically, for the transition matrix P^X, defined in Lemma 1, with a stationary distribution of the form $[c_1 e_1\ c_2 e_2]$, the constants c_1 and c_2 are given

by the stationary distribution of the probability transition matrix P, as we show next.

$$P = \begin{bmatrix} p_{11} & p_{12} \\ p_{21} & p_{22} \end{bmatrix}, \tag{4.19}$$

where $p_{ij} = \frac{\mathbf{1}^T P_{ij} \mathbf{1}}{N_i}$, for $i, j \in \{1, 2\}$, and $\mathbf{1}$ denotes a column vector whose elements are all 1. We can then prove that the stationary distribution of P in Eq. (4.19) is (c_1, c_2) [88].

It can be seen that p_{12}, is the probability of crossing from Region 1 to Region 2. From Lemma 2, we have,

$$p_{12} = \frac{p_{c|1}}{2} \text{ and } \; p_{21} = \frac{p_{c|2}}{2}. \tag{4.20}$$

By substituting Eq. (4.20) in (4.19) and solving for the stationary distribution of P, we have, $c_1 = \frac{v_2 B_1}{v_1 B_2 + v_2 B_1}$, and $c_2 = \frac{v_1 B_2}{v_1 B_2 + v_2 B_1}$. The probability of crossing a given link in Region 1 by a single pedestrian can then be characterized as follows,

$$p_{c,\text{single person}} = c_1 \; p_{c|1} = \frac{v_1 v_2 \delta t \; \text{sinc}(\theta_{\max})}{v_1 B_2 + v_2 B_1}. \tag{4.21}$$

This proves the theorem. ■

Remark 4.2 Note that if there was a link in Region 2, the probability of a single pedestrian crossing it would have been the same. This can be seen from the expression for $p_{c,\text{single person}}$ by interchanging B_1 with B_2 and v_1 with v_2. Further, note that the probability of crossing is independent of the location of the link within Region 1.

Since there are N people walking in the area, we next characterize the probability that any number of people cross a given link, $p_c(v_1, v_2)$, assuming that pedestrians' motions

are independent. We then have the following for the closed case:

$$p_c(v_1, v_2) = 1 - (1 - p_{\text{c, single person}})^N. \tag{4.22}$$

From Eq. (4.22), it can be seen that the probability of any number of pedestrians crossing the link is a function of the speeds of the pedestrians in both regions. Furthermore, from Remark 1, we can see that the probability of crossing a link in Region 2, if there was one in Region 2, will not provide any additional information in terms of the speeds in Region 1 and 2, as it has the same exact function form as the probability of crossing a link in Region 1. In other words, it would not have been possible to estimate the speeds by utilizing two links, one in Region 1 and one in Region 2.

4.5.2 Characterizing the Cross-correlation

As explained in Section 4.2.2, the cross-correlation in Eq. (4.4) contains information about the speeds of people in both regions for the scenarios of both open and closed areas. However, given the vicinity of the two links, and by considering all the possible motion patterns of the people, it can be easily seen that the cross-correlation carries more information on the speed of Region 1, as compared to Region 2. As such, in the next part, we utilize it for the estimation of the speed in Region 1, as we shall see.

4.5.3 Speed Estimation for the Closed Area

As shown in Sections 4.5.1 and 4.2.2, the probability of crossing a WiFi link, and the cross-correlation between the two WiFi links, carry key information about the speeds of the pedestrians in the two adjacent regions. Equations (4.22) and (4.4) further model these relationships, which we then use to estimate the speeds of the pedestrians in the two regions.

Let Y_1^{exp} and Y_2^{exp} denote the event sequences, corresponding to the two WiFi links, obtained from an experiment. Let $R_{Y_1,Y_2}^{\text{exp}}(\tau)$ denote the cross-correlation between the event sequences Y_1^{exp} and Y_2^{exp}, and let $p_{c,1}^{\text{exp}}$, $p_{c,2}^{\text{exp}}$ denote the probability of crossing Link 1 and Link 2 respectively. The probability of crossing can be computed from the event sequences as follows:

$$p_{c,i}^{\text{exp}} = \frac{\delta t}{T} \times \text{Number of events in } Y_i^{\text{exp}}, \text{ for } i \in \{1, 2\}, \tag{4.23}$$

where T denotes the total time for which the data is collected, and δt is the discretization step size.

Since the cross-correlation of Eq. (4.4) is independent of the total number of people, N, we first estimate v_1 from the cross-correlation without assuming the knowledge of N. Then, given N and an estimate of the speed in Region 1, i.e., $\widehat{v_1}$, we use the probability of crossing in Eq. (4.22) to estimate the speed in Region 2. More specifically, we have,

$$\begin{aligned} \widehat{v_1} &= \min_{v_1,v_2} \sum_{\tau=0}^{\tau=T} \left(R_{Y_1,Y_2}^{\text{exp}}(\tau) - R_{Y_1,Y_2}(\tau, v_1, v_2) \right)^2 \\ \widehat{v_2} &= \min_{v_2} \left(p_c^{\text{exp}} - p_c(\widehat{v_1}, v_2) \right)^2, \end{aligned} \tag{4.24}$$

where $p_c^{\text{exp}} = \frac{p_{c,1}^{\text{exp}} + p_{c,2}^{\text{exp}}}{2}$. In other words, given that each link will have the same probability of cross, we average the experimental probability of crossing of the two links in order to reduce the impact of errors. We further only estimate v_1 from the cross-correlation, since it is heavily dependent on v_1, as discussed earlier. As for evaluating $R_{Y_1,Y_2}(\tau, v_1, v_2)$, we utilize simulations, which are low complexity since the cross-correlation is independent of N and can thus be simulated for only one person. More specifically, for any given speed pair, we simulate one person walking in the area and generate the event sequences corresponding to the two links in the area. $R_{Y_1,Y_2}(\tau, v_1, v_2)$ is then obtained by computing

the cross-correlation between the two event sequences. Finally, the parameter $\theta_{\max}$ in $p_c(v_1, v_2)$ is assumed to be 45n all our results of the closed areas in the next section since they involve long hallways. We note that our results are not very sensitive to this choice of $\theta_{\max}$, and $\theta_{\max}$ for a wide range of angles near 45ill lend similar results as we shall see in the next section.

4.5.4 Speed Estimation for the Open Area

Consider the open area scenario shown in Fig. 4.17b. The number of people in the area can change during the sensing period and should be considered a random variable. However, as explained in Section III-C, since the cross-correlation is not a function of the number of people, Eq. (4.24) can still be used to estimate the speed v_1. We next show how to characterize the probability of crossing for the open area in order to estimate v_2.

Let λ denote the rate of arrival of people into the area (from both regions). We assume that the rate of departure of people from the area is also λ. This will be the case as long as the average number of people, N_{avg}, averaged over a small time interval, does not change significantly with time. Furthermore, we assume that each person mainly has a forward flow, i.e., she/he mainly walks in a forward direction and rarely turns back. The probability of crossing a link is then related to the rate of arrival as follows:

$$\begin{aligned} p_c(v_1, v_2) =& \text{Number of events in time interval [0 T]} \times \frac{\delta t}{T} \\ =& \lambda \delta t, \end{aligned} \tag{4.25}$$

To relate p_c to the average speed of people in the two regions, we next use a theory from queuing systems.

Consider the overall area as a queuing system in which every person is serviced until the person exits. Then, the Little's law of queuing theory [89] relates the average number

of people being serviced, N_{avg}, to the average time spent in the area by a person, T_{avg}, and the rate of arrival, λ, as follows:

$$N_{\text{avg}} = \lambda T_{\text{avg}}. \tag{4.26}$$

Since we assume that people mainly walk in a forward direction, the average time spent in the corridor can be approximated as follows:[6]

$$T_{\text{avg}} \approx \frac{B_1}{v_1} + \frac{B_2}{v_2}. \tag{4.27}$$

From Eq. (4.25), (4.26), and (4.27), we can characterize the probability of crossing in terms of the speeds of people in the two regions as follows:

$$p_c(v_1, v_2) \approx \frac{N_{\text{avg}} v_1 v_2}{v_1 B_2 + v_2 B_1} \delta t. \tag{4.28}$$

v_1 and v_2 can then be estimated by substituting Eq. (4.28) in Eq. (4.24).

Remark 4.3 *Consider the expression derived for p_c of Eq. (4.22), for the closed case. If we assume that the probability of simultaneous crosses are negligible, we can approximate Eq. (4.22) with $\frac{N v_1 v_2 \delta t \text{sinc}(\theta_{\max})}{v_1 B_2 + v_2 B_1}$. For the open case, Eq. (4.27) becomes a better approximation if $\theta_{\max}$ is small. Then, by approximating $\theta_{\max} \approx 0$, we then have the probability of crossing of the closed case approximated by $\frac{N v_1 v_2 \delta t}{v_1 B_2 + v_2 B_1}$, which is similar to the expression derived for the open case in Eq. (4.28). As mentioned earlier, Eq. (4.27) can be more rigorously related to $\theta_{\max}$ as part of future work.*

[6] We note that a better approximation of the average time can be calculated by considering the motion model of people in Section 4.4, as part of our future work.

4.6 Experimental Results

In this section, we validate the proposed methodology of Section 4.5 with several experiments. We start with a number of experiments in closed areas in both indoor and outdoor, where different number of people walk in two adjacent regions, with a variety of possible speeds per region, and show that our framework can estimate the speeds with a good accuracy. We then run experiments in a museum-style setting, where two exhibitions showcase two very different types of displays. Our approach can then accurately estimate the visitor speeds in both exhibits, and thus deduce which exhibit is more popular.

4.6.1 Experimental Validations and Discussions

In this Section, we extensively validate our framework by estimating the speeds of people in two adjacent regions of an area using the aforementioned experimental setup.

Figure 4.18: The outdoor area of interest with two snapshots of people walking in the area. The black line separates the area into two regions. People move casually throughout the area with the given region-specific speed. A pair of WiFi links located in Region 1 makes wireless measurements to estimate the speed of people in both regions.

Fig. 4.17 shows the considered outdoor and indoor closed areas of interest respectively. Each area is divided into two regions, with a pair of WiFi links located in one of the

True speeds (v_1, v_2)	**Estimated speeds** $(\widehat{v_1}, \widehat{v_2})$
(0.8, 0.8)	(0.9, 0.9)
(0.8, 0.3)	(0.8, 0.3)
(0.8, 1.6)	(0.8, 2.3)
(0.3, 0.8)	(0.4, 0.9)
(0.3, 0.3)	(0.4, 0.4)
(0.3, 1.6)	(0.3, 2.4)
(1.6, 0.8)	(1.7, 0.6)
(1.6, 0.3)	(1.8, 0.5)
(1.6, 1.6)	(1.9, 2)

Table 4.2: A sample performance of our speed estimation approach for Region 1 (v_1) and Region 2 (v_2) of the outdoor area of Fig. 4.18 and the case of $N = 5$ people.

regions. The dimensions of the outdoor area are $L = 4.26\ m$, $B_1 = 5.5\ m$, $B_2 = 8.8\ m$, $X_1 = 2.5\ m$, $X_2 = 3.7\ m$, while the dimensions of the indoor area are $L = 2.25\ m$, $B_1 = 7\ m$, $B_2 = 13\ m$, $X_1 = 2.5\ m$, $X_2 = 4\ m$ (see Fig. 4.17a). People are then asked to walk casually throughout the area, with a specific region-dependent speed. Sample snapshots of people walking in the outdoor and indoor areas are shown in Fig. 4.18 and Fig. 4.19 respectively. We have conducted several experiments in these areas with different number of people walking at a variety of speeds. More specifically, we test the proposed methodology with 9 possible combinations of speeds for (v_1, v_2) for the two adjacent regions. For each pair of speeds, we then run a number of experiments with both 5 and 9 people walking in the area. For any given speed, people are instructed on how to walk with that specific speed as discussed in Section 4.3.1. Table 4.2 shows a sample performance of our approach when 5 people are walking in the outdoor area and for all the 9 speed combinations, while Table 4.3 shows a sample performance when 9 people are walking in the indoor area. It can be seen that our proposed methodology can estimate the speeds of people in the adjacent regions with a good accuracy, for both

True speeds (v_1, v_2)	**Estimated speeds** $(\widehat{v_1}, \widehat{v_2})$
(0.8, 0.8)	(0.9, 0.9)
(0.8, 0.3)	(1, 0.5)
(0.8, 1.6)	(0.9, 1.6)
(0.3, 0.8)	(0.5, 0.9)
(0.3, 0.3)	(0.5, 0.3)
(0.3, 1.6)	(0.4, 1.9)
(1.6, 0.8)	(1.9, 0.7)
(1.6, 0.3)	(1.7, 0.4)
(1.6, 1.6)	(1.9, 2.1)

Table 4.3: A sample performance of our speed estimation approach for Region 1 (v_1) and Region 2 (v_2) of the indoor area of Fig. 4.19 and the case of $N = 9$ people.

Speed	v_1	v_2	v_1 or v_2
NMSE	0.11	0.24	0.18

Table 4.4: NMSE of the estimation of speeds in each region as well as the overall NMSE of the speeds in any of the two regions.

	NMSE		
Scenario	v_1	v_2	v_1 or v_2
Outdoor	0.09	0.16	0.12
Indoor	0.14	0.33	0.23

Table 4.5: NMSE of speed estimation for both indoor and outdoor.

indoor and outdoor cases, by using a pair of WiFi links located in only one region.

To further validate our framework statistically, we repeat each speed pair 3 times, on different days, for both cases of 5 and 9 people walking in the area. This amounts to 108 overall sets of experiments. To evaluate the performance, we calculate the NMSE. Table 4.4 shows the overall NMSE of the estimation error for speed of Region 1 as 0.11, for speed of Region 2 as 0.24, and for the speed in any of the two regions as 0.18, confirming a good performance. Fig. 4.20 further shows the Cumulative Distribution Function (CDF) of the Normalized Square Error (NSE) for the speed of Region 1, Region 2, and the speed in any region. It can be seen that the NSE is less than 0.15, 90% of the time for v_1 and 70% of the time for v_2, further confirming a good performance. We note that the

Number of people	NMSE		
	v_1	v_2	v_1 or v_2
N=5	0.06	0.20	0.13
N=9	0.16	0.29	0.23

Table 4.6: NMSE of speed estimation based on the total number of people walking in the area.

Figure 4.19: The indoor area of interest with two snapshots of people walking in the area. The black line separates the area into two regions. People move casually throughout the area with the given region-specific speed. A pair of WiFi links located in Region 1 makes wireless measurements to estimate the speed of people in both regions.

estimation of v_1, i.e., the speed of the region where the links are located, is more accurate as compared to v_2. We further note that the convergence time of the presented speed estimation results is typically within a couple of minutes, with several cases (those with higher speeds) converging in much less than a minute.

Speed Classification Performance

Thus far, we have established that our approach can successfully estimate the region-dependent speeds of people walking in two adjacent regions, based on WiFi RSSI measurements in only one region. However, for some applications, an exact speed estimation

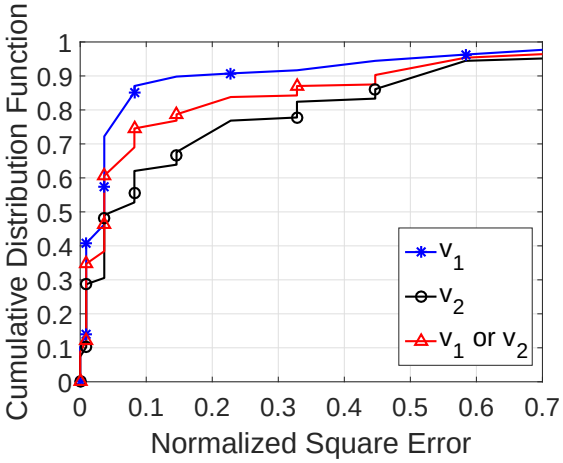

Figure 4.20: CDF of the normalized square error for speeds in Region 1 (v_1), Region 2 (v_2), and for the speeds in any region. It can be seen that our approach estimates the speeds with a good accuracy.

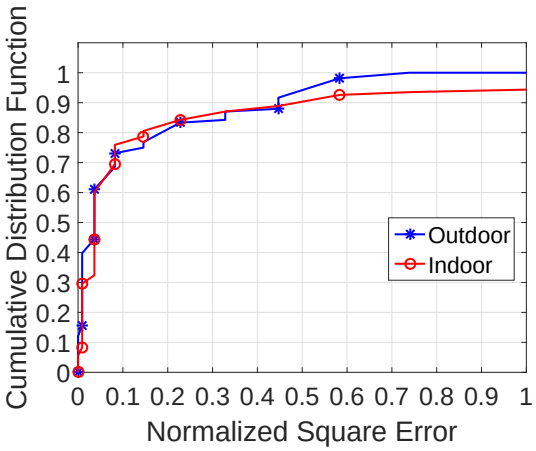

Figure 4.21: CDF of the normalized square error based on the location of the experiment. It can be seen that the outdoor location has a slightly better performance than indoor, as expected.

may not be necessary. Rather, a classification of the pace to low, normal walking, or high may suffice. Therefore, we next show the classification performance of the proposed approach to Low (0.3 m/s), Normal walking (0.8 m/s), or High (1.6 m/s) speeds. More specifically, we classify the estimated speed $\widehat{v_i}$ using nearest neighbor classifier as Low if $\widehat{v_i} \leq 0.55$ m/s, Normal if 0.55 $m/s < \widehat{v_i} \leq 1.2$ m/s, and High if $\widehat{v_i} > 1.2$ m/s, for $i \in \{1, 2\}$. Table 4.7 shows the accuracy of our classification for both indoor and outdoor cases and for different number of people. It can be seen that the overall classification accuracy of the speeds in either of the two regions is 85.2% over all the experiments, confirming a good performance. For comparison, we note that the probability of correct classification would have been 33% in any of the two regions for a random classifier.

Underlying Trends of Speed Estimation

We next discuss some of the underlying characteristics of the results, starting with the impact of the experiment location. Table 4.5 and Fig. 4.21 show the NMSE of the

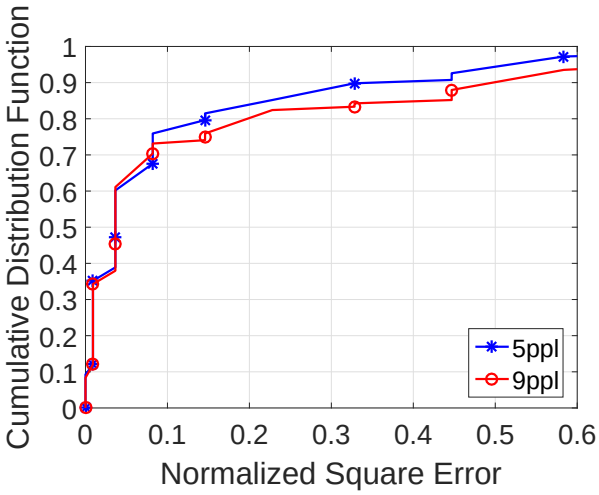

Figure 4.22: CDF of the normalized square error based on the total number of people. It can be seen that the estimation error slightly increases for 9 people as compared to the case of $N = 5$.

estimation error and the CDF of the normalized square error respectively, based on all the experiments in each location. While the estimation error in the indoor environment is still small, the estimation error is less in the outdoor environment as expected, due to the smaller amount of multipath. Furthermore, Table 4.6 and Fig. 4.22 show the performance as a function of the total number of pedestrians. It can be seen that the estimation error is slightly higher for $N = 9$ people as compared to $N = 5$.

Sensitivity to $\theta_{\max}$

As described in Section 4.5, we assume $\theta_{\max} = 45$ n our models of the closed area, which characterizes the flow of people in hallway-type scenarios. We next show the sensitivity of our results to the assumed value of $\theta_{\max}$. More specifically, we assume a broad range of values for $\theta_{\max}$ to characterize the flow of people in our experiments and estimate the speeds of people accordingly. Fig. 4.23 shows the NMSE of the estimated speeds in the two regions as a function of the assumed value of $\theta_{\max}$. It can be seen that the estimation error is nearly constant over a broad range of $\theta_{\max}$, which shows that our

	Classification accuracy (in %)		
Experiment scenario	v_1	v_2	v_1 or v_2
Outdoor N=5 people	100	81.4	90.7
Outdoor N=9 people	88.9	77.8	83.4
Indoor N=5 people	100	66.7	83.3
Indoor N=9 people	92.6	74.1	83.3
All experiments	95.4	75	85.2

Table 4.7: Performance of speed classification to High, Normal Walking, and Low for indoor and outdoor cases, and for different number of pedestrians.

approach is robust and not that sensitive to the exact choice of $\theta_{\max}$.

4.6.2 Museum Experiments

So far, we presented our experimental results for several cases in which people are walking with a variety of speeds in two adjacent regions of an area. We next consider a museum-type scenario, in which there are two adjacent exhibitions, showcasing two very different types of displays. We then utilize our methodology to estimate the visitor speeds in both exhibits, and deduce which exhibit is more popular. By more popular, we mean that the exhibit received more attention, i.e., people slowed down to spend more time there.

For the purpose of this experiment, we stage an exhibition with two types of exhibits in two adjacent regions. We place basic visually-boring displays on the walls of Region 1, such as basic pictures, list of alphabets, and list of numbers. In Region 2, on the other hand, we place more visually-involved displays such as "Where is Waldo" pictures [90].

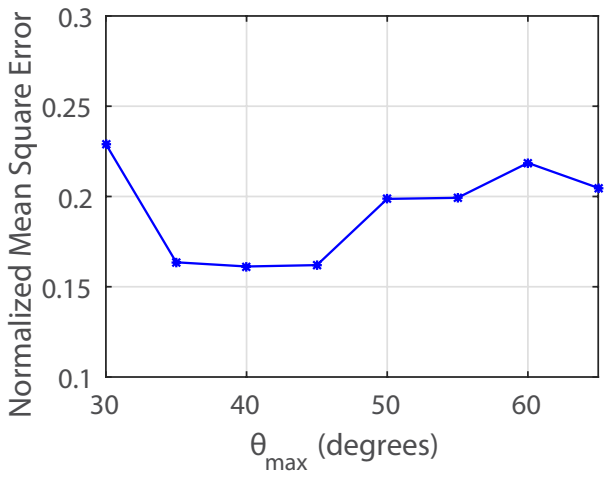

Figure 4.23: Effect of the assumed value of $\theta_{\max}$ on the Normalized Mean Square Error of the estimated speeds in the two regions. It can be seen that NMSE is low for a broad range of $\theta_{\max}$, which shows that it is not that sensitive to the exact choice of $\theta_{\max}$

.

Fig. 4.24 (a) and (b) show a sample display in Region 1 and Region 2 respectively. We use the indoor experiment site shown in Fig. 4.4 for this experiment. We then invite 10 people (randomly selected from our advertisement) to visit this museum. The visitors do not have any background about our experiments. Upon arrival, they are told to explore the area that consists of the two exhibits as it interests them. Note that we do not ask people to walk at a particular speed in a given region, as we did in the validation experiments. Fig. 4.24 (c) shows a snapshot of the museum with people exploring the exhibits. We use the same Tx/Rx locations in Region 1 of Fig. 4.4 and collect the data for 5 minutes. In this setting, we observe that people stop at a display that interests them before moving on to explore other displays. The experiment is videotaped in both regions and the ground-truth average speeds of people in Region 1 and Region 2 are visually estimated as 1.1 m/s and 0.12 m/s, respectively, by extracting the time spent by each person in the two regions from the video. We then use our proposed approach to estimate the average speeds in the two regions of the museum. Fig. 4.25 shows the estimated average speeds in the two regions as a function of time. It can be seen that

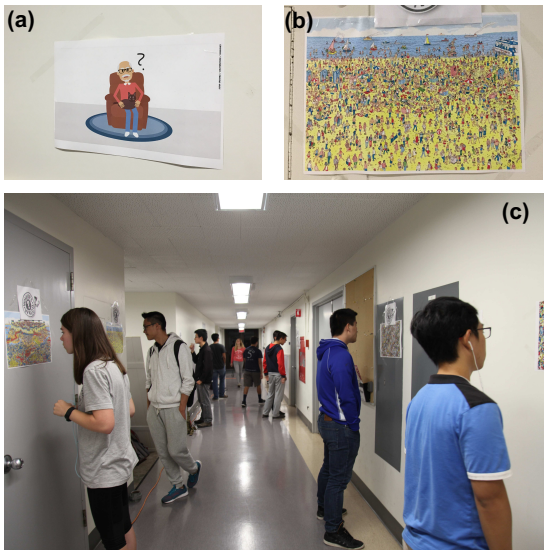

Figure 4.24: Our museum which contains two exhibits – (a) a sample display in the exhibit of Region 1, which contains non-engaging items, (b) a sample display in the exhibit of Region 2, which contains more engaging displays such as "Where is Waldo?", and (c) a snapshot of the visitors exploring the museum.

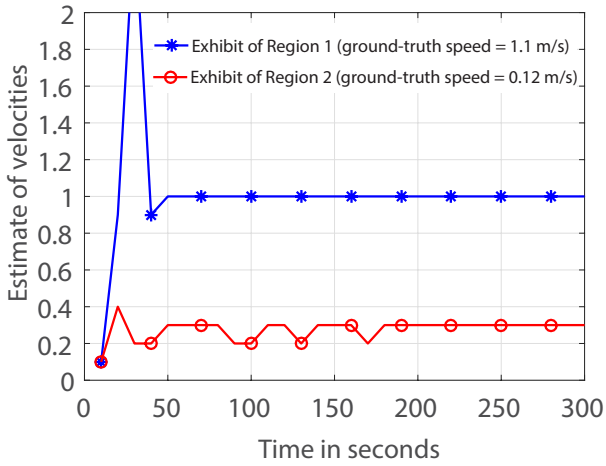

Figure 4.25: Our estimates of the speeds in the two exhibits of the museum experiment of Fig. 4.24. The speed in the Exhibit of Region 2, which contains the Waldo pictures, is estimated as 0.3 m/s, indicating a significant slow down, while the speed in Region 1 is estimated as 1 m/s, which is a normal walking speed. The results further indicate that the exhibit of Region 2 was more engaging and popular.

the speed of people in the Exhibit of Region 2, which contains the Waldo pictures, is estimated as 0.3 m/s, indicating a significant slow down, while the speed in the Exhibit of Region 1 is estimated as 1 m/s, which is a normal walking speed. It can be seen that

these estimates are consistent with the ground-truth and what one would expect based on the level of engagement of the displays. The estimates further indicate that Exhibit 2 was more engaging and popular since it was estimated that people significantly slowed down there. This shows the potential of the proposed methodology for estimating the level of popularity of adjacent displays, based on only sensing and measurement in one of the regions.

Chapter 5

Conclusions and Future Work

In this dissertation, we showed how we can sense our surroundings by utilizing everyday wireless signals such as WiFi. We prioritized having minimal prior knowledge about the sensing environment, the privacy of the people involved, and sensing with inexpensive wireless devices that are used everywhere such as WiFi routers. More specifically, we showed

- How we can image an area, including any occluded objects, using WiFi RSSI measurements without any prior knowledge of the area.
- How to estimate the number of people in an area using only a pair of WiFi transceivers and without depending on people carrying any device. We have further shown how to extend this to crowd counting through walls.
- How to jointly estimate the total number of people and their walking speeds, using only a pair of WiFi links, even in the areas where there is no WiFi coverage and without relying on people to carry any device.

We next summarize our results in each of these areas.

5.1 Robotic Through-Wall Imaging

In Chapter 2, we have considered the problem of high-resolution imaging through walls, with only WiFi signals, and its optimization with unmanned vehicles. We have developed a theoretical framework for this problem based on Rytov wave models, sparse signal processing, and robotic path planning. We have furthermore validated the proposed approach on our experimental robotic testbed. More specifically, our experimental results have shown high-resolution imaging of three different areas based on only a small number of WiFi measurements (20.12%, 4.7% and 2.6%). Moreover, they showed considerable performance improvement over the state-of-the-art that only considers the Line Of Sight path, allowing us to image more complex areas not possible before. Finally, we showed the impact of robot positioning and antenna alignment errors on our see-through imaging framework. Overall, this chapter addresses one of the main bottlenecks of see-through imaging, which is the proper modeling of the receptions.

Since the information about material properties of the objects is inherent in the received signal, reconstructing the material properties of all the objects, along with location and shapes of objects, is an interesting future direction of this work.

5.2 Occupancy Estimation

In Chapter 3, we proposed a new approach for estimating the total number of people walking in an area with only WiFi received power measurements of a wireless link. More specifically, we separated the impact of the crowd on the transmitted signal into two key components: 1) blocking of the LOS and 2) MP effects caused by scattering. By developing a simple motion model, we first mathematically characterized the impact of the crowd on blocking the LOS. We further probabilistically characterized the resulting

multipath fading and developed an overall mathematical expression for the probability distribution of the received signal amplitude as a function of the total number of occupants, which was the base for our estimation using KL Divergence. In order to confirm our approach, we ran several indoor and outdoor experiments with up to and including 9 people and showed that the proposed framework can estimate the total number of people with a good accuracy.

We then extended our approach to through-wall scenarios. More specifically, we proposed a framework to count the total number of people walking behind the walls, using only the RSSI of two WiFi transceivers that are installed outside of the area. We proposed to use the inter-event times corresponding to the signal dips for crowd counting through walls as it is more robust to the attenuation of the walls. More specifically, we showed how to model the impact of people on the received power measurements using superposition of Renewal-type processes. We then mathematically characterized the statistics of the inter-event times of the resulting process and showed how it contains vital information on the total number of people, which then became the base for our ML estimation of the total number of people. To validate our proposed framework, we ran extensive experiments in five different areas on our campus, three classrooms, a conference room, and a hallway, with walls made of different material such as concrete, plaster, and wood, and with up to and including 20 people, and showed that our approach can estimate the total number of people through walls with a high accuracy.

A generic motion model for a casual walk is considered in this chapter. Estimating occupancy in other settings which would involve other motion behaviors, would be an interesting future direction of this work. Furthermore, tracking people along with counting, by utilizing multiple sensors, is another promising future direction of this work.

5.3 Joint Crowd Counting and Crowd Speed Estimation

In Chapter 4, we proposed a system to estimate occupancy attributes in an area such as the number of people, walking speed, and the rate of arrival, by using RSSI measurements of a pair of WiFi links, and in a device-free manner. More specifically, we showed how two key statistics, the probability of crossing and the cross-correlation between the two links, carry key information about the occupancy attributes and mathematically characterized them. To validate our framework, we ran extensive experiments (total of 51) in indoor and outdoor locations, with up to 20 people and with a variety of speeds, and showed that our approach can accurately estimate the occupancy attributes of an area. The NMSE of crowd speed estimation over all the experiments was 0.047, while the NMSE of the arrival rate estimation was 0.034, and the MAE of head counting was 1.3. Finally, we implemented our framework in Costco, estimated the motion behavior of buyers in an aisle, and deduced the popularity of the products in that aisle.

We then extended our framework to estimate the average speeds of pedestrians in two adjacent regions, by using RSSI measurements of a pair of WiFi links in only one region. Our approach only relies on WiFi signal availability in the region where the links are located. Thus, it not only allows for estimating the speed of a crowd in the immediate region where the pair of links are, but also enables deducing the speed of the crowd in the adjacent WiFi-free regions. More specifically, we showed how two key statistics, the probability of crossing and the cross-correlation between the two links, carry key information about the pedestrian speeds in the two regions and mathematically characterized them as a function of the speeds. To validate our framework, we ran extensive experiments (total of 108) in indoor and outdoor locations with up to 10 people, with a variety of speeds per region, and showed that our approach can accurately estimate

the speeds of pedestrians in both regions. Furthermore, we tested our methodology in a museum setting, with two different exhibitions in adjacent areas, and estimated the average pedestrian speeds in both exhibits, thus deducing which exhibit was more popular.

In this chapter, we estimated the traffic flow in an aisle in Costco. A natural extension of this work is to estimate traffic in the entire store or a museum based on a small number of wireless links.

Appendices

Appendix A

Born Approximation

Consider the case of weak scatterers, where the electric properties of the objects in $\mathbf{D}$ are close to free space, i.e., $\epsilon(\mathbf{r})$ is close to ϵ_0. In the Born approximation, this assumption is used to approximate the electric field inside the integral of (2.5) with $E^z_{\text{inc}}(\mathbf{r})$, resulting in the following approximation:

$$E^z(\mathbf{r}) = E^z_{\text{inc}}(\mathbf{r}) + \iiint_{\mathbf{D}} G_{zz}(\mathbf{r}, \mathbf{r}')(O(\mathbf{r}')E^z_{\text{inc}}(\mathbf{r}'))\, dv'. \tag{A.1}$$

The validity of the Born approximation is established by dimensional analysis in (2.5) and it is accurate at high frequencies, only if

$$k_0 L_{\text{obj}} \delta_\epsilon(\mathbf{r}) \ll 1, \text{ for all } \mathbf{r} \in \mathbf{D},$$

Born approximation is a theory of single scattering, wherein the multiple scattering due to object inhomogeneities is neglected.

Appendix B

B.1 Proof of Theorem 4.1

Consider a link located in the area of Fig. 4.1(a), whose x-coordinate is X_i. X_i, for instance, can represent the x-coordinate of either of the links of Fig. 4.17(a). Let the position of the person at time k be $x(k) \leq X_i$. The person crosses the link at time $k+1$, if she/he chooses a direction $\theta(k)$ at time k such that $x(k) + v\delta t\cos(\theta(k)) \geq X_i$, which results in $|\theta(k)| \leq \cos^{-1}\left(\frac{X_i - x(k)}{v\delta t}\right)$, where $|.|$ is the absolute value of the argument. Since $|\theta(k)| \leq \theta_{\max}$, in order to cross the link, the heading direction has to satisfy $|\theta(k)| \leq \min\left\{\theta_{\max},\ \cos^{-1}\left(\frac{X_i - x(k)}{v\delta t}\right)\right\}$. Since the heading direction is uniformly distributed over μ^d, the probability that a person at $x(k)$ crosses the link at time $k+1$, $p^{x(k)}_{c,\text{singleperson}}$, for $x(k) \leq X_i$, is given by, $p^{x(k)}_{c,\text{singleperson}} = \frac{\min\left\{\theta_{\max},\ \cos^{-1}\left(\frac{X_i - x(k)}{v\delta t}\right)\right\}}{2\theta_{\max}}$. By symmetry, it can be seen that $p^{x(k)}_{c,\text{singleperson}}$, for $x(k) \geq X_i$, is given by, $p^{x(k)}_{c,\text{singleperson}} = \frac{\min\left\{\pi - \theta_{\max},\ \pi - \cos^{-1}\left(\frac{x(k) - X_i}{v\delta t}\right)\right\}}{2\theta_{\max}}$. The probability of crossing the link by a single person, $p_{c,\text{singleperson}}$, is then obtained by summing over all the positions from which a cross can occur:

$$p_{c,\text{singleperson}} = \sum_{x(k)=X_i - v\delta t}^{X_i + v\delta t} \frac{\Delta x}{B} p^{x(k)}_{c,\text{singleperson}}, \tag{B.1}$$

where $\frac{\Delta x}{B}$ is the probability that a pedestrian is located at any given position in the area. By substituting the expression for $p^{x(k)}_{c,\text{singleperson}}$ in (B.1) and letting $\delta t \to 0$, we

get, $p_{c,\text{singleperson}} = \frac{\int_{X_i-v\delta t}^{X_i+v\delta t} \min\left\{\theta_{\max},\ \cos^{-1}\left(\left|\frac{X_i-x(k)}{v\delta t}\right|\right)\right\} dx}{2B\theta_{\max}}$. By simplifying this further, we get $p_{c,\text{singleperson}} = \frac{v\delta t \sin(\theta_{\max})}{B\theta_{\max}}$, which proves the Theorem.

Bibliography

[1] D. Evans, *The internet of things: How the next evolution of the internet is changing everything. 2011, URL http://www. cisco. com/web/about/ac79/docs/innov/IoT IBSG 0411FINAL. pdf* (2015).

[2] New study: consumers overwhelmingly reject in-store tracking by retailers, 2014. https://goo.gl/KfuUQo.

[3] Y. Agarwal, B. Balaji, R. Gupta, J. Lyles, M. Wei, and T. Weng, *Occupancy-driven energy management for smart building automation*, in *Proceedings of the 2nd ACM Workshop on Embedded Sensing Systems for Energy-Efficiency in Building*, pp. 1–6, ACM, 2010.

[4] O. Ardakanian, A. Bhattacharya, and D. Culler, *Non-intrusive techniques for establishing occupancy related energy savings in commercial buildings*, in *Proceedings of the 3rd ACM International Conference on Systems for Energy-Efficient Built Environments*, ACM, 2016.

[5] O. Perdikaki, S. Kesavan, and J. M. Swaminathan, *Effect of traffic on sales and conversion rates of retail stores*, *Manufacturing & Service Operations Management* **14** (2012), no. 1 145–162.

[6] Bluescan. www.bluescan.org/english/counting/traffic-counting/.

[7] X. Chen, A. Edelstein, Y. Li, M. Coates, M. Rabbat, and A. Men, *Sequential monte carlo for simultaneous passive device-free tracking and sensor localization using received signal strength measurements*, in *Proceedings of the 10th International Conference on Information Processing in Sensor Networks (IPSN)*, pp. 342–353, 2011.

[8] Y. Chen, D. Lymberopoulos, J. Liu, and B. Priyantha, *Fm-based indoor localization*, in *Proceedings of the 10th international conference on Mobile systems, applications, and services*, pp. 169–182, 2012.

[9] A. Kosba, A. Saeed, and M. Youssef, *Rasid: A robust WLAN device-free passive motion detection system*, in *IEEE International Conference on Pervasive Computing and Communications (PerCom)*, pp. 180–189, 2012.

[10] M. Moussa and M. Youssef, *Smart cevices for smart environments: Device-free passive detection in real environments*, in *IEEE International Conference on Pervasive Computing and Communications (PerCom)*, pp. 1–6, 2009.

[11] R. Nandakumar, K. Chintalapudi, and V. Padmanabhan, *Centaur: locating devices in an office environment*, in *Proceedings of the 18th annual international conference on Mobile computing and networking*, pp. 281–292, 2012.

[12] H. Schmitzberger and W. Narzt, *Leveraging wlan infrastructure for large-scale indoor tracking*, in *Proceedings of the 6th International Conference on Wireless and Mobile Communications (ICWMC)*, pp. 250–255, 2010.

[13] M. Bocca, S. Gupta, O. Kaltiokallio, B. Mager, Q. Tate, S. Kasera, N. Patwari, and S. Venkatasubramanian, *RF-based device-free localization and tracking for ambient assisted living*, .

[14] T. Bailey and H. Durrant-Whyte, *Simultaneous localization and mapping (slam): Part I the essential algorithms*, *IEEE Robotics and Automation Magazine* **13** (2006), no. 2 99 – 110.

[15] T. Bailey and H. Durrant-Whyte, *Simultaneous localization and mapping (slam): Part II*, *IEEE Robotics & Automation Magazine* **13** (2006), no. 3 108–117.

[16] S. Thrun, W. Burgard, and D. Fox, *A probabilistic approach to concurrent mapping and localization for mobile robots*, *Autonomous Robots* **31** (1998), no. 1-3 29–53.

[17] F. Dellaert, F. Alegre, and E. Martinson, *Intrinsic localization and mapping with 2 applications: Diffusion mapping and macro polo localization*, in *International Conference on Robotics and Automation*, pp. 2344–2349, 2003.

[18] E. Jose and M. D. Adams, *An augmented state slam formulation for multiple line-of-sight features with millimetre wave radar*, in *Intelligent Robots and Systems, 2005.(IROS 2005). 2005 IEEE/RSJ International Conference on*, pp. 3087–3092, IEEE, 2005.

[19] W. Chew, *Waves and fields in inhomogeneous media*, vol. 522. IEEE press New York, 1995.

[20] W. Chew and Y. Wang, *Reconstruction of two-dimensional permittivity distribution using the distorted born iterative method*, *IEEE Transactions on Medical Imaging* **9** (1990), no. 2 218–225.

[21] L.-P. Song, C. Yu, and Q. Liu, *Through-wall imaging (twi) by radar: 2-D tomographic results and analyses*, *IEEE Transactions on Geoscience and Remote Sensing* **43** (2005), no. 12 2793–2798.

[22] Q. Liu, Z. Zhang, T. Wang, J. Bryan, G. Ybarra, L. Nolte, and W. Joines, *Active microwave imaging. I. 2-D forward and inverse scattering methods*, *IEEE Transactions on Microwave Theory and Techniques* **50** (2002), no. 1 123–133.

[23] Y.-H. Chen and M. Oristaglio, *A modeling study of borehole radar for oil-field applications*, *Geophysics* **67** (2002), no. 5 1486–1494.

[24] P. V. D. Berg, A. V. Broekhoven, and A. Abubakar, *Extended contrast source inversion*, *Inverse Problems* **15** (1999), no. 5 1325.

[25] M. Pastorino, *Stochastic optimization methods applied to microwave imaging: A review*, *IEEE Transactions on Antennas and Propagation* **55** (2007), no. 3 538–548.

[26] Y. Mostofi, *Compressive cooperative sensing and mapping in mobile networks*, *Mobile Computing, IEEE Transactions on* **10** (2011), no. 12 1769–1784.

[27] J. D. Nichols, L. L. Bailey, N. W. Talancy, E. H. Campbell Grant, A. T. Gilbert, E. M. Annand, T. P. Husband, J. E. Hines, *et. al.*, *Multi-scale occupancy estimation and modelling using multiple detection methods*, *Journal of Applied Ecology* **45** (2008), no. 5 1321–1329.

[28] M. Li, Z. Zhang, K. Huang, and T. Tan, *Estimating the number of people in crowded scenes by mid based foreground segmentation and head-shoulder detection*, in *Pattern Recognition, 2008. ICPR 2008. 19th International Conference on*, pp. 1–4, IEEE, 2008.

[29] S.-F. Lin, J.-Y. Chen, and H.-X. Chao, *Estimation of number of people in crowded scenes using perspective transformation*, *IEEE Trans. on Systems, Man, and Cybernetics-Part A: Systems and Humans* **31** (2001), no. 6 645–654.

[30] K. P. Lam, M. Höynck, B. Dong, B. Andrews, Y.-S. Chiou, R. Zhang, D. Benitez, J. Choi, *et. al.*, *Occupancy detection through an extensive environmental sensor network in an open-plan office building*, *IBPSA Building Simulation* **145** (2009) 1452–1459.

[31] C. Jiang, M. K. Masood, Y. C. Soh, and H. Li, *Indoor occupancy estimation from carbon dioxide concentration*, *Energy and Buildings* **131** (2016) 132–141.

[32] S. Wang, J. Burnett, and H. Chong, *Experimental validation of CO2-based occupancy detection for demand-controlled ventilation*, *Indoor and Built Environment* **8** (2000), no. 6 377–391.

[33] F. Wang, Q. Feng, Z. Chen, Q. Zhao, Z. Cheng, J. Zou, Y. Zhang, J. Mai, Y. Li, and H. Reeve, *Predictive control of indoor environment using occupant number detected by video data and CO 2 concentration*, *Energy and Buildings* **145** (2017) 155–162.

[34] S. Depatla, L. Buckland, and Y. Mostofi, *X-ray vision with only wifi power measurements using rytov wave models*, *IEEE Trans. on Vehicular Technology* **64** (2015), no. 4 1376–1387.

[35] A. Gonzalez-Ruiz, A. Ghaffarkhah, and Y. Mostofi, *An integrated framework for obstacle mapping with see-through capabilities using laser and wireless channel measurements*, *IEEE Sensors Journal* **14** (2014), no. 1 25–38.

[36] C. R. Karanam and Y. Mostofi, *3D through-wall imaging with unmanned aerial vehicles using WiFi*, in *Proceedings of the 16th ACM/IEEE International Conference on Information Processing in Sensor Networks*, pp. 131–142, ACM, 2017.

[37] J. Wilson and N. Patwari, *Through-wall tracking using variance-based radio tomography networks*, *arXiv preprint arXiv:0909.5417* (2009).

[38] J. Weppner and P. Lukowicz, *Bluetooth based collaborative crowd density estimation with mobile phones*, in *IEEE international conference on Pervasive computing and communications*, pp. 193–200, 2013.

[39] M. Wirz, T. Franke, D. Roggen, E. Mitleton-Kelly, P. Lukowicz, and G. Tröster, *Probing crowd density through smartphones in city-scale mass gatherings*, *EPJ Data Science* **2** (2013), no. 1 1.

[40] Y. Yuan, C. Qiu, W. Xi, and J. Zhao, *Crowd density estimation using wireless sensor networks*, in *Mobile Ad-hoc and Sensor Networks (MSN), 2011 Seventh International Conference on*, pp. 138–145, IEEE, 2011.

[41] T. Yoshida and Y. Taniguchi, *Estimating the number of people using existing WiFi access point in indoor environment*, in *Proceedings of the 6th European Conference of Computer Science*, pp. 46–53, 2015.

[42] C. Xu, B. Firner, R. S. Moore, Y. Zhang, W. Trappe, R. Howard, F. Zhang, and N. An, *SCPL: Indoor device-free multi-subject counting and localization using radio signal strength*, in *Proceedings of the 12th international conference on Information Processing in Sensor Networks*, pp. 79–90, ACM, 2013.

[43] S. Di Domenico, M. De Sanctis, E. Cianca, and G. Bianchi, *A trained-once crowd counting method using differential WiFi channel state information*, in *Proceedings of the Workshop on Physical Analytics*, pp. 37–42, ACM, 2016.

[44] W. Xi, J. Zhao, X.-Y. Li, K. Zhao, S. Tang, X. Liu, and Z. Jiang, *Electronic frog eye: Counting crowd using WiFi*, in *IEEE INFOCOM 2014-IEEE Conference on Computer Communications*, pp. 361–369.

[45] A. G. Abuarafah, M. O. Khozium, and E. AbdRabou, *Real-time crowd monitoring using infrared thermal video sequences*, *Journal of American Science* **8** (2012), no. 3 133–140.

[46] P. Liu, S.-K. Nguang, and A. Partridge, *Occupancy inference using pyroelectric infrared sensors through hidden markov models*, *IEEE Sensors Journal* **16** (2016), no. 4 1062–1068.

[47] J. Yun and S.-S. Lee, *Human movement detection and identification using pyroelectric infrared sensors*, *Sensors* (2014) 8057–8081.

[48] M. S. Kristoffersen, J. V. Dueholm, R. Gade, and T. B. Moeslund, *Pedestrian counting with occlusion handling using stereo thermal cameras*, *Sensors* **16** (2016), no. 1 62.

[49] B. Yang, J. Luo, and Q. Liu, *A novel low-cost and small-size human tracking system with pyroelectric infrared sensor mesh network*, *Infrared Physics & Technology* **63** (2014) 147–156.

[50] R. Tomastik, Y. Lin, and A. Banaszuk, *Video-based estimation of building occupancy during emergency egress*, in *American Control Conference, 2008*, pp. 894–901, IEEE, 2008.

[51] New CSC Research Reveals Where Shoppers and Retailers Stand on Next Generation In-store Technology, 2015. https://turtl.dxc.technology/story/55ee93d8bbfd077f2d4e22ee.pdf?

[52] P. Prasertsung and T. Horanont, *How does coffee shop get crowded?: Using WiFi footprints to deliver insights into the success of promotion*, in *Proceedings of the 2017 ACM International Joint Conference on Pervasive and Ubiquitous Computing*, pp. 421–426, ACM, 2017.

[53] L. M. Ni, Y. Liu, Y. C. Lau, and A. P. Patil, *LANDMARC: Indoor location sensing using active RFID*, *Wireless networks* (2004).

[54] Attention, Shoppers: Store Is Tracking Your Cell. goo.gl/DrZFXW.

[55] S. Depatla, A. Muralidharan, and Y. Mostofi, *Occupancy estimation using only WiFi power measurements*, *IEEE Journal on Selected Areas in Communications* **33** (2015), no. 7 1381–1393.

[56] S. Sigg, U. Blanke, and G. Tröster, *The telepathic phone: Frictionless activity recognition from WiFi-RSSI*, in *2014 IEEE International Conference on Pervasive Computing and Communications*, pp. 148–155.

[57] S. Shi, S. Sigg, W. Zhao, and Y. Ji, *Monitoring attention using ambient FM radio signals*, *IEEE Pervasive Computing* **13** (2014) 30–36.

[58] M. Bocca, O. Kaltiokallio, N. Patwari, and S. Venkatasubramanian, *Multiple target tracking with RF sensor networks*, *IEEE Transactions on Mobile Computing* **13** (2014), no. 8 1787–1800.

[59] L. Tsang, J. Kong, and K.-H. Ding, *Scattering of Electromagnetic Waves, Theories and Applications*, vol. 27. John Wiley & Sons, 2004.

[60] J. Shea, P. Kosmas, S. Hagness, and B. V. Veen, *Three-dimensional microwave imaging of realistic numerical breast phantoms via a multiple-frequency inverse scattering technique*, *Medical physics* **37** (2010), no. 8 4210–4226.

[61] Y. Mostofi, *Cooperative wireless-based obstacle/object mapping and see-through capabilities in robotic networks*, *IEEE Transactions on Mobile Computing* **12** (2013), no. 5 817–829.

[62] K. Avinash and M. Slaney, *Principles of computerized tomographic imaging*. Society for Industrial and Applied Mathematics, 2001.

[63] A. Devaney, *A filtered backpropagation algorithm for diffraction tomography*, *Ultrasonic imaging* **4** (1982), no. 4 336–350.

[64] Y. Mostofi and P. Sen, *Compressive Cooperative Mapping in Mobile Networks*, in *Proceedings of the 28th American Control Conference (ACC)*, (St. Louis, MO), pp. 3397–3404, June, 2009.

[65] A. Devaney, *Diffraction tomographic reconstruction from intensity data*, *IEEE Transactions on Image Processing* **1** (1992), no. 2 221–228.

[66] E. Candès, J. Romberg, and T. Tao, *Robust uncertainty principles: Exact signal reconstruction from highly incomplete frequency information*, *IEEE Transactions on Information Theory* **52** (2006), no. 2 489–509.

[67] Y. Wang, J. Yang, W. Yin, and Y. Zhang, *A new alternating minimization algorithm for total variation image reconstruction*, *SIAM Journal on Imaging Sciences* **1** (2008), no. 3 248–272.

[68] C. Li, *An efficient algorithm for total variation regularization with applications to the single pixel camera and compressive sensing*. PhD thesis, 2009.

[69] Y. Wang, J. Yang, W. Yin, and Y. Zhang, *A new alternating minimization algorithm for total variation image reconstruction*, *SIAM Journal on Imaging Sciences* **1** (2008), no. 3 248–272.

[70] M. Inc. http://www.mobilerobots.com.

[71] L. Technologies. http://www.lairdtech.com/Products/Antennas-and-Reception-Solutions/.

[72] Y. Mostofi, *Compressive cooperative sensing and mapping in mobile networks*, *IEEE Transactions on Mobile Computing* **10** (2011), no. 12 1769–1784.

[73] A. Gonzalez-Ruiz, A. Ghaffarkhah, and Y. Mostofi, *An integrated framework for obstacle mapping with see-through capabilities using laser and wireless channel measurements*, *IEEE Sensors Journal* **14** (2014), no. 1 25–38.

[74] H. Minc, *Nonnegative matrices*. Wiley, 1988.

[75] C. D. Meyer, *Matrix analysis and applied linear algebra*. Siam, 2000.

[76] C. D. Godsil, G. Royle, and C. Godsil, *Algebraic graph theory*, vol. 207. Springer New York, 2001.

[77] A. Goldsmith, *Wireless communications*. Cambridge university press, 2005.

[78] E. Jakeman and P. Pusey, *A model for non-rayleigh sea echo*, *Antennas and Propagation, IEEE Transactions on* **24** (1976), no. 6 806–814.

[79] E. Jakeman and R. Tough, *Generalized k distribution: a statistical model for weak scattering*, *JOSA A* **4** (1987), no. 9 1764–1772.

[80] P. M. Shankar, *Ultrasonic tissue characterization using a generalized nakagami model*, *Ultrasonics, Ferroelectrics and Frequency Control, IEEE Transactions on* **48** (2001), no. 6 1716–1720.

[81] D-link. http://www.dlink.com.

[82] T. M. Cover and J. A. Thomas, *Elements of information theory*. John Wiley & Sons, 2012.

[83] V. S. Barbu and N. Limnios, *Semi-Markov chains and hidden semi-Markov models toward applications: their use in reliability and DNA analysis*, vol. 191. Springer Science & Business Media, 2009.

[84] D-link. support.dlink.com/ProductInfo.aspx?m=WBR-1310.

[85] TPlink. www.tp-link.com/en/products/details/cat-11_TL-WN722N.html.

[86] RaspberryPi. www.raspberrypi.org/products/raspberry-pi-3-model-b/.

[87] C. D. Meyer, *Stochastic complementation, uncoupling markov chains, and the theory of nearly reducible systems*, *SIAM review* **31** (1989), no. 2 240–272.

[88] G. Rubino and B. Sericola, *Markov chains and dependability theory*. Cambridge University Press, 2014.

[89] J. D. Little, *Or forumlittle's law as viewed on its 50th anniversary*, *Operations research* **59** (2011), no. 3 536–549.

[90] Where is Waldo, 2015. http://whereswaldo.com/index.html.